

Distribution Agreement

In presenting this thesis or dissertation as a partial fulfillment of the requirements for an advanced degree from Emory University, I hereby grant to Emory University and its agents the non-exclusive license to archive, make accessible, and display my thesis or dissertation in whole or in part in all forms of media, now or hereafter known, including display on the world wide web. I understand that I may select some access restrictions as part of the online submission of this thesis or dissertation. I retain all ownership rights to the copyright of the thesis or dissertation. I also retain the right to use in future works (such as articles or books) all or part of this thesis or dissertation.

Signature:

Radhika Sharma

Date

**Engineering Nanodiscoidal Nucleic Acids as the Next-Generation Platform to Deliver
Oligonucleotide Therapeutics**

By

Radhika Sharma
Doctor of Philosophy

Chemistry

Khalid Salaita, Ph.D.
Advisor

Vincent Conticello, Ph.D.
Committee Member

Yonggang Ke, Ph.D.
Committee Member

Accepted:

Kimberly Jacob Arriola, Ph.D.
Dean of the James T. Laney School of Graduate Studies

Date

**Engineering Nanodiscoidal Nucleic Acids as the Next-Generation Platform to Deliver
Oligonucleotide Therapeutics**

By

Radhika Sharma
B.S. Georgia Institute of Technology, 2016

Advisor: Khalid Salaita, Ph.D.

An abstract of
A dissertation submitted to the Faculty of the
James T. Laney School of Graduate Studies of Emory University
in partial fulfillment of the requirements for the degree of
Doctor of Philosophy
in Chemistry
2022

Abstract

Engineering Nanodiscoidal Nucleic Acids as the Next-Generation Platform to Deliver Oligonucleotide Therapeutics

By Radhika Sharma

Over the past several decades, nucleic acid therapeutics have made successful strides and almost a dozen therapies have received FDA approval. Typically, a DNA or RNA based drug is a short oligomer comprised on average of <25 base pairs and designed to target a specific mRNA sequence within a cell. As exogenous DNA and RNA sequences, these nucleic acids take advantage of Watson-Crick-Franklin base pairing to bind to and perturb native translational activity and initiate degradation. Despite the simple mechanism, delivery of these drugs has been significantly hindered because of several intracellular and extracellular barriers. To overcome these issues, nanoparticles are often the choice delivery vehicle owing to their large surface areas and small sizes. In this dissertation, we investigate the potential for a high-density lipoprotein (HDL) mimetic known as nanodiscs (NDs) to serve as a biomimetic vector for delivering therapeutic oligonucleotides. In Chapter 1, a comprehensive overview on nucleic acid therapeutics, and the advantages endowed by the ND based on its design, properties, and innate targeting features, compared to other NPs are elucidated. Chapter 2 introduces the conceptualization and construction of the initial ND scaffold: a ND composed of DMPC, thiol phospholipids, and a mimetic Apolipoprotein A1 peptide. We demonstrate that this framework can covalently bind 15 copies of DNA/ND and not alter the ND morphology, its selective recognition pathway using the non-endocytic Scavenger Receptor B1, or overall functional activity as a result. Chapter 3 builds off the framework revealed in Chapter 2 to create the nanodiscoidal nucleic acid (NNA) scaffold. The NNA scaffold is maximally packed with the highest density of nucleic acid reported yet to date, beating even our previous record in Chapter 2. Detailed *in vitro* and *in vivo* studies highlight the potency of the NNAs as an enhanced therapeutic. We reveal that the constructed scaffold was highly active in lowering the effective dose of a HIF-1- α ASO five-fold, to a level that was previously rendered ineffective by pharmaceutical companies. This work culminates in Chapter 4 by exploring the outlook and future of how NNAs are the next promising step towards advancing oligonucleotide therapeutics.

**Engineering Nanodiscoidal Nucleic Acids as the Next-Generation Platform to Deliver
Oligonucleotide Therapeutics**

By

Radhika Sharma
B.S. Georgia Institute of Technology, 2016

Advisor: Khalid Salaita, Ph.D.

A dissertation submitted to the Faculty of the
James T. Laney School of Graduate Studies of Emory University
in partial fulfillment of the requirements for the degree of
Doctor of Philosophy
in Chemistry
2022

Dedication

This dissertation is dedicated to my family which includes my mom, Anna Sharma, my dad, Arun Sharma, and my sister, Artee Sharma. They have been strong support pillars throughout this journey, and I undoubtedly could not have survived the graduate school challenges if it was not for their unwavering support and encouragement. Thank you for always providing me the space and constantly pushing me to achieve everything I desire.

I also dedicate this dissertation to my significant other, Misael Adair Romero-Reyes. We met one semester after I started graduate school and instantly bonded. Throughout these last 4.5 years he has stood by my side in the ups and downs, including the difficult challenges the COVID-19 pandemic brought both of us. There is no one better I can have by my side to complete this journey and cannot wait for what is to come.

Lastly, I dedicate this work to the mice whose lives were sacrificed for advancing my research and providing the potential to transform oligonucleotide delivery.

Acknowledgements

I will always have eternal gratitude towards my advisor, my committee, my peers, friends, family, and significant other for lending their support, time, finances, and scholarship to meld me into the scientist and research that I am today. I would like to first and foremost acknowledge my advisor, Dr. Khalid Salaita for taking a chance on me. I came to graduate school with no formal research experience and only a desire to become a better scientist. I was initially drawn to Khalid because he manifested this amazing excitement for science, really matching the passion that led me to pursue graduate school in the first place. Throughout my research, Khalid has always pushed me further than I thought I could ever reach. Under his tutelage I developed as a critical thinker, science communicator, and most of all, as an independent scientist. Thank you, Khalid, for your time and investment. I will be lucky if I can even be half the scientist that you are.

I am thankful for my past, present, and new committee members: Dr. Vincent Conticello, Dr. Jennifer Heemstra, and Dr. Yonggang Ke. Their insight and tidbits of advice in my annual committee meetings is what helped developed my project into the current state that it is today. Thank you, Vince, for your support and encouraging emails while serving on my committee- a truly compassionate act that I will always remember.

I would also like to express my sincere appreciation for my parents. Their love and unconditional support became something I relied on almost every day. More than half of the meals I consumed in graduate school were delivered from my mom's kitchen and provided just the right nourishment to help me stay the course. I am eternally indebted because of their countless sacrifices that have led me to what I am today. I also would like to thank my sister Artee for her continual care, because she has the lifelong role of being my sibling! My career would not be in the trajectory that it is today without her persistence and efforts.

I am thankful for my partner, boyfriend, and companion, Misael. The last thing I expected when I started graduate school was to find such a wonderful life partner. However, life had other plans for me when we instantly connected in April 2018 – my second semester of my first year in

graduate school. Misael has been resilient and has stood by me for the good, the bad, and the ugly. The graduate school journey is not an easy one, and I hope everybody is as lucky as me to have a Misael by their side. Misael, I am thrilled for our next chapter, which hopefully will also include traveling the world.

My graduate school experience was highly enriched through the forging of many new friendships, especially the ones I made outside of the chemistry department and some outside Emory University. Prominent friends I would like to thank include Sallie Stern, Derek Onken, Dylan Allen, Deanna Zhong, Pranav Bhandari, Katherine Goree, Patrick Steng, Juliana Ribiero, Larissa Xavier, Farnaz Tahmasab, Ali Ahmadvand, and Alina Ionescu. I hope to continue these meaningful friendships beyond our path at Emory and graduate school overall. I am grateful for my friends including Elijah and Krista Idowu, Vincent Way, Marybeth Dooley, Renee Desprez, Navi Kamra, and Cary McGinnis for always checking in and caring for my wellbeing.

I especially made long-term friendships and am deeply appreciative of my colleagues-turned-friends such as Yixiao Dong, Rachel Bender, Anna Kellner, Nicolas Watkins, Gokul Raghunath, Arventh Velusamy, Yuesong Hu, Youngsun Kim, Sara Gebre, Torie Snider, and Arunava Manna. Despite the pandemic and the pressures of graduate school, I have been fortunate enough to develop lifelong friends and meaningful relationships.

No dissertation achievements can be possible without the helpful support of the Salaita Lab, including members from the past and present. I would like to especially thank Victor Ma, my invaluable mentor who helped me get established within the lab and always provided me with vital advice for my project, graduate school career, and beyond- even till this day. Other notable lab members I would like to thank are Jiahui Zhang and Steven Narum. Thank you for your input, assistance, training, and support that was lent towards me and the success of my project. Our collective efforts have resulted in the development of Nanodiscoidal Nucleic Acids – and I am excited to see this project develop further in the lab and beyond. To the readers, I hope this research will bring inspiration towards nanoparticle and drug delivery research for years to come.

Table of Contents

List of Figures	iii
List of Tables	iv
Common Abbreviations	v
Chapter 1: Introduction	1
1.1: Brief Overview of Nucleic Acid Therapeutics	2
1.2: Challenges of Nucleic Acid Therapeutics	3
1.3: High-Density Lipoproteins: Cholesterol and Cargo Transport	6
1.4: Advantages of HDL as a Transport Scaffold	9
1.5: Structural Properties of ApoA1 and ApoA1 Mimetic Peptides	11
1.6: Phospholipids and Assembly Techniques for Synthetic HDL Structures	17
1.7: Shortcomings in Previous Renditions of HDL Mimics as a Nucleic Acid DDS	22
1.8: Summary and Scope of this Dissertation	25
Chapter 2: Gene Regulation Using Nanodiscs Modified with HIF-1- α ASOs	27
2.1: Overview	28
2.2: Introduction	29
2.3: Results and Discussion	32
2.3.1 Incorporating and Assembling Thiol-Functionalized NDs	32
2.3.2: ND Conjugation to DNA	33
2.3.3: DNA bound to the surface of the ND is functional and nuclease resistant	37
2.3.4: ASO-ND conjugates are internalized in a dose- and time-dependent manner	38
2.3.5: The uptake of thiol NDs and ASO-NDs into cells is partially mediated by SRB1	40
2.3.6: Anti-HIF-1- α ASO-ND conjugates are active <i>in vitro</i>	42
2.4: Conclusion	46
2.5: Materials and Methods	47
2.5.1: Synthesis and Characterization of Thiol ND	48
2.5.2: DLS and TEM Characterization of Thiol NDs	49
2.5.3: Addition of Maleimide Group to DNA	49
2.5.4: Covalent Linkage of DNA to NDs	50
2.5.5: FRET Analysis of ASO-ND Samples	51
2.5.6: Quantification of DNA Density	51
2.5.7: Zeta (ζ) Potential Measurement of DNA-ND Samples	52
2.5.8: Gel Electrophoresis	52
2.5.9: DNazyme Kinetics and Nuclease Degradation Assay	52
2.5.10: Cell Culture	53
2.5.11: Confocal Microscopy of HeLa Cells	53
2.5.12: Dose- and Time-Dependent Uptake Measurements using Flow Cytometry	53
2.5.13: SRB1 Mediated Uptake of ASO-NDs	54
2.5.14: RT-qPCR to Assess HIF-1- α Levels after EZN-2968 ASO-ND Treatment <i>in vitro</i>	54
2.5.16: Comparing Dose-Dependent Uptake of Anti-HIF-1- α ASO/ Anti-HIF-1- α ASO-NDs	54
2.5.17: MTT Assay to Assess Cell Viability	55
2.6: Supplementary Information	56
Chapter 3: Nanodiscoidal Nucleic Acids for Gene Regulation	63
3.1: Overview	64

3.2: Introduction	65
3.3: Results and Discussion	68
3.3.1 Screening of Cysteine-Modified ApoA1 Mimetic Peptides.....	68
3.3.2: NNAs are Internalized into Cells via Scavenger Receptor B1	75
3.3.3: Internalized ASO-NDs and NNAs Undergo Dissociation with 24 h	78
3.3.4: Quantifying NNA and ASO-ND Activity <i>In Vitro</i>	80
3.3.5: NNAs Penetrate into the Hypoxic Core of Tumor Spheroids and are active	82
3.3.6: Anti-HIF-1- α NNAs are Active <i>In Vivo</i>	85
3.4: Conclusion	88
3.5: Materials and Methods	89
3.5.1: Synthesis and characterization of ND and NNA scaffolds.....	91
3.5.2: Size and morphology characterization of NDs and NNAs	91
3.5.3: Coupling maleimide-DNA onto the ND and NNA scaffolds	92
3.5.4: Quantifying DNA density.....	92
3.5.5: Bulk solution FRET measurements of DNA-NDs and NNAs	93
3.5.6: Gel electrophoresis and serum degradation assay	93
3.5.7: DNase I assay	93
3.5.8: Cell and spheroid culture	94
3.5.9: Confocal uptake studies on HeLa cells and spheroids	94
3.5.10: SRB1 mediated uptake of ASO-NDs and NNAs into cells and spheroids	95
3.5.11: Sensitized FRET measurements of ASO-NDs and NNAs in HeLa cells	96
3.5.12: RT-qPCR to assess HIF-1- α levels after <i>in vitro</i> treatment with EZN2968.....	97
3.5.13: MTT assay to assess cell viability.....	97
3.5.14: Mice acclimatization and tail-vein injection of ND scaffold, NNAs, and ASO	98
3.5.15: Murine <i>in vivo</i> and <i>ex vivo</i> fluorescence imaging	98
3.5.16: RNA isolation and RT-qPCR quantification of HIF-1- α from mice organs	99
3.6: Supplementary Information.....	100
Chapter 4: Recap and Future Directions	107
4.1: Summary and Conclusions.....	108
4.2.: Future Directions	109
References	111

List of Figures

Figure 1.1.1: The different forms of FDA approved nucleic acid therapeutics.	2
Figure 1.2.1: Common nucleic acid modifications	4
Figure 1.2.2: Intracellular and extracellular barriers for NP delivery in humans.	5
Figure 1.3.1: Lipoproteins that are native to the human body.....	6
Figure 1.3.2: Lipoprotein transport and functions within the body.	7
Figure 1.3.3: Pre- β discoidal HDL.....	8
Figure 1.3.4: Structure of mature HDL.....	8
Figure 1.4.1: Mechanism by which HDL docks onto SRB1 and deposits cholesterol.....	10
Figure 1.5.1: HDL biogenesis.	12
Figure 1.6.1: Solubilization of lipid vesicles using ApoA1 mimetic peptides.	18
Figure 1.7.1: Multivalency of HDL.....	23
Figure 2.1.1: Conceptual overview of the design strategy for covalent DNA-NDs.....	28
Figure 2.3.1: Coupling and optimizing DNA onto ND Surface.	34
Figure 2.3.2: Validating and characterizing DNA attachment to surface.	35
Figure 2.3.3: Activity and nuclease resistance of DNA-NDs.....	37
Figure 2.3.4: Uptake of ASO-NDs in HeLa, U373, and PLC/PRF/5.	39
Figure 2.3.5: SRB1 partially mediates uptake of ASO-NDs.....	41
Figure 2.3.6: Quantifying functional activity of ASO-NDs that target HIF-1- α	43
Figure S2.6.1: DNA density using click chemistry approach	56
Figure S2.6.2: TEM panel of NDs incorporated with different ratios of lipids.....	57
Figure S2.6.3: DLS stability data of 10% thiol DNA-NDs.....	57
Figure S2.6.4: Catalytic activity of DNAzyme-NDs.	57
Figure S2.6.5: Confocal microscopy of time-dependent internalization.....	58
Figure S2.6.6: Quantification of ND uptake into HeLa, U373, and PLC/PRF/5 cells.	59
Figure S2.6.7: SRB1 expression on HeLa, U373, and PLC/PRF/5 cells.	59
Figure S2.6.8: Role of SRB1 in mediating uptake of NDs only.....	60
Figure S2.6.9: Quantitative Cy5 fluorescence intensity plots of cells treated with BLT-1	60
Figure S2.6.10: Activity factor comparing the activity of ASO-ND vs. naked ASOs.	61
Figure 3.1.1: Overview of nanodiscoidal nucleic acids and their activity.	64
Figure 3.3.1: Engineering and assembly of nanodiscoidal nucleic acids.....	69
Figure 3.3.2: Electron microscopy imaging of the ND and NNA scaffolds.....	71
Figure 3.3.3: DNA conjugation and nuclease resistance of NNAs.....	73
Figure 3.3.4: Cell Uptake and SRB1 Assay for ASO-NDs and NNAs.....	76
Figure 3.3.5: Sensitized-FRET assays of ASO-NDs and NNAs.	79
Figure 3.3.6: Quantifying the functional activity of ASO-NDs and NNAs in cells.	84
Figure 3.3.7: Uptake and functional activity of NNAs in H1299 spheroids.....	87
Figure 3.3.8: <i>In vivo</i> internalization and gene silencing efficacy of NNAs.....	87
Figure S3.6.1: Helical wheel diagrams of 22A ApoA1 and modified 22A ApoA1 peptides.....	101
Figure S3.6.2: DLS measurements of ASO-NDs and NNAs before and after DNA addition... ..	101
Figure S3.6.3: BLT-1 inhibition and raw intensity plot of DNA-NDs and NNAs.	101
Figure S3.6.4: Flowchart of the image processing performed to determine FRET index.	102
Figure S3.6.5: Representative epifluorescence images for FRET controls.	103
Figure S3.6.6: Quantifying HIF-1- α levels of NNAs in harvested organs of mice.....	104

List of Tables

Table 1.1.1: FDA approved nucleic acid therapeutics.....	3
Table 1.5.1: Distinction of ApoA1 residues and associated sequences.....	14
Table 1.5.2: Representative list of ApoA1 mimetic peptides.....	16
Table 1.6.1: Phospholipids used to prepare HDL mimics.....	19
Table 1.7.1: List of gene targets targeted by HDL therapies.....	24
Table S2.6.1: Lipids used to prepare thiol-modified NDs.....	61
Table S2.6.2: Oligonucleotide and primer sequences used for <i>in vitro</i> studies.....	62
Table S3.6.1: Comparison of DNA copies occupied on gold & different ND scaffolds.....	105
Table S3.6.2: Lipids used for preparing ND scaffold (1 - 7)..	105
Table S3.6.3: Nucleic acid sequences used for the NNA study.....	106

Common Abbreviations

18S	18S Ribosome	RT-qPCR	Real Time- Quantitative Polymerase Chain Reaction
22A	ETC-642 22A ApoA1 Mimetic Peptide	POPC	1-palmitoyl-2-oleoyl-glycero-3-phosphocholine
ABCA1	ATP Binding Cassette, Member A1	PS	Phosphorothioate
ABCG1	ATP Binding Cassette, Member G2	RCT	Reverse Cholesterol Transport
ASO	Antisense Oligonucleotide	mRNA	Messenger Ribonucleic Acid
BLT-1	Blocker of Lipid Transport 1	SMCC	Succinimidyl 4-(N-maleimidomethyl)cyclohexane-1-carboxylate)
DDS	Drug Delivery System	SRB1	Scavenger Receptor, Class B, Type 1
DLS	Dynamic Light Scattering	SUV	Small Unilamellar Vesicles
DMPC	1,2-Dimyristoyl- <i>sn</i> -glycero-3-phosphocholine	TEM	Transmission Electron Microscopy
DNA	Deoxyribonucleic Acid	VLDL	Very Low-Density Lipoprotein
DOPC	1,2-Dioleoyl- <i>sn</i> -glycero-3-phosphocholine		
DPPC	1,2-Dipalmitoyl- <i>sn</i> -glycero-3-phosphocholine		
DPPE	1,2-Dipalmitoyl- <i>sn</i> -glycero-3-phosphoethanolamine		
DPPG	1,2-Dipalmitoyl- <i>sn</i> -glycero-3-phospho-(1'- <i>rac</i> -glycerol)		
DSPC	1,2-distearoyl- <i>sn</i> -glycero-3-phosphocholine		
DSPE	1,2-distearoyl- <i>sn</i> -glycero-3-phosphoethanolamine		
EZN2968	Enzon 2968 HIF-1- α ASO		
FRET	Fluorescence Resonance Energy Transfer		
HDL	High Density Lipoprotein		
HIF-1- α	Hypoxible Inducible Factor 1 α		
HPPS	HDL Mimicking Peptide Phospholipid Scaffold		
LCAT	Lecithin-Cholesterol Acyl Transferase		
LDL	Low Density Lipoprotein		
LNA	Locked Nucleic Acid		
LNP	Lipid Nanoparticle		
MTT	3-(4,5-dimethylthiazol-2-yl)-2,5-diphenyltetrazolium bromide		
ND	Nanodisc		
NNA	Nanodiscoidal Nucleic Acid		
NP	Nanoparticle		

Chapter 1

Introduction

1.1: Brief Overview of Nucleic Acid Therapeutics

Nucleic acid therapy is commonly referred to as the delivery of an exogenous strand of DNA/RNA, often < 25 nucleotides, to complementary bind and modulate cellular messenger RNA (mRNA) levels in the cell. Mitigation of mRNA is critical because common treatments will target protein expression levels, and not the underlying cause that is responsible for maintaining the protein expression required to sustain a disease state. The FDA approval of nucleic acid drugs has greatly escalated in the past decade (**Table 1.1.1**) and especially gained heightened prominence outside the scientific and medical community because of its vital role in battling the current Sars-CoV-2 (COVID-19) pandemic. The common types of nucleic acids used in the clinic are antisense oligonucleotides (ASOs), short interfering RNAs (siRNA), and of late, mRNA vaccines (**Figure 1.1.1**), which functions to introduce mRNA to induce antigen production and immune protection. Despite the strong significance and pressing need for nucleic acid therapies, many nucleic acids face challenges and become eventually “stuck” in the pipeline, unable to translate into clinical use.

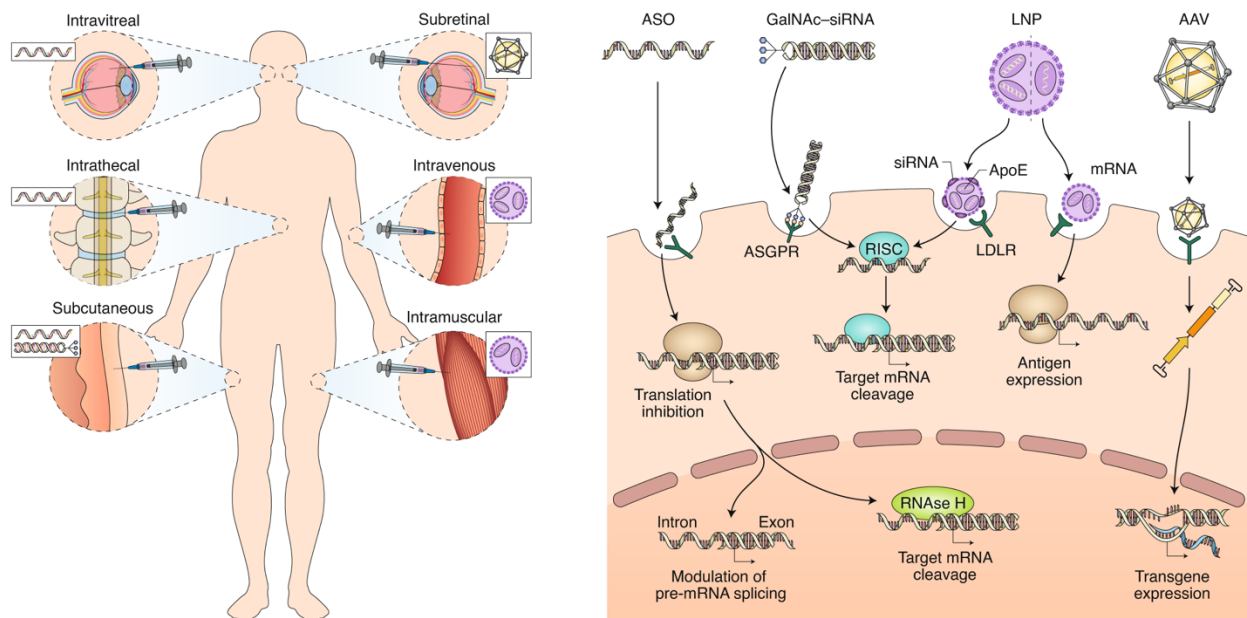


Figure 1.1.1: The different forms of FDA approved nucleic acid therapeutics, including their mechanism, and common injection routes today. Ref (1)

Table 1.1.1: FDA approved nucleic acid therapeutics

Drug	Company	Indication (Target)	Type	Administration	Year Approved	Delivery Vehicle
Vitravene	Ionis	Cytomegalovirus Retinitis (CMV IE-2)	ASO	Intraocular	1998	Naked
Kynamro	Ionis	Homozygous Hypercholesteremia (ApoB-100)	ASO	Subcutaneous	2013	Naked
Exondys 51	Sarepta	Duchenne Muscular Dystrophy (Exon 51)	ASO	Intrathecal	2016	Naked
Spinraza®	Ionis	Spinal Muscular Atrophy (SMN2)	ASO	Intrathecal	2016	Naked
Tegsedi	Ionis	Hereditary Transthyretin-Mediated Amyloidosis (TTR)	ASO	Subcutaneous	2018	Naked
Onpatro®	Ionis	Hereditary Transthyretin-Mediated Amyloidosis (TTR)	siRNA	Intravenous	2018	LNP
Vyondys 53	Sarepta	Duchenne Muscular Dystrophy (Exon 53)	ASO	Intravenous	2019	Naked
Givlaari®	Alnylam	Acute Hepatic Porphyria (ALAS1)	siRNA	Subcutaneous	2019	GalNAc
Viltepso	NS Pharma	Duchenne Muscular Dystrophy (Exon 53)	ASO	Intravenous	2020	Naked
Oxlumo®	Alnylam	Primary Hyperoxaluria Type I (HA01)	siRNA	Subcutaneous	2019	GalNAc
Leqvio®	Novartis	Heterozygous Hypercholesteremia (PCSK9)	siRNA	Subcutaneous	2020	GalNAc
Amondys 45	Sarepta	Duchenne Muscular Dystrophy (Exon 45)	ASO	Intravenous	2021	Naked
Comirnaty®	Pfizer-BioNTech	Sars-CoV-2	mRNA	Intramuscular	2021	LNP
mRNA-1273	Moderna	Sars-CoV-2	mRNA	Intramuscular	2022	LNP
Amvuttra	Alnylam	Hereditary Transthyretin-Mediated Amyloidosis (TTR)	siRNA	Subcutaneous	2022	GalNAc

1.2: Challenges of Nucleic Acid Therapeutics

Efficacy of most nucleic acid drugs are severely limited due to ineffective delivery to its intended target.¹ Previously, nuclease degradation from serum proteins used to pose a significant challenge. However, most degradation has been subdued because of the advent of chemical modifications to the nucleic acid backbone, thus significantly improving the nuclease susceptibility assists in prolonging the half-life of the sequence (**Figure 1.2.1**).² Chemical modifications were introduced into sequences in the '90s, deeming them as “first-generation” nucleic acids. However,

now with the presence of second and third generation oligonucleotides, there is still a relative stagnation for drug approvals, suggesting unmet challenges.

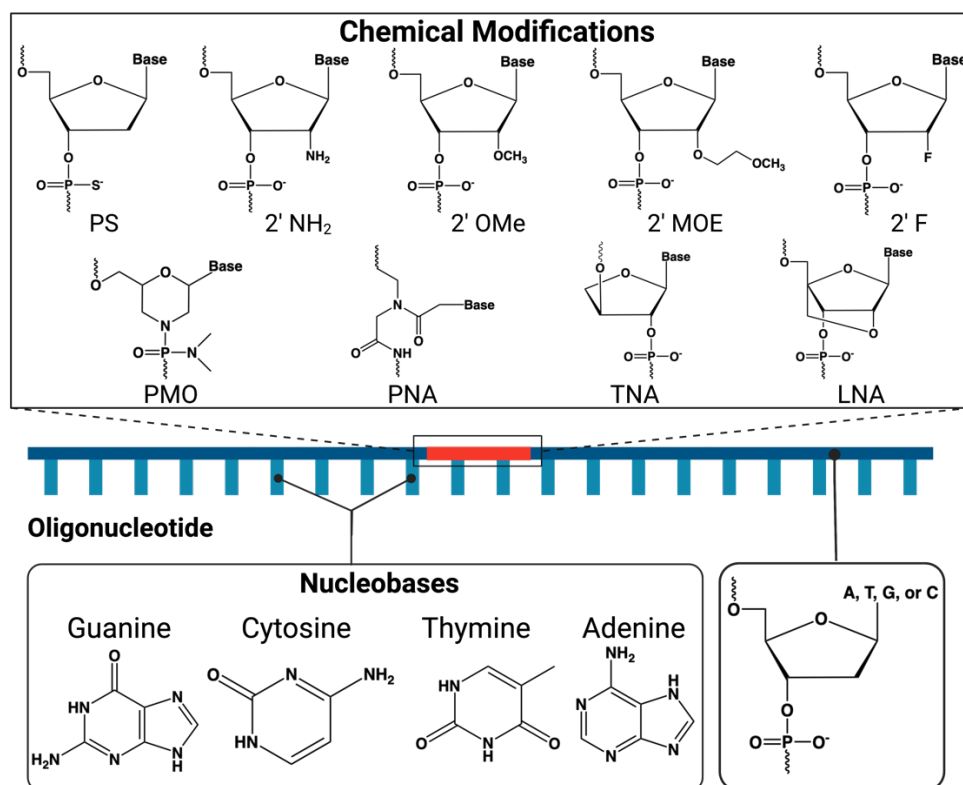


Figure 1.2.1: Common nucleic acid modifications imparted to the backbone or the sugar of the nucleobase to confer nuclease resistance, promote target affinity, and extend the half-life in serum.

Upon delivery, exogenous nucleic acids are still vulnerable to thrombocytopenia,³ bulkiness and/or charge restrictions¹ of the oligonucleotide which limits transport across the plasma membrane and increased endosomal entrapment and other nonproductive internalization pathways that promote degradation inside the cell.⁴ To facilitate and enhance delivery, most often a drug delivery system (DDS) is employed, such as a high-affinity receptor-targeting ligand such as *N*-acetylgalactosamine (GalNAc) or nanoparticles (NPs). NPs offer compelling advantages such as higher conjugation density because of the high surface area and smaller sizes to assist in cell penetration. However, not all NPs are equal and can face challenges in opsonization upon delivery;⁵ each platform provides its own sets of challenges depending on the composition and structure. For example, the safety profile for inorganic NPs is fundamentally questionable and these NPs lack specificity and compromise delivery.⁶ Alternatively, lipid scaffolds are

biocompatible and safe for use in humans. As noted in **Table 1.1.1**, the certain FDA approved drugs, including the COVID-19 vaccines are formulated using lipid nanoparticles (LNPs) such as liposomes. LNPs are a step-forward in DDS purposes, but they are not easily applicable in every situation. Liposomes face multiple issues during scaleups and have low drug loading efficiencies.⁷ Liposomes present with lower stabilities *in vivo* and are faced with numerous intracellular and extracellular barriers during drug delivery (**Figure 1.2.2**),⁸ resembling similar obstacles that naked nucleic acids face upon delivery. Of note is that liposome and LNP formulations can undergo nonspecific extravasation that could potentially lead to many unintended targeting, hence lowering delivery and therapeutic efficacy.⁹

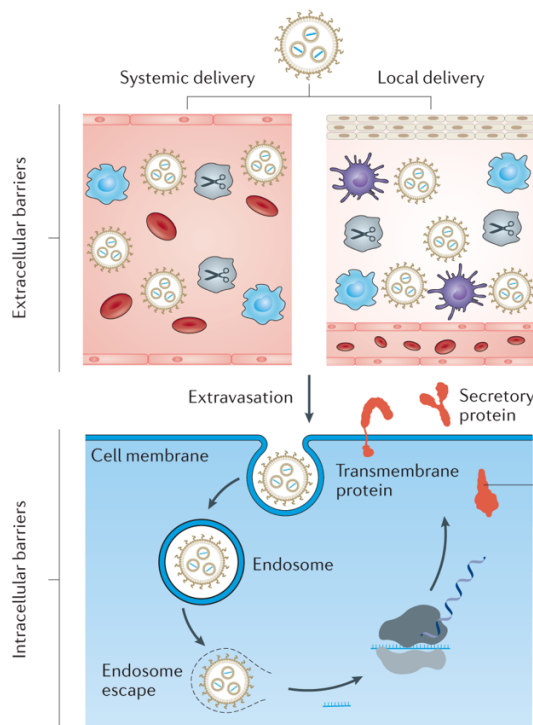


Figure 1.2.2: Intracellular and extracellular barriers that LNPs (and other NPs) that occur upon delivery in humans. Ref (8)

Furthermore, any internalized oligonucleotide, whether it be from targeted delivery from nanoparticles, GalNAc or other receptor-targeting moieties, and/or extravasation, will be transported internally into the cell the via endocytosis. Endocytosis is a nearly inevitable process that occurs during the delivery of any drug and is almost agnostic to any carrier platform. Endocytosis is a necessary regulatory process that carefully controls the cell's composition

because of the semi-permeable nature of the cell membrane. This process assists in internalizing nutrients and controlling signaling cascades, and by default, this process involves entrapping any external cargo, including therapeutic drugs that meander near the cell. Less than 1% of entrapped oligonucleotides can escape the endosome,¹⁰ and the remaining 99% of internalized drugs are degraded in the late endosomal-lysosomal degradation pathway.

Understandably, the challenges presented in delivery considerably diminishes efficiency and augments the required dosage for efficacy, almost nullifying the advantages of using a NP DDS. Most current oligonucleotide therapies are currently very costly, and increasing the dosage, especially with the required chemical modifications, presents with prohibitive costs and inaccessibility for many patients. Therefore, an ideal technique that can boost drug delivery can be described as one that is not only biocompatible, but is a biomimetic, so it can increase circulation within the body for longer periods of time, bypass the endosome (to some extent) and achieve selective and targeted delivery of its cargo.

1.3: High-Density Lipoproteins: Cholesterol and Cargo Transport

The human body endogenously contains multiple lipoproteins (**Figure 1.3.1**), assemblies of lipids and proteins, that assist in the transport of hydrophobic molecules throughout the body, beginning from ingestion. Lipoproteins can be structurally differentiated by the lipids and scaffolding proteins used for these structures (i.e., lipid:protein ratio), which in tune affects the density of these structures.¹¹ One such example of lipoproteins are high-density lipoproteins (HDLs), the densest of the structures within our body.

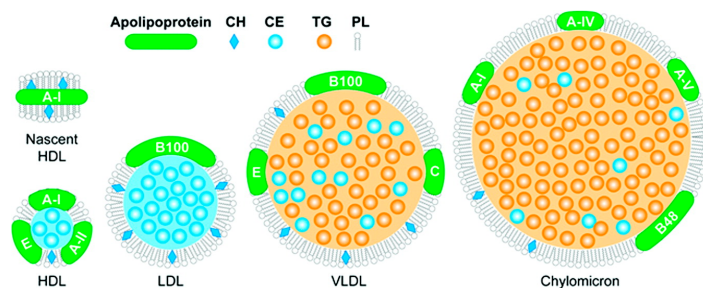


Figure 1.3.1: Lipoproteins that are native to the human body. Ref (11)

HDL, often referred to as the “good cholesterol” plays a vital role in reverse cholesterol transport (RCT) and maintaining cholesterol homeostasis (**Figure 1.3.2**). Excess cholesterol is scavenged by HDL and shuttled back to the liver for metabolism and excretion. In addition to its atheroprotective role, HDL has been noted to possess multiple other beneficial properties including but not limited to antithrombotic,¹² anticoagulant,¹³ antioxidative,¹⁴ anti-apoptotic,¹⁵ and anti-inflammatory functions.¹⁶ These multifaceted attributes play critical roles in moderating disease and pathophysiological effects while supporting a healthy, physiological environment.

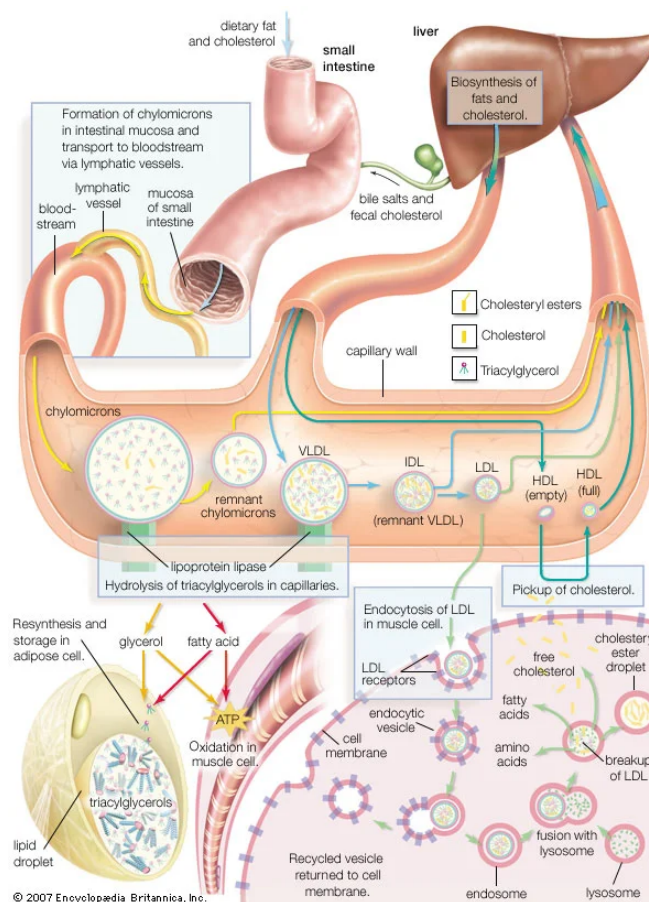


Figure 1.3.2: Lipoprotein transport and functions within the body.

HDL biogenesis is initiated by the liver manufacturing apolipoprotein A1 (predominant form), in addition to other minority apolipoproteins that compose HDL structure. ATP-Binding Cassette Transporter A1 (ABCA1) will lipidate apolipoprotein A1 (ApoA1) with phospholipids, hence generating dense (high lipid:protein content) discoidal shaped pre- β HDLs with an average density: 1.06 – 1.21 g/mL (**Figure 1.3.3**).¹¹ One mechanism during RCT involves the transfer of

cholesterol from the blood and tissues onto the lipoprotein, specifically by lecithin-cholesterol acyl transferase (LCAT). This enzyme will esterify the cholesterol so it can nicely package the cholesterol into the lipoprotein scaffold. α -LCAT is specifically for promoting cholesterol esterification for HDL and β -LCAT facilitates esterification for the family of low- and very low-density lipoproteins (LDL and VLDL).¹⁷ The efflux of esterified cholesterol over time into the HDL core will form mature, spherical structures (**Figure 1.3.4**).

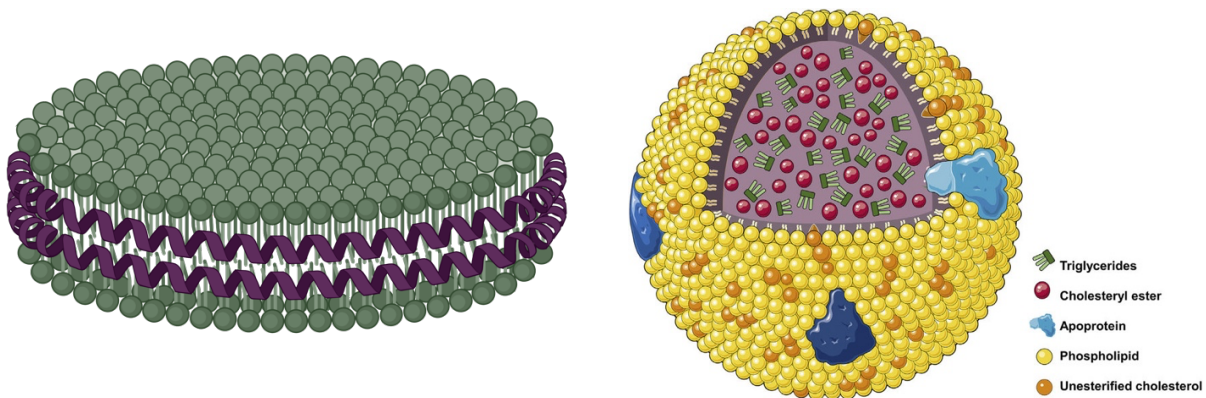


Figure 1.3.3: Pre- β discoidal HDL generated in the liver.

Figure 1.3.4: Structure of mature HDL after transport of cholesterol. Ref (18)

In addition to cholesterol transport, native HDL particles are known to inherently transport diverse cargo including many classes of lipids,¹⁹ proteins,²⁰ small molecules (hormones and vitamins),²¹ and even nucleic acids (microRNAs).²² Studies have identified that endogenous miRNAs are circulated in plasma and are protected from nucleases, and one mechanism for such protection is afforded by HDL particles. Indications as to how microRNAs can bind to the HDL include the formation of divalent cation bridges from the adsorption of the nucleic acid onto the zwitterionic phospholipid surface, which induces a conformational change of the lipids to help incorporate the nucleic acids into its space.²² This mechanism has been proposed to provide a shielding effect from nucleases, which in turn, can mediate the safe transport and delivery of functional miRNAs into cells to help regulate gene expression. Other studies performed by Wolfrum, et. al reveal that lipophilic siRNA preferentially associates with lipoproteins in serum,

and siRNA bound to HDL has enhanced uptake (up to 15-fold enhancement) compared to the delivery of cholesterol-siRNA alone.²³ These underlying principles serves as the basic framework for exploring, developing, and optimizing HDL systems as a carrier DDS for transporting nucleic acids, proteins, and other biological and small molecule payloads.

1.4: Advantages of HDL as a Transport Scaffold

As mentioned above, there are many different classes of NPs, and each type possesses certain distinct qualities. Usually, the benefit of a certain NP will also have a tradeoff that will restrict the NP for use only in specific drug therapies and targeting system that are receptive for the NP. However, the same cannot be stated for an HDL platform. HDL has multiple key features combined into a *single* platform, thus making it an attractive strategy for working with nucleic acids. The primary advantage of using HDL NPs for delivery pertains to the excellent biocompatibility and biomimicry due to the intrinsic roles of HDL within the body. HDLs help promote longer retention times without the need for chemical modifications (e.g., PEG) which can lead to potential immune responses.²⁴ Additionally, HDL can circumvent cytotoxic effects that can possibly arise from using metal nanoparticles such as gold, or polymeric nanoparticles such as chitosan.⁶

Previous clinical trials have demonstrated that HDLs can be safely tolerated in humans in high doses up to 30 g of HDL, and up to 135 mg/kg of the protein dose of the carrier itself with minor side effects concerning to increased liver strain because of cholesterol metabolism.²⁵ HDL are ultrasmall in size, with a diameter ranging between 6 – 15 nm and the thickness being ~ 5 nm. As with any small NPs, this endows the HDL with high surface areas which enables increased transport capacity for cargo, a substantial advantage over liposomes and LNPs. Notably, the small sizes of HDL are extremely consistent and is not significantly influenced by HDL remodeling as cholesterol is effluxed and undergoes changes in density and shape as it matures.²⁶ The relatively

stable and smaller sizes can help achieve tumor-selective delivery by simple diffusion mechanisms because of the leaky vasculature properties present in solid tumors.²⁴

In addition to passive targeting, HDL can interact with Scavenger Receptor B, Type I (SRB1) class of cell-surface receptors for direct, cytosolic delivery of its content, thereby evading endosomal entrapment and degradation.²⁷ This selective interaction does not require any external, costly modifications (e.g., antibodies) that is required for other classes of nanoparticles to achieve targeted delivery. In humans, HDLs will natively interact with SRB1 (in the liver) to deposit cholesterol into cells for metabolism. SRB1 is expressed in multiple cell types but is predominantly found in hepatocytes and cancer cells (**Figure 1.4.1**).²⁸ Naturally, this receptor functions as a docking site for HDL particles to bind (no consensus sequence required; binding is mediated through the multiple α -helices present in ApoA1) to deposit cholesterol removed from lipid-laden cells via ABCG1) for metabolism. Exogenous HDL assemblies present with a tropism towards SRB1,²⁹ and this active targeting strategy has formed the basis for studying the delivery of therapeutic nucleic acids over the past decade and half.

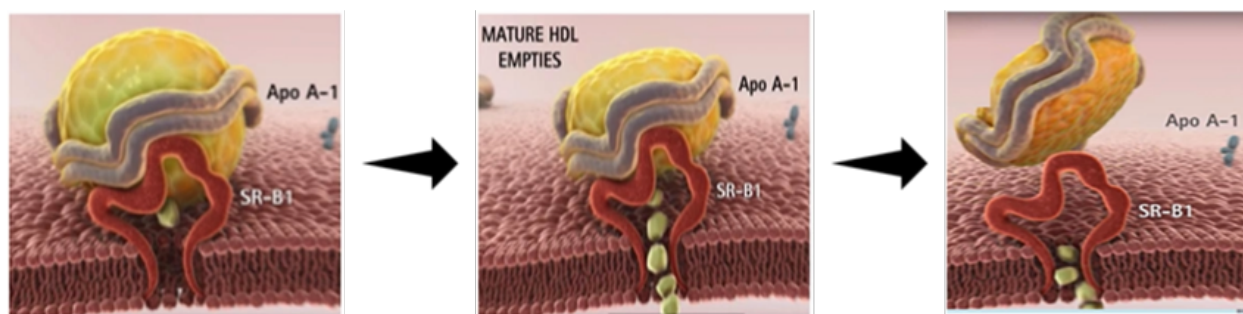


Figure 1.4.1: Mechanism by which HDL docks onto SRB1 and empty its contents directly into the cytoplasm of a [hepatocyte] cell. Figure adapted and modified from ref (28).

Lastly, exogenous HDL can be assembled using simple and reasonably cost-effective methods. As a note to the readers, in the literature exogenous HDL assemblies have a variable naming system and can be commonly referred to as a synthetic HDL (sHDL), reconstituted or recombinant HDL (rHDL), nanodisc (ND), HDL-mimicking peptide phospholipid scaffold (HPPS), HDL NPs, and/or HDL-mimicking NPs. The structure is rather modest and consist of phospholipids and Apolipoprotein A1 derivatives (protein or peptide mimetics), and multiple

clinical trials performed previously can attest to the scale-up and the GMP manufacturing capacity of NDs and its clinical translation potential.

1.5: Structural Properties of ApoA1 and ApoA1 Mimetic Peptides

Endogenous HDL particles are extremely diverse and multiple subclasses have been defined for HDL based on the variation in shape, the amount of cholesterol that is esterified, triglycerides, cargo that is present, and protein content. HDL composition is highly mutable as it is constantly undergoing remodeling because of its native role to transport and delivery a variety of cargo. The discoidal shape found in pre- β HDL accounts for $\sim <10\%$ of the HDL composition in the body at any given time.³⁰ All HDL particles, regardless of its heterogenous composition, contain ApoA1 as the defining scaffolding protein and comprises $>60\%$ of all protein content. Other minor constituents can also include other ApoA, ApoC, and ApoE families. The specific functional differences between each subtype are not well understood, however the pre- β and the differentiated subspecies are critical and highly involved in RCT

ApoA1 is manufactured and secreted by the liver and intestine. It is characterized as a 243 amino acid protein (MW: 28.1 kDa) that exists as a two-domain structure with 10 α -helices, 8 22-mers and 2 11-mers. It is classified as a class A helix because the amphipathic properties have the hydrophobic and hydrophilic residues in an opposed arrangement along the “long” axis.³¹ The N-terminus and the central region exists as a helix bundle whereas the C-terminus is a hydrophobic disordered random coil. The C-terminus is critical for human ApoA1 to initiate lipid-binding,³² and a segment containing residues 260 – 270 exists as an exposed hydrophobic surface to initiate the initial contact for lipid solubilization.³⁰ During HDL biosynthesis, ABCA1 will mediate vesiculation of a segment of a phospholipid bilayer (**Figure 1.5.1**) using an ATP driven phospholipid translocase to induce bending; this process does commonly occur in hepatocytes but can occur in any cell type with ABCA1. The C-terminus of ApoA1 will insert itself into defects

of the segment of a phospholipid bilayer vesicle. Upon contact with lipids, the binding of the C-terminus will transition from the unstructured random coils found in residues 179 – 236, as well as residues found in the intermittent regions at 45 – 53, 66 – 69, and 116 – 146, to an α -helix, thus giving rise to much of the helical content found in ApoA1.³⁰ This process is thermodynamically favorable as the binding of ApoA1 and helix formation to the lipids will increase the free energy of the lipid binding ($-42 \text{ cal}/\alpha\text{-helical residue}$) and consequentially increase the binding affinity by a couple orders of magnitude.³³ From there on, the N-terminus will unwind its helix bundles and form a continuous helical structure, separated by punctuating kinks at proline residues.³⁴ Once the bilayer has been solubilized with a critical concentration of α -helices, the bilayer will destabilize and collapse to relieve strain and form a discoidal structure.

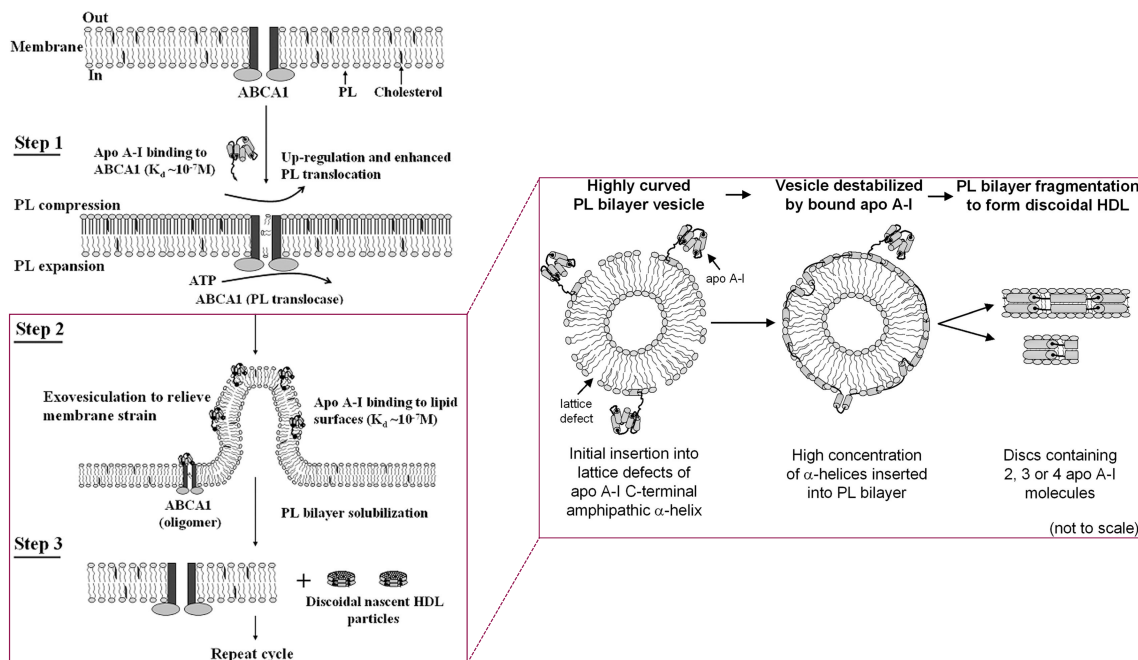


Figure 1.5.1: ABCA1 facilitated phospholipid vesiculation, followed by ApoA1 solubilization to form discoidal HDL particles during biogenesis. Figure adapted and modified from ref (30).

This is a highly sensitive and kinetically controlled process, and this structure will not form if excess cholesterol, and cholesteryl esters, or any triglycerides and other fatty acids are present.³⁰

Solubilization by the detergent-like properties present in ApoA1 leads to an arrangement of $\sim 2 - 3$ (3 if size is $> 10 \text{ nm}$) ApoA1 molecules in an antiparallel arrangement that scaffolds the lipids.³⁰

³⁵ This process can occur with any of the exchangeable apolipoproteins (including ApoE)³⁶ and

depending on the protein combination that is solubilizing the lipids, the lipoproteins complexes are fractionated based on the density (and size) of the structure produced. However, because of the diverse protein reactions that can occur to compose one HDL structure, the population of HDL is highly heterogeneous in the body (60 – 70% of the protein content is still ApoA1). Similar to the lipid-free state, ApoA1 has low stability (3 – 5 kcal/mol), indicating that this protein is highly flexible and can rapidly be unfolded and refolded.³⁰ The rapidly interchanging dynamic of ApoA1 is what allows the protein to reconfigure during the transition of cholesteryl esters for spherical HDL and this feature contributes to the remodeling processes of native HDL by lipases and transfer proteins. Upon the addition of cholesteryl esters, HDL will accommodate an extra ApoA1 for stability and form a double-belted arrangement consisting of mixed trefoil (Y-shape) and/or helical hairpin conformations on the scaffold.³⁵ This configurational adaptation helps maintain the smaller sizes of the particles on an ultimately curved surface.

Understandably, the functional levels of innate HDL can relieve cardiovascular stress and indications related to plaque. Previously, HDL levels were a common medical marker to assess risk for coronary artery disease. While this theory is currently dated as there are many components that contribute to high lipids, HDL levels are still a salient gauge for overall cardiac health. To that extent, pharmaceutical companies have devoted considerable time and interest to develop apolipoprotein mimetic peptides- a cheaper and scalable alternative to the full protein while still resembling the ApoA1 microenvironment to help boost HDL levels and RCT in serum.

As mentioned above, ApoA1 is a class A helix, and this helical property is represented in 6 of the 10 helices. The remaining 4 are class Y helices (3, 4, 9, 10) which closely resemble the class A helix structure but have a higher affinity towards lipids and contain additional positively charged residues at the polar interface (**Table 1.5.1**); class A helices have negatively charged amino acids oriented towards the polar edge and the positively charged amino acids towards the polar-nonpolar interface.³⁷ As also noted, the sequence of ApoA1 is fragmented into segments by

proline residues. All residues resemble amphipathic character that plays a key role for designing ApoA1 mimetic peptides.

Table 1.5.1: Residue distinctions for the full length human ApoA1 sequence. Residues are classified as a class A amphipathic helix except for when noted in blue, which is a class Y helix. Note that proline distinctions are in red and are responsible for breaking up the protein into different helical segments. Adapted and modified from ref (34).

Helix	Residue	Sequence
	1	DEPPQSP
Class G	8	WDRVKDLATVYVDVLKDSGRDYVSOF
	34	EGSALGKQLN
1	44	LKLLDNWDSVTSTFSKLREQLG
2	66	PVTQEFWDNLEKETEGRLRQEMS
3	88	KDLEEVKAKVQ
4	99	PYLDDFOKKWOEEMELYROKVE
5	121	PLRAELQEGARQKLHELQEKLS
6	143	PLGEEMRDRARAHVDALRTHLA
7	165	PYSDELRRORLAARLEALKENGG
8	187	ARLAEYHAKATEHLSTLSEKAK
9	209	PALEDLROGLL
10	220	PVLESFKVSFLSALEEYTKKLN
	242	TQ

By closely studying the physiochemical and biological properties imparted by the amphipathic residues, researchers have developed a suite of ApoA1 mimetic peptides, and the first design was composed of 18 amino acids and was termed as 18A (**Table 1.5.2**) and as its namesake, is prepared from 18 amino acids.³⁸ Due to the reversible and highly dynamic nature of ApoA1, sequence homology or any resemblance to native ApoA1 is not a necessary requirement for an amphipathic peptide to solubilize a phospholipid bilayer and mimic a pre- β HDL structure.³⁹ This criterion has widened the design space and discoidal lipid-peptide complexes can be prepared from any peptide that has detergent-like properties, like ones found on frog skin (Pxt-5).⁴⁰ Other than maintaining the key structural ordering of ApoA1, very few guidelines are in fact offered to generate a successful design, especially because assembly of discoidal complexes can be attained rather simply and is usually based on a rational sequence design. One of the limited considerations researchers have identified in the peptide design (which is typically 18 – 24 amino acids in length) is that helical formations are more conducive if there

are an equal number of positively and negatively charged residues appropriately distributed in the sequence (~ 3 – 4 residues of each type).⁴¹ Furthermore, lipid affinity is enhanced if the sequence is capped with an acetyl group at the N-terminus and an amide group at the C-terminus and these specific capping modifications at the termini can increase the hydrophobicity by promoting hydrogen bonds at the peptide backbone.⁴² If the goal of the peptide design is to promote RCT, researchers also suggest that the presence and ratio of certain amino acid residues need to be carefully moderated. These identified amino acids include methionine, tryptophan, lysine, and histidine. These residues can be inadvertently oxidized by myeloperoxidase at key positions on [certain] helix residues, under the presence of abundant atherosclerotic lesions and require a careful selection of the amino acid components during the design.³⁴ Furthermore, LCAT activity appears to be more pronounced if hydrophobic amino acids are positioned at select residues with consensus representation from helices 4 – 6,⁴³ with positively charged amino acids present at the C-terminus.⁴⁴ Preferentially mimetic peptides should be a net zero charge to retain amphipathic character.

While a full detailed review of the properties of therapeutic mimetic peptides designed to mimic and structurally resemble ApoA1 protein (for cardiac regulation) is outside the scope of the HDL function presented here (as a DDS for oligos), most of the peptides that have been developed are deemed as “successful” only if they can demonstrate one or more of the following properties: antiatherogenic activity, are anti-inflammatory, can attenuate atherosclerosis, are anti-oxidant and sequester oxidized lipids, can activate LCAT, promote cholesterol efflux, and is resistant to proteolysis.^{45, 46} These listed features suggest that simply binding of the lipid to the peptide is not sufficient to produce any therapeutic activity, and the peptide design should come as close as possible to resemble the benefits conferred by native HDL.⁴⁴ This was the case for 18A, as it failed to inhibit atherosclerosis. This peptide was further modified to yield the more prevalent 4F by swapping two leucines for two phenylalanines and switching to D-amino acids over L-amino acids to improve aromaticity and overall hydrophobicity, as well as proteolysis. A

representative list of different peptides that can be used to prepare mimetic HDL, sHDL, ND complexes are listed below in **Table 1.5.2**.

Table 1.5.2: Succinct representative list of mimetic peptides that have been used to form HDL mimicking structure. List is not exhaustive and includes a representative snapshot. Certain peptides were excluded (e.g., 3F) because of failed clinical potential, even though it did not fail to form HDL-like structures, however they are not used commonly today.

Name	# of Residues	Sequence	Reference
18A	18	DWLKAFYDKVAEKLKEAF	38
D-4F	18	Ac-DWFKAFYDKVAEKFKKEAF-NH ₂	47
ETC-642	22	PVLDLFRELLNELLEALKQKLK	48
5A	37	DWLKAFYDKVAEKLKEAFPDWAKAAYDKAAEKAKEAA	49
NSP	37	Ac-DWLKAFYDKVAEKLKEAAPDWFKAFYDKVAEKFKKEAF-NH ₂	50
PXT-5	14	FIQALLQWLLELLK-NH ₂	40
Monomer ₂₃	23	CGVLESFKASFLSALEEWTKKLQ-NH ₂	51
Monomer ₁₆	16	CGSFLSALEEWTKKLQ-NH ₂	51
-	22	NH ₂ -PVLESFKASFLSALEEWTKKLN-NH ₂	52
ELK neu	18	EKLKELLEKLEKLEKELL	53
ELK hyd	18	EKLLELLKLELLKELL	53
P12	20	FLEKLKELLEHLKELLTKLL	54

The *in vivo* data for some mimetic peptides such as 4F mentioned above modeled spectacular potential as an HDL infusion therapy to deplete blood cholesterol, but this activity did not translate in clinical trials and failed to elicit any significant anti-inflammatory, antiatherogenic, or any modulation effects for atherosclerosis (even for formulations using full length variations of ApoA1).^{45, 55} These challenges have caused pharmaceutical companies to place emphasis on other therapies, hence sequestering funding that is essential to keep the studies going. Mimetic peptides offer tremendous potential and enormous cost advantages and are still of broad scientific interest today. Nonetheless, the current mimetic peptide strategy suggests that there are other structural parameters of native human ApoA1 that are vital to incorporate during the rational design. However, due to structural differences between animal ApoA1 vs human apoA1, *in vivo* studies will need to be judiciously accounted for during pre-clinical testing to progressively

advance the future of therapeutic ApoA1 mimetic peptide. It is also very likely that the future of ApoA1 mimetics and exogenously delivered sHDL infusions maybe used in tandem and co-administered with other atherosclerotic interventions (e.g., cholesteryl esterase transfer protein inhibitors) especially because cardiac dysfunction does present with multiple abnormalities, and they must all be under control to achieve any therapeutic outcome.

Despite the setbacks for ApoA1 mimetic peptides for clinical use, the properties of and mimetic HDL complexes are not exclusive to atherosclerosis treatment and still resemble and retain key properties like native HDL. One such peptide includes ETC-642,⁴⁸ a peptide that was a chief constituent in this research study. ETC-642 was developed by Esperion Therapeutics (later acquired by Pfizer) and demonstrated LCAT activation and atheroprotective effects. Initial phase I clinical testing relayed that this peptide can be tolerated in a high dose (20 mg/kg) without impact to the liver as observed for the 30 mg/kg dose.⁵⁶ Further safety profiling was conducted however the results of the study have not been publicly disclosed, potentially because of the late-stage clinical failure of a cardiovascular drug by Esperion and Pfizer which led to further terminating the whole cardiovascular drug development program for the company. Overall, the encouraging results of this peptide has translated into being one of the more popular peptides (along with 4F) used when preparing any type of DDS using external assemblies. Additionally, ETC-642 (herein referred to as 22A) peptide does appear to closely encompass the native aspects of HDL, including SRB1 targeting and formation of homogenous assemblies with discoidal morphologies for the assembled platform.⁵⁷ Collectively, these results provided an appropriate framework for us to also pursue this peptide in our studies to develop a biomimetic DDS for DNA/RNA based drugs.

1.6: Phospholipids and Assembly Techniques for Synthetic HDL Structures

HDL composition varies within the body, and it is not restrictive to the different amounts of exchangeable apolipoproteins that maybe present in the scaffolded structure. Phospholipids that

comprise HDL do not consist of one single type of phospholipid, but rather a heterogenous mixture as that is what is found in cellular plasma membranes. Recapitulating artificial HDL assemblies (ND, rHDL, sHDL), whether it be through reconstitution from isolated ApoA1 or through mimetic peptides, is not representative of the intrinsic phospholipid compositions and consists of usually 1 – 3 phospholipid mixtures. Mechanistically, the kinetic process that drives the insertion of mimetic peptides to the lipid vesicles is analogous to what is shown in **Figure 1.5.1**. The process is kinetically controlled, and the peptide can only properly solubilize the lipid if the lipid is in a liquid-disordered state. Spontaneous assembly of the ND occurs when the lipid vesicles are above the transition temperature (T_m) bringing the lipids into a liquid-crystalline fluid state, hence introducing defects into the lipid structure.⁵⁸ The peptides will partition throughout the lipid vesicle kinks, effectively stressing it and collapsing the partitioned segments into discs (**Figure 1.6.1**). The transition temperature is very crucial, and no ND formations are observed at temperatures below the T_m of the lipid.^{58, 59} To form NDs using a mixture of lipids, it is important to ensure the temperature is above the T_m of at least one of the phospholipids that are present; although in the case of any natural lipids it may not be always possible to correctly pinpoint the accurate T_m . Furthermore, the size of the assembly can be controlled for by ensuring that the mimetic peptide is present in at least equal or preferably excess ratio from the lipid concentration.

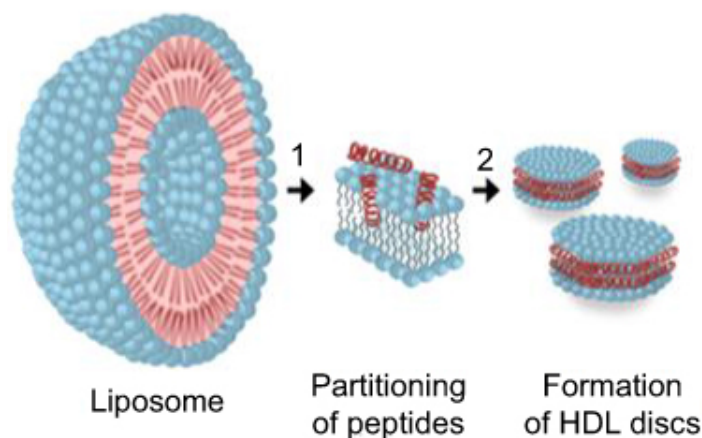


Figure 1.6.1: Solubilization of lipid vesicles using ApoA1 mimetic peptides. Ref (58)

A list of commonly used phospholipids for the preparation of rHDL and sHDL/NDs are listed in **Table 1.6.1**. A common phospholipid for synthetic preparations is DMPC (1,2-dimyristoyl-

sn-glycero-3-phosphocholine). DMPC has yielded great results for forming discs because of its room temperature T_m . Usually, no other steps are required other than mixing the vesicles with the peptide in an appropriate ratio to form the discs when this lipid is used. POPC (1-palmitoyl-2-oleoyl-glycero-3-phosphocholine) is another candidate that readily forms HDL-like assemblies because of its below room temperature T_m of $-2\text{ }^\circ\text{C}$. For lipids with a higher T_m above room temperature, such as sphingomyelins (SMs), the combined vesicle-peptide mixture will be subject to thermal cycling at temperatures above the T_m to facilitate the spontaneous assembly into discs.

Table 1.6.1: Phospholipids used to prepare HDL mimicking NPs. Information and structures as available from Avanti Polar Lipids.

Lipid (common abbreviation)	T_m ($^\circ\text{C}$)	Structure
DMPC	24	
POPC	-2	
DSPE	74	
DPPC	41	
DPPG	41	
SM/egg SM	40	
DSPC	55	
DOPC	-17	

It is important to note that functional ability of the HDL mimics based on the phospholipid composition can be impacted to some extent. Appropriate pharmacokinetics must be empirically

determined based on the mimetic peptide, the phospholipid, and any appropriate loading cargo for which these compounds will be developed. The impact for composition was especially notable and still is a consideration for designing sHDL for cardiovascular indications. sHDL prepared with DMPC and POPC (T_m below physiological temperature) had pronounced cholesterol efflux from macrophages, compared to DSPC or DPPC using the ETC-642 (22A) mimetic peptide.⁶⁰ Contrarily, it was also noted that the higher T_m phospholipids (DSPC or DPPC) showed longer half-lives *in vivo* compared to the DMPC and POPC. Higher T_m formulated sHDLs are also characteristically rigid at 37 °C, suggesting they are less susceptible for remodeling compared to lower T_m formulations and its fragile native HDL counterpart.⁶⁰ Furthermore, higher T_m phospholipids are better suited to encapsulate cargo within its smaller space. Therefore, depending on the phospholipid composition, the amphipathic peptide, and drug compounds the resulting sHDL/ND assemblies will need to be properly analyzed for the intent and purposes the scaffold is prepared for, but keeping in mind that there maybe tradeoffs for functionality vs. stability.

From the advent of ApoA1 mimetic peptides, the cost to prepare HDL-mimic scaffolds are cheap and preparation techniques are facile without the need for costly reagents or techniques. Assembly methods can be chiefly divided into three categories which include: 1) bulk self-assembly, 2) detergent-assisted assembly, and 3) microfluidics-based assembly. The underlying principle for all these methods is the same and require a combination of lipids and the peptide. Earlier versions of discoidal assemblies were prepared through [co-]lyophilizing a (dehydrated) mixture of lipids with the ApoA1 mimetic peptide, followed by buffer hydration.⁶¹ Depending on the concentration of the lipid component used, this may generate turbid solutions that can dissipate upon sonication or vortexing to break up the aggregates and facilitate solubilization. The more common technique utilized is as what has been described above. Lipid vesicles (either in the form of SUVs or MLVs) are prepared and discs are formed following solubilization of the vesicles at or above the lipid's T_m .⁶² This step can be followed by a thermal cycling if necessary

to assist solubilization and forming an emulsion of discs with a homogenous population.⁶⁰ The detergent method to prepare discs is quite like bulk assembly and differs with the addition of two steps. The dried lipid film that is obtained from lyophilization is hydrated with buffer and sodium cholate, which functions as a detergent to help introduce defects into the lipid vesicle.⁶³ Modulating the ratio of the detergent maybe necessary depending on the composition of the lipids used, though anywhere from a 1-fold to 2-fold excess of detergent to phospholipid ratio is added. The detergent will insert itself into the lipid layers and interact with the protein and the strain will cause the lipid to collapse to form the more thermodynamically favorable disc-like structure. The detergent is subsequently removed by extensive dialysis workups to yield discoidal complexes. This method has been classified as beneficial to embed any protein into the core of the membrane bilayer and use it to study structure-function interactions. The dialysis method does not completely remove the sodium cholate and there is a small fraction of remnant detergent particles,⁶⁴ thus deeming it unsuitable for drug delivery purposes. Conversely, some experts argue that this method produces more stable populations of discs, but the presence of even minor cholate compromises purity, and has shown toxicity at elevated doses in clinical assessments.⁶⁵ Nonetheless, this process has led to one HDL formulation (CSL-112) that is currently undergoing a phase III clinical trial.⁶⁶ Advanced microfluidic techniques address the challenges associated with batch-to-batch variability. This assembly style has been boasted as a solution that can facilitate large scale-ups (~420 mg per hour) at faster timescales without drastically altering the physiochemical properties associated with “benchtop” synthesis. The microfluidic devices have a central inlet that takes an input of a hydrophobic compound (i.e., lipid in an organic solvent) and two side inlets that will incorporate hydrophilic substances (i.e., ApoA1 or a mimetic peptide).^{67, 68} The chamber will generate microvortices allowing the organic and aqueous phases to combine generating lipid aggregates. The microvortices will coax the peptide or protein to solubilize the lipid aggregates to instantaneously form discs. This method is biologically relevant and advantageous because this system provides a pathophysiological microenvironment to mix and

assemble the precursors, making it useful to perform relevant screens specific to the system that is attempting to be commercialized. Note that any of these techniques can generate discoidal or the fully mature spherical HDL-mimics depending on the addition of cholesterol or cholesteryl oleate. The addition of cholesterol does help increase the fluidity of the lipid vesicles and prepare a more native-like structure. Spherical HDL has been additionally previously prepared from addition of gold nanoparticle core⁶⁹ or by constructing a DNA tetramer scaffold⁷⁰ to initiate assembly by adding phospholipids and ApoA1 protein. Each geometry may offer its own set of advantages, such as the spherical structure maybe regarded as more stable and can have enhanced cholesterol efflux but can increase liver trafficking and faster degradation through holoparticle endocytosis. Whereas the discoidal shape has a unique topology and ultra-small sizes that may make it easier to penetrate more difficult targets (e.g., tumors) and offer less energetic strain during internalization.⁷¹ While each preparation technique may offer one advantage over the other, the overall synthesis and preparation of these discs is rather simple and can be easily performed if the appropriate materials are available.

1.7: Shortcomings in Previous Renditions of HDL Mimics as a Nucleic Acid DDS

HDL is colloquially referred to as “Drano for the arteries” because of its fundamental role for clearing cholesterol in the blood. However, HDL has multiple occupations that arise from its role in transporting diverse cargo, an attribute that has also deemed HDL as a multivalent particle (**Figure 1.7.1**) that can be used to target multiple organ systems in the body.²⁵ HDL serves as a putative target for the transport of endogenous microRNAs (miRNAs) and functions to regulate HDL metabolism and gene expression for physiological processes.⁷² Many biological conditions favor the association of miRNA to the HDL. One such condition is the RNA bases can be easily accommodated and these bases tightly penetrate the membrane monolayer, potentially helping to shield from RNases.²² The associating property of miRNA also has biological implications, and

this can serve as a helpful diagnostic marker in which the profile of miRNAs being transported at any given time may vary, particularly during a disease state (and not just limited to cardiovascular indications).^{22, 72}

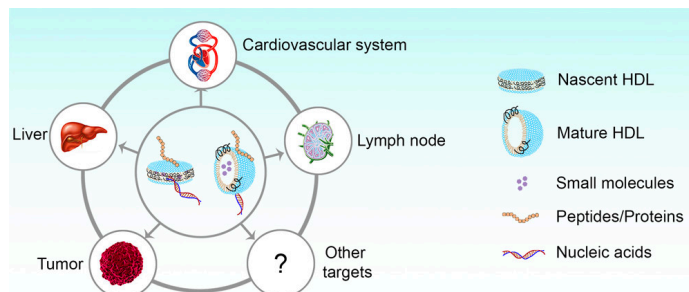


Figure 1.7.1: HDL and HDL mimicking particles can be used for multiple purposes, hence often referred to as a multivalent particle. Ref (25)

Initial studies revealed that siRNA was 15-fold more effective at gene silencing compared to just a naked siRNA-only administration on no scaffold.²³ It was also discovered at the same time that delivery of nucleic acids like siRNA and miRNA are highly dependent on SRB1, with up to 90% reduction in cellular internalization of siRNA and a 2-fold decrease in *in vivo* uptake in the steroidogenic organs, liver, and kidneys.^{22, 23} Expression and overexpression of SRB1 in multiple cell types and tumors have been rigorously evaluated.²⁸ The ability for tumors to express SRB1, most likely owing to high cholesterol demands from increased proliferation makes for selective tumor targeting especially lucrative.⁷³ These initial studies set the precedent for developing DDS for nucleic acids. However, the preliminary findings were discovered over 15 years ago, and while the genetic targeting capacity using ND scaffolds through siRNAs⁷⁴ and select other forms of nucleic acids, like peptide nucleic acids (PNA),⁷⁵ miRNAs,⁷⁶ and DNA,⁶⁹ has widened (**Table 1.7.1**), there have been no successful implementation as of this form of therapy, or even any clinical trials.

It is rather surprising to the broader scientific community as to why there have been no active clinical trials using a mimetic HDL scaffold.⁷⁷ There are numerous benefits to adopting such a system, but a closer analysis reveals a few setbacks that could be holding up advance testing. Barring any financial and disclosure provisions that could contribute to deferring trials, other

delays maybe owed to specific shortcomings in the design. The conjugation chemistry used to assemble these particles is based on weak, transient interactions (e.g., cholesterol^{69, 74, 78-80} and/or electrostatic interactions⁸¹). Despite the intrinsic property of HDL to modulate cholesterol and transport it in its core, the plasma half-life of cholesterol is indicated to be around 2 – 4 hours *in vivo*.²³ The lability of cholesterol is rather a common occurrence and does occur for tethered nucleic acids to lipid bilayer structures (large k_{off} rates).^{62, 82}

Table 1.7.1: List of gene targets that have been targeted by HDL mimicking or rHDL systems using nucleic acid therapeutics.

Gene	Nucleic Acid	Target System	Conjugation Chemistry	Reference
ApoB	siRNA	Liver	Cholesterol	23, 83
ApoM	siRNA	Liver	Cholesterol	23
PCSK9	siRNA	Liver	Cholesterol	83
FVII	siRNA	Liver	Cholesterol	83
SALL4	siRNA	Liver	Cholesterol	78
STAT3	siRNA	Tumor	Electrostatics	84 85
Bcl-2	siRNA	Tumor	Cholesterol	74, 79
OAT3	siRNA	Brain	Cholesterol	86
CpG	DNA	Immune System	Cholesterol	57
BACE	siRNA	Brain	Tocopherol	87
GAPDH	siRNA	HepG2 Liver Cells	Electrostatics	81
Pokemon	siRNA	Tumor	Cholesterol	88
VEGF	siRNA	Tumor	Cholesterol	89
miR-210	ASO	PC-3 Cells	Cholesterol	69
AR	siRNA	Tumor	Electrostatics	90
SHIP2	miRNA	Cornea	Electrostatics	76
NF- κ B	miRNA	Cornea	Electrostatics	76
VEGFR2	siRNA	Tumor	Cholesterol	91

The “pop off” ability for cholesterol-RNA or cholesterol-DNA does create difficulties in preparing a monodisperse population of oligonucleotide-disc conjugates, as the surface density can vary disc-to-disc and ultimately, batch-to-batch. Furthermore, only a small fraction of the dissociated nucleic acid will be due to internalization into the cellular cytoplasm of its intended target. However, other issues include premature dissociation which can lead to off-target effects and degradation, either through nucleases, cholesterol metabolism, or lysosomal pathways. These limitations require higher dosages to achieve therapeutic outcomes and can rapidly become very

expensive during scaleup for human trials. This problem is further propagated by the fact that each disc-like particle has overall a low and uneven oligonucleotide distribution, a critical and understated factor that can impact dosing across all levels (~ 8 – 10 copies of nucleic acid/disc observed maximally).^{74, 78, 83} The lower dosage form requires higher concentration and/or lengthy dosing regimens to achieve effective gene silencing *in vivo* and in humans. Delivery of larger doses (as high as the 8 – 30 mg/kg drug scale)^{78, 86} has been observed for certain situations involving siRNA delivery on a HDL mimicking scaffold. Other situations require that the oligonucleotide be delivered over multiple doses *in vivo* (murine models) to achieve therapeutic efficacy^{79, 84} at a much higher scale when compared to oligonucleotide delivery using other scaffolds,⁹² such as a gold nanoparticle. Arguably, one would argue that the dosing requirements are still much lower compared to naked administration, however there is much room for improvement to make this scaffold suitable for human use. Continuously injecting higher doses of drug leads to higher drug costs and increases the probability of suffering from many known and unknown side effects.

1.8: Summary and Scope of this Dissertation

The information presented in this chapter provided a preliminary overview of nucleic acid therapeutics, followed by ample background to understand how HDL mimicking NPs function as a biomimetic and how its unique design contributes as a therapeutic and delivery vehicle. We also provided an understanding of the competitive advantages this scaffold compare to other drug delivery systems and outlined some pitfalls in current state of the art for this technology as it pertains to gene regulation (and even cardiovascular disease). In Chapter 2 of this dissertation, we explore multiple covalent click chemistry techniques and identify the most conducive strategy that facilitates the oligonucleotide conjugation to a scaffold without significantly altering the structure and key properties of the scaffold. We determine whether this attachment can still retain a proof-of-concept model ASO's functional capacity (EZN2968) to regulate HIF-1- α in different

model cell lines. In Chapter 3, we will explain how the oligonucleotide density was augmented to its maximum potential for the ND scaffold using the chemical strategy developed in Chapter 2 and exploiting the ApoA1 mimetic peptide space, consequently creating a Nanodiscoidal Nucleic Acid (NNA). We assess the functionality of the NNA also using model cell lines, but we also embark on assessing its potential in a 3D tumor spheroid culturing system and *in vivo* efficacy in mice – the ultimate test, where we observe some powerful gene silencing of HIF-1- α , using a dose that is many-fold lower than the effective therapeutic dose as declared by original company that developed this nucleic acid. We wrap up and in Chapter 4 we explain the potential of the NNA as a therapeutic and its implication for use in virtually any disease state. We also highlight the potential areas for improving the NNA scaffold and explain how the NNAs can be further innovated upon to further amplify its powerful response in gene silencing.

Chapter 2

Gene Regulation Using Nanodiscs Modified with HIF-1- α Antisense Oligonucleotides

Adapted from Sharma, R.; Dong, Y.; Hu, Y.; Ma, V.-P.-Y.; and Salaita, K. Gene Regulation Using Nanodiscs Modified with HIF-1- α Antisense Oligonucleotides. *Bioconjugate Chem.* **2022**, 33, 279 – 293.

2.1: Overview

Delivery of nucleic acids can be hindered by multiple factors including nuclease susceptibility, endosome trapping, and clearance. Multiple nanotechnology scaffolds have offered promising solutions, and among these, lipid-based systems are advantageous because of their high biocompatibility and low toxicity. However, many lipid nanoparticle systems still have issues regarding stability, rapid clearance, and cargo leakage. Herein, we demonstrate the use of a synthetic nanodisc (ND) scaffold functionalized with an anti-HIF-1- α antisense oligonucleotide (ASO) to reduce HIF-1- α mRNA transcript levels. We prepared ND conjugates by using a mixture of phosphoglycerolipids with phosphocholine and phosphothioethanol headgroups that self-assemble into a $\sim 13 \times 5$ nm discoidal structure upon addition of a 22-amino-acid ApoA1 mimetic peptide. Optimized reaction conditions yield 15 copies of the anti-HIF-1- α ASO DNA covalently conjugated to the thiolated phospholipids using maleimide–thiol chemistry. We show that DNA-ND conjugates are active, nuclease resistant, and rapidly internalized into cells to regulate HIF-1- α mRNA levels without the use of transfection agents. DNA-ND uptake is partially mediated through Scavenger Receptor B1 and the ND conjugates show enhanced knockdown of HIF-1- α compared to that of the soluble ASOs in multiple cell lines (**Figure 2.1.1**). Our results demonstrate that covalently functionalized NDs may offer an improved platform for ASO therapeutics.

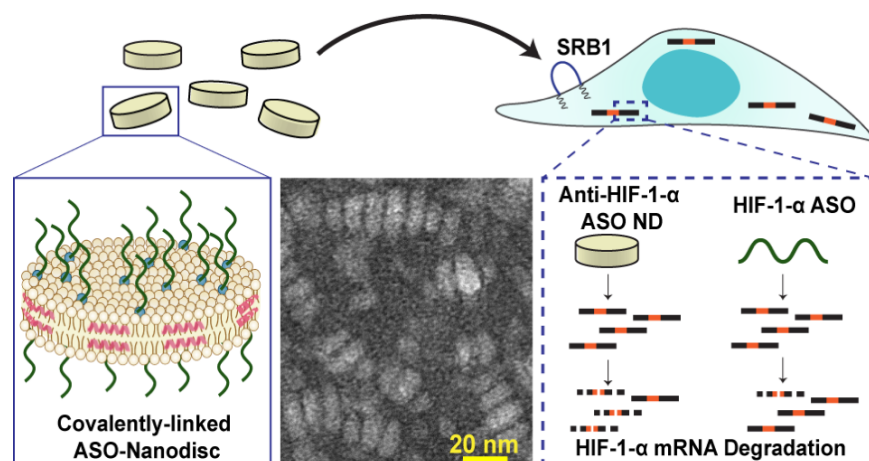


Figure 2.1.1: Overview of the oligonucleotide strategy used for this ND design and the heightened gene regulation potential provided by this ND design.

2.2: Introduction

Nucleic acid therapeutics have evolved into a highly attractive class of drugs that directly target the genetic basis for disease. One important type of nucleic acid drug is antisense oligonucleotides (ASO) typically comprising <20mer DNA or RNA nucleotides complementary to a target mRNA. There are only currently a handful of FDA-approved oligonucleotide drugs (**Table 1.1.1**), and a significant number are in clinical testing and early stage development. Despite this progress, ASO drugs have met setbacks in the clinic, in part, because of two main challenges.⁹³ The first pertains to the short half-life of these molecules due to the activity of endogenous nucleases.^{94, 95} The second major challenge is the highly charged backbone of DNA and RNA polymers that limits penetration across the plasma membrane.⁴ To reduce nuclease susceptibility, the phosphate backbone is typically modified with a phosphorothioate (PS) or methyl modifications, while the ribose is often modified with 2' methoxy or fluoro groups, as well as 2'–4' cross-links.^{96, 97} These modified oligos underlie the most recently FDA approved ASO drugs. Inadvertently, the PS modification also leads to protein interactions, which results in increased cellular uptake for particular tissues.^{2, 98, 99} Nonetheless, less than 1% of internalized DNA/RNA drugs reach the cytoplasm of the cell, and most are destroyed or trapped within endosomes.^{10, 100} Accordingly, any slight improvement in the delivery or stability of nucleic acid drugs will likely have a profound impact on the clinical application of such drugs. Indeed, thrombocytopenia, the depletion of platelets, is a common adverse event associated with the elevated dosing that is needed to achieve efficacy for ASO drugs.¹⁰¹ Hence, improving the delivery and nuclease resistance of ASOs will enhance efficacy, thus reducing costs, and facilitating clinical adoption.

One general approach to addressing these challenges is using nanoparticle scaffolds which can assist in cellular penetration as shown by Mirkin and others.^{69, 102, 103} Specifically, spherical nucleic acids (SNAs) ranging in size from 5 to 20 nm are ideally suited for delivery, because they escape clearance mechanisms and enhance cell uptake as shown in prior work.^{104,}

¹⁰⁵ Lipid-based nanomaterials are especially attractive because phospholipids offer high biocompatibility with facile and simple synthetic preparation techniques and minimal toxicity, in comparison to inorganic scaffolds, such as metal nanoparticles. Phospholipids will spontaneously self-assemble into liposomes, which are the most commonly investigated class of lipid nanoparticles for delivery. However, liposomes typically range from 30 nm to 2.5 μm in diameter, which leads to some level of clearance *in vivo*, and are best suited to encapsulate materials within their aqueous cavity. To enhance delivery, an ideal nanomaterial would be one that is small, ideally 10–60 nm⁹ in size, highly monodisperse, stable, and biocompatible.

Nascent high-density lipoprotein (HDLs) particles are well suited for delivery given their size, which is typically ~ 10 nm in diameter with a thickness of ~ 5 nm. As previously mentioned, HDLs are naturally occurring and play a prominent role in delivering cholesterol to the liver through reverse cholesterol transport. In addition to cholesterol transport, HDL is commonly referred to as a multivalent particle (**Figure 1.7.1**) because of its inherent role in transporting and delivering various molecular cargo including nucleic acids (miRNAs) through its non-endocytic mechanism of Scavenger Receptor B1 (SRB1) delivery,²⁷ thus highlighting its natural role as a delivery vehicle. While the nascent HDL particles are composed of ApoA1, phospholipids, and several other minority component proteins, the structure of HDLs can be easily recapitulated using specific phospholipids and short ApoA1- mimetic peptides,^{57, 58} herein referred to as synthetic nanodiscs (NDs). The advantages of using NDs for delivery include a facile and scalable synthesis, biocompatible composition, and evasion of clearance because of their sub-20 nm size. Additionally, NDs can also transfer their content directly into the cytoplasm of a cell via SRB1, bypassing endosomal entrapment.⁸⁸ SRB1 is commonly expressed in many cellular subtypes, hence widening the realm of possibilities for targeted delivery. Furthermore, nonspherical nanoparticles such as NDs may also offer a lower energetic barrier for internalization,⁷¹ thus enhancing cell delivery. Therapeutic oligonucleotides, such as siRNA,^{23, 78, 86, 87, 90, 106} DNA,^{57, 69,}
¹⁰⁷ PNA,⁷⁵ and miRNA,⁷⁶ are typically anchored onto NDs using noncovalent linking strategies

through cholesterol tagging^{69, 78, 88, 91} or electrostatic attraction^{75, 76, 81, 84} using NDs assembled with positively charged phospholipids or polylysine. One of the challenges in using ND for oligonucleotide delivery pertains to the labile nature of these interactions, which leads to instability of the conjugates. For example, the observable k_{off} between cholesterol-labeled oligonucleotides and phospholipid membranes is reported as $\sim 10^{-2}$ to 10^{-3} /s (ref¹⁰⁸) and hence offers short half-lives, $t_{1/2}$ of ~ 1 – 10 min. Another problem with the noncovalent assembly of ND–nucleic acid conjugates is the low density of oligonucleotides, which has been optimally reported as ~ 1 – 8 oligonucleotides per ND.^{74, 78, 83} It is thus desirable to generate covalently linked ND–nucleic acid structures with greater densities of nucleic acids to boost their ASO activity.

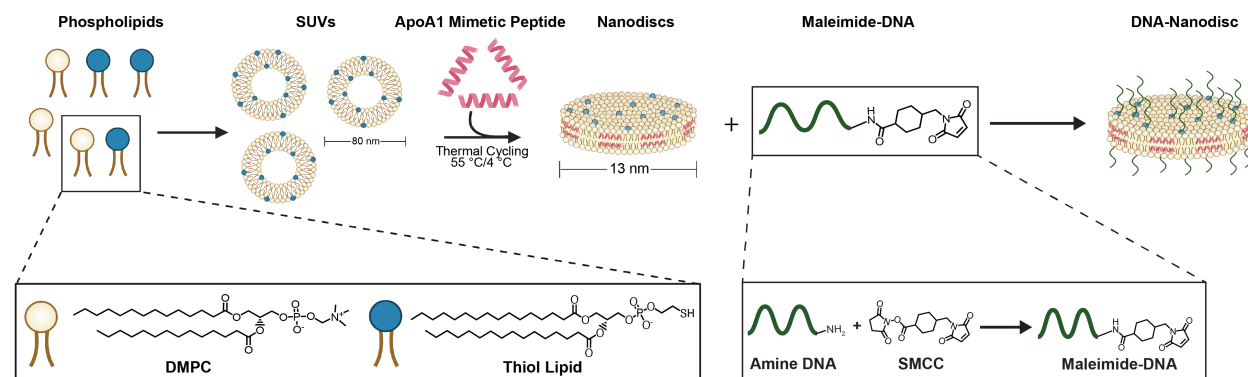
Herein, we address these problems and generate covalently linked ASO-ND conjugates with the greatest reported density of DNA, to the best of our knowledge. Specifically, we tested a range of bioconjugation methods and identified the maleimide–thiol Michael addition chemistry as the most favorable. By titrating different thiol phospholipid concentrations and various reaction conditions (temperature and pH), we were able to boost the density of DNA to maximally 15 copies/ND while maintaining the NDs ultrasmall size and monodispersity. Importantly, we found that ND conjugation afforded enhanced nuclease resistance. As a proof-of-concept, we studied the uptake and efficacy of ND conjugated to a clinically relevant ASO that targets hypoxia inducible factor 1 alpha (HIF-1- α). We tested this particular ASO because it was evaluated in phase 1 dose escalation studies in patients with advanced solid tumors and showed no dose-limiting toxicities.^{109, 110} Our results show that ASO-NDs are taken up by a variety of cell types and internalization is SRB1-dependent. ASO-NDs are also highly active in knocking down HIF-1- α in a time- and concentration-dependent manner. On an ASO-basis, our ND-conjugation approach affords ~ 3 -fold improvement in knockdown of HIF-1- α in HeLa cells (75 nM of the ASO, 24 h) when compared to the ASO itself, which represents a marked enhancement in drug efficacy.

Overall, our work describes a facile and easily adaptable conjugation strategy for linking ASO drugs to NDs that may potentially enhance efficacy.

2.3: Results and Discussion

2.3.1 Incorporating and Assembling Thiol-Functionalized NDs

NDs were prepared from small unilamellar vesicles (SUVs) comprised of 1,2-dimyristoyl-sn glycerol-3-phosphocholine (DMPC) and 1,2-dipalmitoyl-sn-glycerol-3-phosphoethanol (referred to as thiol lipid). To self-assemble the NDs from the SUVs (1 mL of lipid at 2.5 mg/mL), 751 nM of ApoA1-mimetic peptide (PVLDFRELLNELLEALKQKLK) was incubated with the SUVs and the samples were subjected to thermal cycling (**Scheme 2.3.1**).



Scheme 2.3.1: Protocol for preparing and assembling DNA-ND conjugates. NDs are formed by preparing 80 nm small unilamellar vesicles (SUVs) primarily using DMPC as a major component and the thiol phospholipid as a minor component (~10%). A short 22 amino acid peptide ApoA1 mimetic is added to SUVs before subjecting them to thermal cycling between 55 °C and 4 °C to form NDs. DNA bearing a maleimide group is chemically conjugated to the thiol NDs resulting in the DNA-ND conjugate. The product is purified by using size exclusion chromatography.

In preliminary experiments, we tested strain-promoted Cu-free click reactions to couple nucleic acids to NDs. However, these methods generated low DNA conjugation yields in our hands and were not pursued further (**Figure S2.6.1**). Instead, we found that coupling between maleimide-activated DNA to a thiolated ND produced the most promising initial yields. Therefore, we first aimed to optimize the coupling efficiency by determining the maximum density of the thiolated lipids that could be incorporated into the ND. We tested a range of molar percentages (5% - 20%) of thiol lipids and assessed the ND structure using transmission electron microscopy (TEM). We

observed that 5 mol% and 10 mol% thiol-NDs (**Figure 2.3.1a**) displayed a monodisperse morphology, whereas the 20 mol% thiol-NDs showed aggregation and broadening of ND size (**Figure S2.6.2**). We postulate that the thiolated lipids can lead to the formation of disulfide bonds, prompting aggregation. Moreover, the thiolated lipids have a longer lipid tail which may contribute to the observed aggregation. Quantification of TEMs indicated that ND diameters slightly increased with increasing thiol lipid content (**Figure 2.3.1a**), though the values are not significant. For example, the 0% thiol ND had a diameter of 11.9 ± 2.8 nm and this increased to $12.1 \text{ nm} \pm 2.3$ nm for 5 mol% thiol ND, and $12.5 \text{ nm} \pm 1.8$ nm for the 10 mol % thiol NDs. As expected, the ND thickness seemed independent of thiol concentration and was approximately 4.4, 4.5 and 4.7 nm for the 0%, 5%, and 10% thiol lipid ND particles respectively. Moreover, the ND thickness and diameter were consistent with the reported dimensions for DMPC bilayers and other NDs generated using different protocols,^{50, 52, 111-113} confirming that the ND structures formed appropriately and likely adopted the structural beltlike conformation reported in other literature. We were able to distinctly visualize the top and side views of NDs and these distinct structural differences confirmed the disc-like configuration typical of nascent native HDL and NDs. We also observed ND “coin-like” stacks ascribed to the “rouleaux effect,” a common artifact of the negative staining process in TEM due to the interaction of the negatively charged particles in the stain with the choline headgroups during the drying process.^{52, 114}

2.3.2: ND Conjugation to DNA

In order to facilitate a maleimide-thiol linkage onto the surface of ND, an amine-terminal DNA was modified with a maleimide group bearing a hetero-bifunctional linker, succinimidyl 4-(N-maleimidomethyl)cyclohexane-1-carboxylate (SMCC). For our initial proof-of-concept studies, we chose to prepare DNA-ND conjugates by using a deoxyribozyme (DNAzyme) as a model nucleic acid which has catalytic activity that is highly sensitive to the local environment.¹¹⁵ The maleimide-activated DNAzyme (DNA) was then coupled to the surface of NDs (**Scheme 2.3.1**) which were

first treated with tris(2-carboxyethyl)phosphine (TCEP) to reduce the thiols. We measured the DNA density on NDs using the OliGreen™ assay (see **2.5: Materials and Methods**) and compared densities for NDs displaying 5 and 10 mol % thiol lipids under standard reaction conditions (RT, pH 7.4, 2 h).

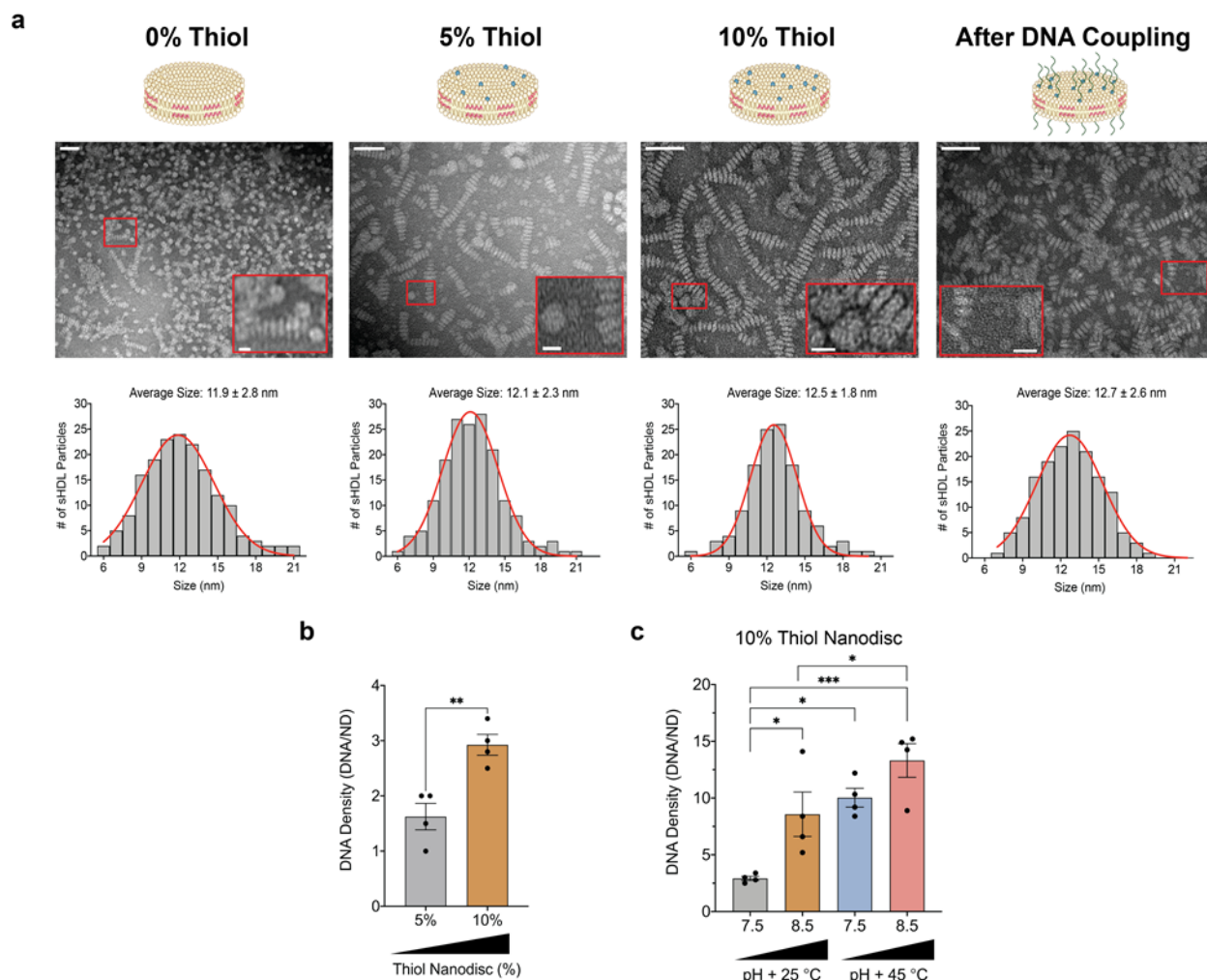


Figure 2.3.1: Coupling and optimizing DNA onto the ND surface. **(a)** TEM images (top) and binned size analysis (bottom, $n = 170$ NDs from 3 different images for each group) of NDs comprised of DMPC only, 5% thiolated lipid, 10% thiolated lipid, and after DNA is coupled onto a 10% thiol ND surface. Scale bar: 50 nm, inset: 30 nm. Samples were prepared using a plasmon-etched 400-mesh copper grid and staining was performed using Nano-W™. Diameter differences between each ND group is not statistically significant. **(b)** Plot comparing DNA density of DNA-ND conjugates consisting of NDs with 5% thiol or 10% thiol. The 10% thiol ND shows a greater DNA density (3 DNA/ND vs 1.6 DNA/ND for 5%) at standard reaction conditions: 25 °C, pH 7.4. **(c)** Plot comparing the DNA density on 10% thiol ND after testing different pH (7.5 and 8.5) and temperature (25 °C and 45 °C) conditions. There is an average increase in DNA density from 3 ± 0.5 DNA/ND to 13 ± 2 DNA/ND under the improved conditions. Each data point represents one independent replicate. Error bars represent SEM of $n = 4$ independent replicates and * $p < 0.05$, ** $p < 0.01$, *** $p < 0.001$.

As expected, NDs composed of 10 mol % thiol lipids displayed a greater DNA density compared to the 5 mol % (**Figure 2.3.1b**). These results prompted us to optimize the coupling conditions

(Figure 2.3.1c) by varying temperature (25 °C and 45 °C) and pH (7.4 and 8.5). Elevated temperatures in combination with a more basic pH resulted in an average DNA density (13 ± 2 DNA strands/ND). We did not increase the pH and temperature further to avoid disrupting the ND structure and activating lysines in the ND. Note that this coupling strategy and conditions resulted in DNA densities that significantly exceed that of cholesterol tagged siRNAs. We also confirmed through TEM that DNA modification and exposure to higher temperature and pH conditions did not alter the structure of the ND (Figure 2.3.1a), signifying that the structure-dependent properties of DNA-ND remain intact and still resemble that of discoidal pre- β HDL.

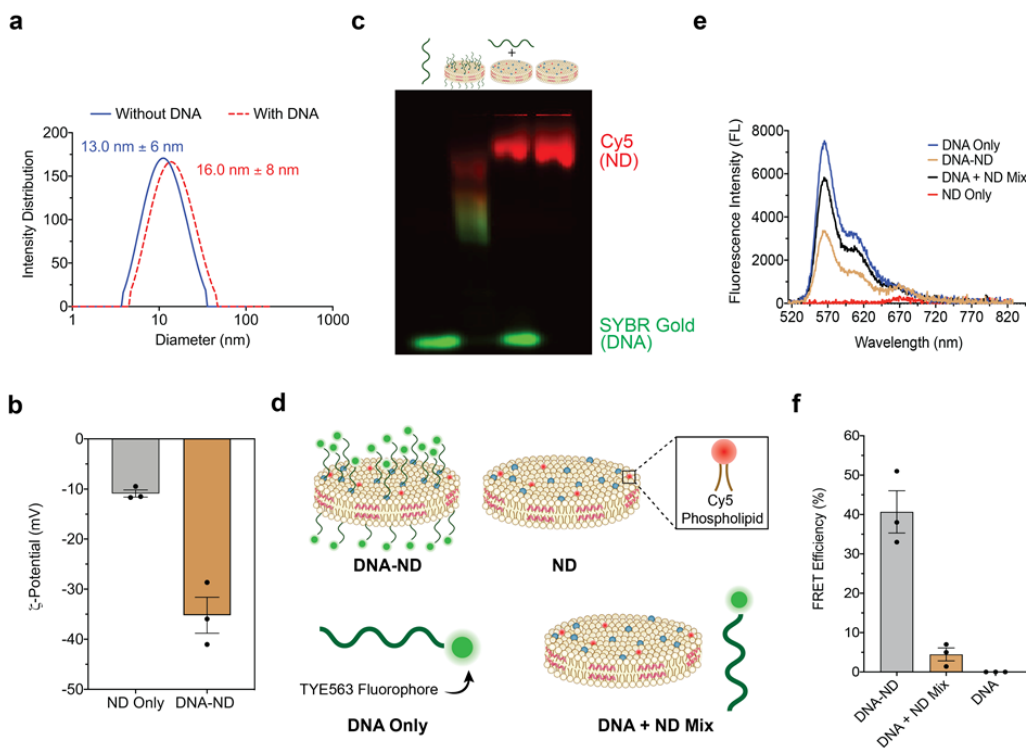


Figure 2.3.2: Validating and characterizing the attachment of DNA onto the surface of ND. **(a)** DLS graph indicating a shift in the hydrodynamic radius from 13.0 nm to 16.0 nm after the conjugating DNA to the ND. Size distribution profile is representative graph of a typical sample ($n = 3$ independent experiments) containing ND or ND with DNA conjugate. **(b)** Zeta-potential graph showing the increase in negative charge from -10.9 mV to -35.2 mV after DNA is coupled onto the surface of the ND. **(c)** Gel electrophoresis of four samples (L to R): DNA only, DNA coupled to ND, DNA mixed with ND, and ND only. NDs were prepared using a Cy5 phospholipid and the gel was prepared using 1.5% agarose, in-gel staining using SYBR™ Gold and TAE buffer. The gel ran for 90 min at 85 V before imaging using a laser scanner. There is a retardation of DNA once attached to the ND compared to the unbound DNA lanes. **(d)** Schematic representation showing the different samples: DNA only, ND only, DNA-ND, and DNA mixed with NDs that were used for the FRET assay. TYE labeled DNA and Cy5 labeled phospholipid NDs were used for FRET. **(e)** Fluorescence spectra of the four groups illustrated in **(d)** when excited at $\lambda = 520$ nm. DNA was measured at a concentration of 100 nM while 8 nM ND concentration was used to best match the ND and DNA + ND mix concentration in the DNA-ND sample. **(f)** Plot of the calculated FRET efficiency of the chemically conjugated DNA-NDs compared to the unlinked DNA and ND mixture. The higher FRET efficiency (40.1%) of the DNA-ND compared to the mixed control (4.5%) further substantiates that DNA is bound onto the surface of the ND. Each data point represents one independent replicate. Error bars represent SEM of $n = 3$.

We next performed a set of experiments to validate DNA conjugation to the ND. DLS indicated a shift in the hydrodynamic radius after coupling with DNA (**Figure 2.3.2a**) and the average size of NDs increased from $13 \text{ nm} \pm 4 \text{ nm}$ to $15 \text{ nm} \pm 7 \text{ nm}$ ($n = 3$ independent replicates). ζ -potential measurements showed a drastic shift from -10.9 mV to -35.2 mV (**Figure 2.3.2b**) after DNA conjugation, indicating the presence of negatively charged nucleic acid on the surface of the ND. We also used agarose gel electrophoresis to confirm covalent conjugation of the DNA in samples that had Cy5-tagged lipids (**Figure 2.3.2c**). The ND-conjugated DNA showed a marked retardation in migration compared to soluble DNA. In contrast the ND band migrated more rapidly as a result of DNA conjugation, which is consistent with an increase in charge density as a result of DNA conjugation. Notably, we did not observe any changes in the bands when DNA was mixed with the ND, indicating weak if any electrostatic interactions (**Figure 2.3.2c**). The smear-like pattern in the DNA-ND sample is likely due to a distribution of DNA densities on each ND as well as disruption of the ND as it migrates in the gel. DNA-ND conjugates are highly stable in solution for up to 3 weeks at $4 \text{ }^\circ\text{C}$, as confirmed by DLS measurements (**Figure S2.6.3**). FRET measurements further confirmed direct DNA conjugation to the ND (**Figure 2.3.2d**). Here, we tagged the short anti-HIF-1- α ASO (**Table S2.6.2**) with a TYE563 donor fluorophore while the ND incorporated a Cy5 acceptor fluorophore. Donor emission spectra showed that DNA conjugation led to a significant reduction in donor emission intensity when compared to donor only sample or samples that mixed the DNA with the ND (**Figure 2.3.2e**). The calculated FRET efficiency was 40% for the DNA-ND conjugate and 5% for the mixture of the DNA and ND (**Figure 2.3.2f**). The relatively moderate FRET efficiency is because the acceptor is not directly attached to the TYE-labeled DNA. Rather the donor (TYE-DNA) and the acceptor (Cy5 phospholipids) are localized to the same ND, and thus the FRET efficiency reflects the statistically averaged donor-acceptor distance. Collectively, these results establish that the DNA is chemically linked to the ND, prompting us to next investigate the activity of the DNA-ND conjugates and their nuclease resistance.

2.3.3: DNA bound to the surface of the ND is functional and nuclease resistant

Recent work has shown improved therapeutic potential for DNAzymes further motivating these sets of experiments.^{116, 117} For our experiments, we used a novel DNAzyme sequence that has been identified in our lab. We measured the activity of the DNAzyme containing the catalytic loop derived from the 10-23 DNAzyme^{92, 103, 115, 118, 119} against a fluorogenic substrate.

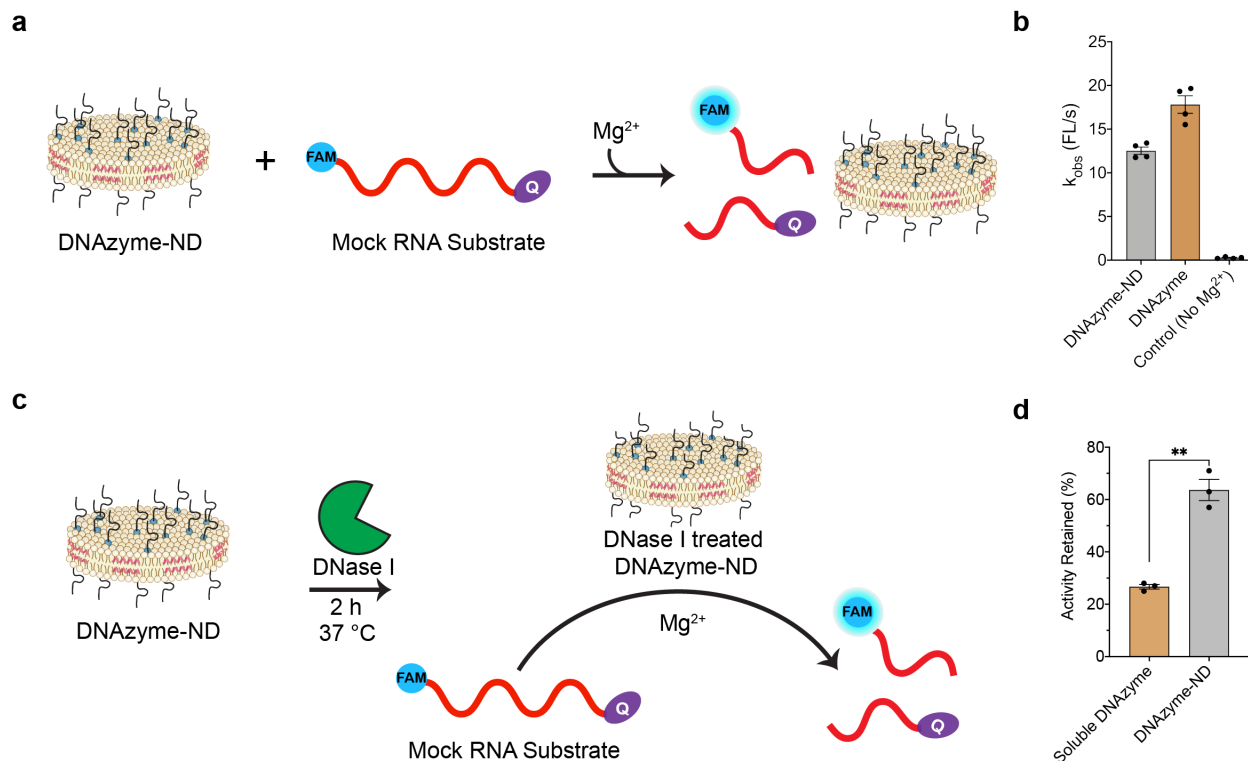


Figure 2.3.3: DNA conjugated to the surface of the ND is catalytically active and nuclease resistant. **(a)** Scheme depicting the fluorescence assay used to assess catalytic activity using a DNAzyme-ND and a fluorogenic mock RNA substrate. Under the presence of Mg^{2+} , the DNAzyme will cleave the quenched substrate, leading to an increase in fluorescence. **(b)** Plot showing the difference in k_{obs} for the cleavage assay using the soluble DNAzyme, DNAzyme-ND, and a control with no magnesium in the buffer. The DNAzyme only group showed the highest cleavage rate, followed by DNAzyme-ND. Error bars represent SEM of $n = 4$. **(c)** Scheme showing the treatment of the DNAzyme-NDs with DNase I for 2 h prior to measuring catalytic activity using the fluorogenic mock RNA substrate. **(d)** Plot showing the relative activity retained after DNAzyme-ND conjugates and soluble DNAzymes were treated with DNase I for 2 h at 1 U. The ND scaffold afforded greater protection against DNase I as it retained higher activity, 64%, compared to the soluble nucleic acid which only retained 27%. Each data point represents one independent replicate. Error bars represent SEM of $n = 3$ and ** $p < 0.01$.

To achieve multiple turnover kinetics, the kinetic measurements employed a 10-fold excess of the substrate compared to the DNAzyme-ND (or soluble DNAzyme). The nucleic acid substrate was dual labeled with a FAM fluorophore at the 5' terminus and an Iowa Black® quencher at the 3' terminus (**Figure 2.3.3a**). The FAM fluorescence intensity (FL) was monitored over a 4 h time

period (**Figure S2.6.4**) and fits of these plots provided the k_{obs} rate constants. We found that DNAzyme-ND conjugates displayed ~34% loss in activity compared to the soluble DNAzyme (**Figure 2.3.3b**) possibly due to sterics imposed by the ND surface.¹²⁰ Importantly, the ND afforded nuclease resistance, as DNAzyme-ND conjugates retained 64% of their activity after treatment with DNase I for 2 h, while the soluble DNAzyme only preserved ~27% of the activity after the same nuclease treatment (**Figure 2.3.3c-d**). Thus, the ND scaffold offers a suitable and robust candidate for delivery therapeutic nucleic acids. This is not surprising as this structure resembles a nascent HDL scaffold that is known to offer protection against nucleases.⁶⁹ These results prompted us to investigate the uptake mechanisms and functional activity *in vitro*.

2.3.4: ASO-ND conjugates are internalized in a dose- and time-dependent manner

For our *in vitro* studies, we transitioned towards using a clinically relevant ASO target as a test bed model to investigate the potential of ND conjugation in enhancing the function of validated ASOs. Our goal here was to quantify the uptake of ASO-ND conjugates using model cell lines (**Figure 2.3.4a**). We first incubated HeLa cells with ASO (anti-HIF-1- α ASO, see **Table S2.6.2** for sequences used in this study) and phospholipid dual-tagged fluorescent ASO-ND conjugates for 3, 12, and 24 h. Then cells were washed and imaged by confocal microscopy (**Figure 2.3.4b, Figure S2.6.5a**). We observed accumulation of ASO and phospholipid scaffold inside the cytoplasm of the cells (**Figure S2.6.5b**) but were excluded from the nucleus. Importantly, ASO-ND conjugates were primarily localized to the cell edge at 3 h, indicating the cargo was associated with membrane and possibly trapped in early endosomes. The Pearson's coefficient for colocalization between the phospholipid and ASO was significantly higher than that measured for control samples containing a mixture of NDs and ASO at all time points (**Figure 2.3.4c**). This shows that a significant subset of ASO-ND conjugates remain intact upon cell uptake. As expected, there is a decrease in colocalization at 24 h, indicating disassembly of the ASO-ND conjugates at later time points.

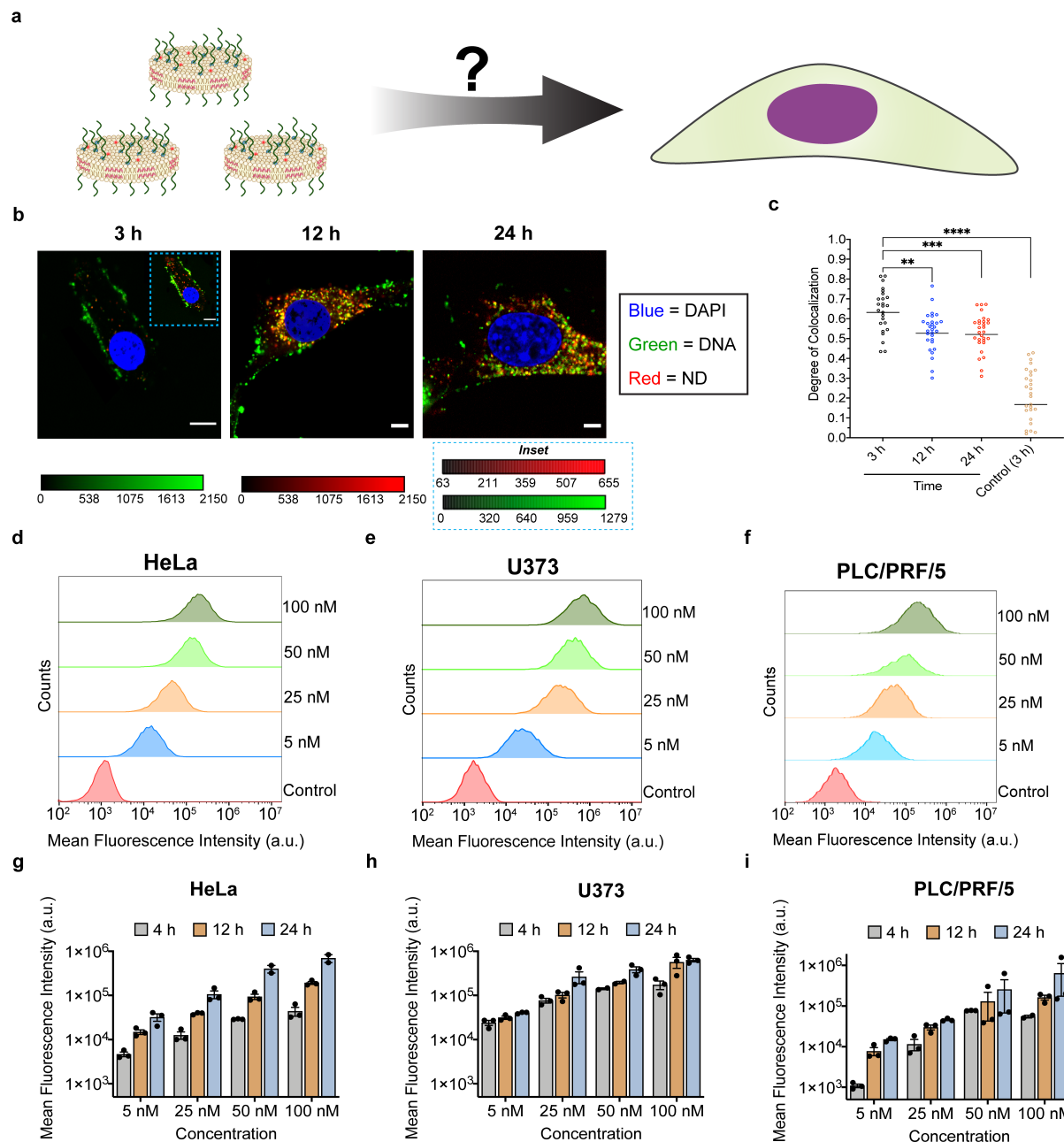


Figure 2.3.4: ASO-ND show uptake into HeLa, U373, and PLC/PRF/5 cells in a dose and time-dependent manner. **(a)** Scheme showing the possibility for ASO-ND to be internalized into cells. **(b)** Representative confocal microscopy images showing a time course for the uptake of 100 nM ASO-ND into HeLa cells. ASO was labeled with a TYE dye and the NDs were labeled with a Cy5 phospholipid. Cells were fixed and stained with DAPI before acquiring images with a 60 \times oil objective. Scale bar: 5 μ m. **(c)** Pearson's colocalization coefficient analysis of TYE and Cy5 signal in $n = 25 - 30$ cells for each group. Analysis indicates the increased detachment of ASO from the ND within 12 h. Representative flow cytometry histograms at 12 h for **(d)** HeLa, **(e)** U373, and **(f)** PLC/PRF/5 cells that were treated with the indicated concentration of the ASO-ND and rinse prior to the measurement. Flow data represents intensities for a minimum of 5000 cells. Increase in uptake of ASO-ND over time measured at 4, 12, and 24 h as measured from the mean intensity from flow cytometry in **(g)** HeLa, **(h)** U373, and **(i)** PLC/PRF/5 cells. Each data point represents one independent replicate. Error bars represent SEM of $n = 3$ and ** $p < 0.01$, *** $p < 0.001$, **** $p < 0.0001$.

We observe the presence of both ASO and ND puncta which indicates that there are likely multiple populations of ASOs. Likely, a subset of ASOs are entrapped within endosomes, which

would appear as puncta. Another population that appears as puncta is likely in the form of assembled phospholipid-ASO structures that have been internalized using the primary SRB1 uptake pathway for the NDs.⁸⁰ Additionally, because we used PS-modified ASOs, it is possible that the DNA was trafficked inside the cell using multiple productive and nonproductive entry pathways that would appear as puncta.¹²¹ Since the DNA is lipidated, puncta may be associated with membranes such as the ER, nuclear membrane, mitochondrial membrane, plasma membrane, and other vesicle-like structures.¹²²

We further investigated uptake of ASO-ND conjugates across multiple cell lines. Dose-dependent and time-dependent uptake into HeLa cells, U373 cells, and PLC/PRF/5 cells were quantified by incubating with fluorescently tagged ND and ASO-ND at varying concentrations (0 nM – 100 nM) for different lengths of time (4 h – 24 h) prior to analyzing cells by flow cytometry. Both the scaffold (**Figure S2.6.6**) and the ASO-ND (**Figure 2.3.4d-i**) were taken up by the different cells in a similar dose- and time-dependent manner. It has been reported that NDs can be tolerated at higher doses, compared to other nanoparticle scaffolds such as AuNPs and PEGylated liposomes.²⁵ Hence, at the ASO-ND concentrations tested, we do not observe saturation of uptake, suggesting that it may be possible to dose these conjugates at yet greater concentrations to further boost mRNA inhibition.

2.3.5: The uptake of thiol NDs and ASO-NDs into cells is partially mediated by Scavenger Receptor B1

To elucidate the role of SRB1 in uptake, we performed RT-qPCR on HeLa, U373, and PLC/PRF/5 cells to confirm the expression of SRB1 (**Figure S2.6.7**). SRB1 levels were quantified relative to wildtype Huh7 cells, a known expressor for SRB1, as a positive control. The cell line panel was incubated with an inhibitor for SRB1 (**Figure 2.3.5a**), blocker of lipid transport-1 (BLT-1) before treatment with ND or ASO-ND for 2 h and measuring fluorescence intensity using flow cytometry. Fluorescence intensity of the inhibited cells were compared against cells that were treated with ASO-ND (**Figure 2.3.5b-d**) or ND (**Figure S2.6.8**) but no inhibitor. BLT-1 treated cells

displayed reduced uptake compared to the cells treated with ND only, without BLT-1 (**Figure S2.6.9**). Notably, we observed that generally ASO-ND displayed more uptake compared to ND only (**Figure 2.3.5e**) after blocking the SRB1 receptor.

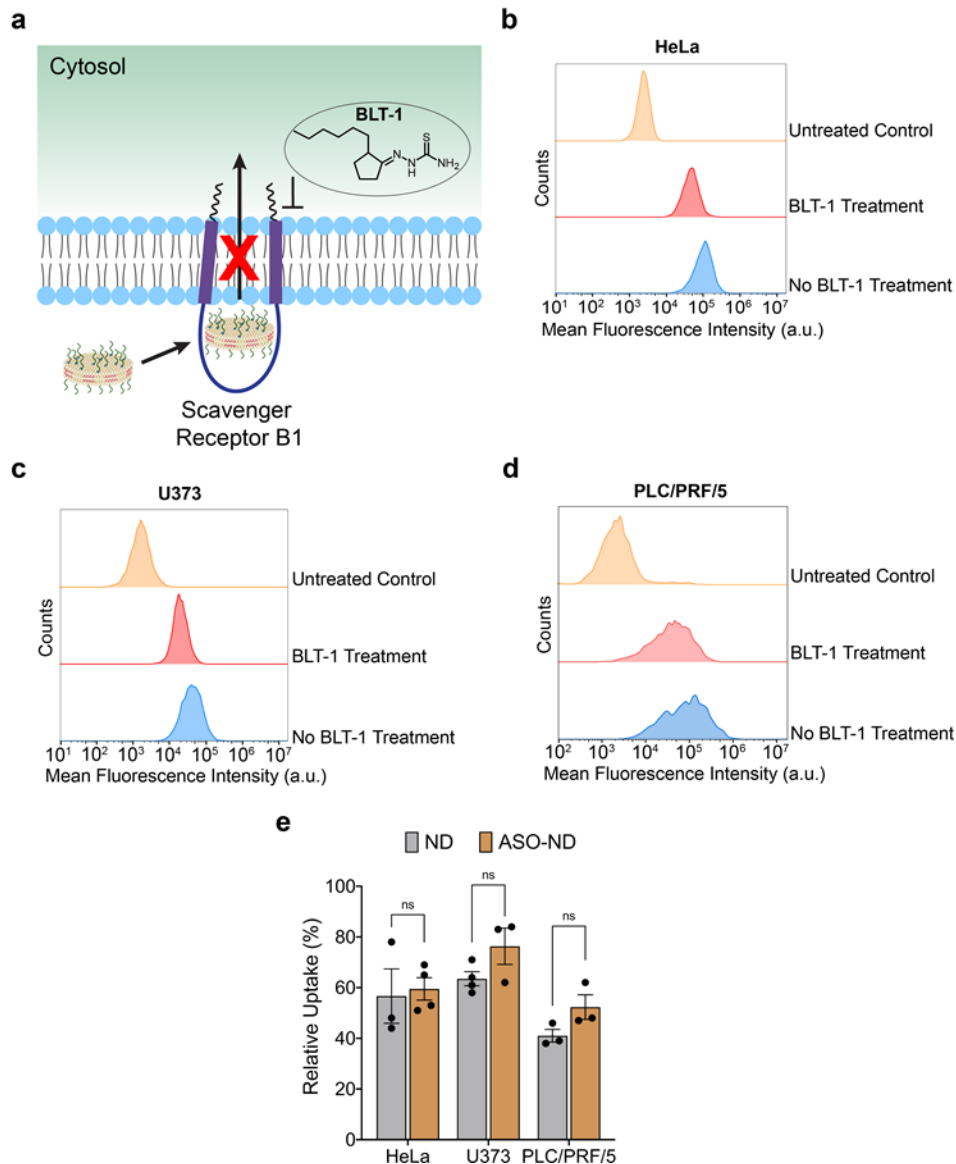


Figure 2.3.5: SRB1 partially mediates uptake of ASO-NDs in HeLa, U373, and PLC/PRF/5 cells. **(a)** Schematic showing the blocking of SRB1 on the cell surface with BLT-1 and how it can hinder the internalization of ASO-ND. Representative flow cytometry histograms measuring Cy5 intensity for cells that were pretreated with 50 μ M BLT-1 for 1 h, and then incubated with the ASO-ND for 2 h in **(b)** HeLa, **(c)** U373, and **(d)** PLC/PRF/5 cells. The flow data reports mean intensities from a minimum of 5000 cells. **(e)** Graph comparing the uptake of ASO-ND or ND into cells after BLT-1 treatment. The values are normalized to the uptake level measured for the untreated control group. Representative flow cytometry histograms and plots of the ND only treated cells are shown in **Figure S8** and **Figure S9**. Each data point represents the mean fluorescence intensity from an independent replicate. Error bars represent SEM of at least $n = 3$ replicates. There were no significant differences observed in the uptake after BLT-1 treatment for the ASO and ASO-ND groups.

This is likely due to the PS modifications, which mediate internalization through endocytosis by adsorption onto various cellular surface proteins, including SRB and LDL-receptor entry pathways.² Hence, the presence of PS modifications may further facilitate the trafficking of ASO-ND inside the cell, especially when conjugated to a delivery vehicle. We also noted the uptake of ND and ASO-ND into PLC/PRF/5 liver cells was lower following BLT-1 treatment compared to the uptake in HeLa and U373 cells. This is not surprising as hepatocytes are prominent expressors of SRB1 due to the inherent role of HDL docking and offloading of cholesterol for processing and clearance, and therefore these cells are more sensitive to SRB1 blocking.¹²³ Together, we conclude that the trafficking of thiol-NDs into cells is partially mediated by SRB1, a known pathway that circumvents endosomal entrapment by selectively taking up and delivering the ND content inside to the cytoplasm of the cells.

2.3.6: Anti-HIF-1- α ASO-ND conjugates are active in vitro

The transcription factor HIF-1- α is sensitive to hypoxia and aids in regulation of responses such as vascularization and angiogenesis that can ultimately tune oxygenation in tissues.¹²⁴ HIF-1- α also drives survival and adaptation to hypoxic or inflammatory conditions such as that found in solid tumors¹²⁵ and in wound healing.¹²⁶ Accordingly, there is significant interest in developing drugs that can downregulate the expression of HIF-1- α . Examples of HIF-1- α inhibitors include PX-478 and bortezomib, which are FDA-approved anti-cancer therapies. These inhibitors lack cell or tissue-specificity and carry significant off-target effects,^{127, 128} thus prompting the development of nucleic acid-based drugs that target HIF-1- α at the transcript level. EZN-2968 is a potent HIF-1- α gapmer ASO that has undergone Phase I trial in patients with solid tumors and showed significant reduction of HIF-1- α levels in tumor biopsies.^{109, 110} Given the proven activity of this ASO, we aimed to evaluate the potency of anti-HIF-1- α ASOs upon conjugation to the ND phospholipids and to test whether function is maintained or potentially enhanced compared to the unmodified nucleic acid drug (**Figure 2.3.6a**).

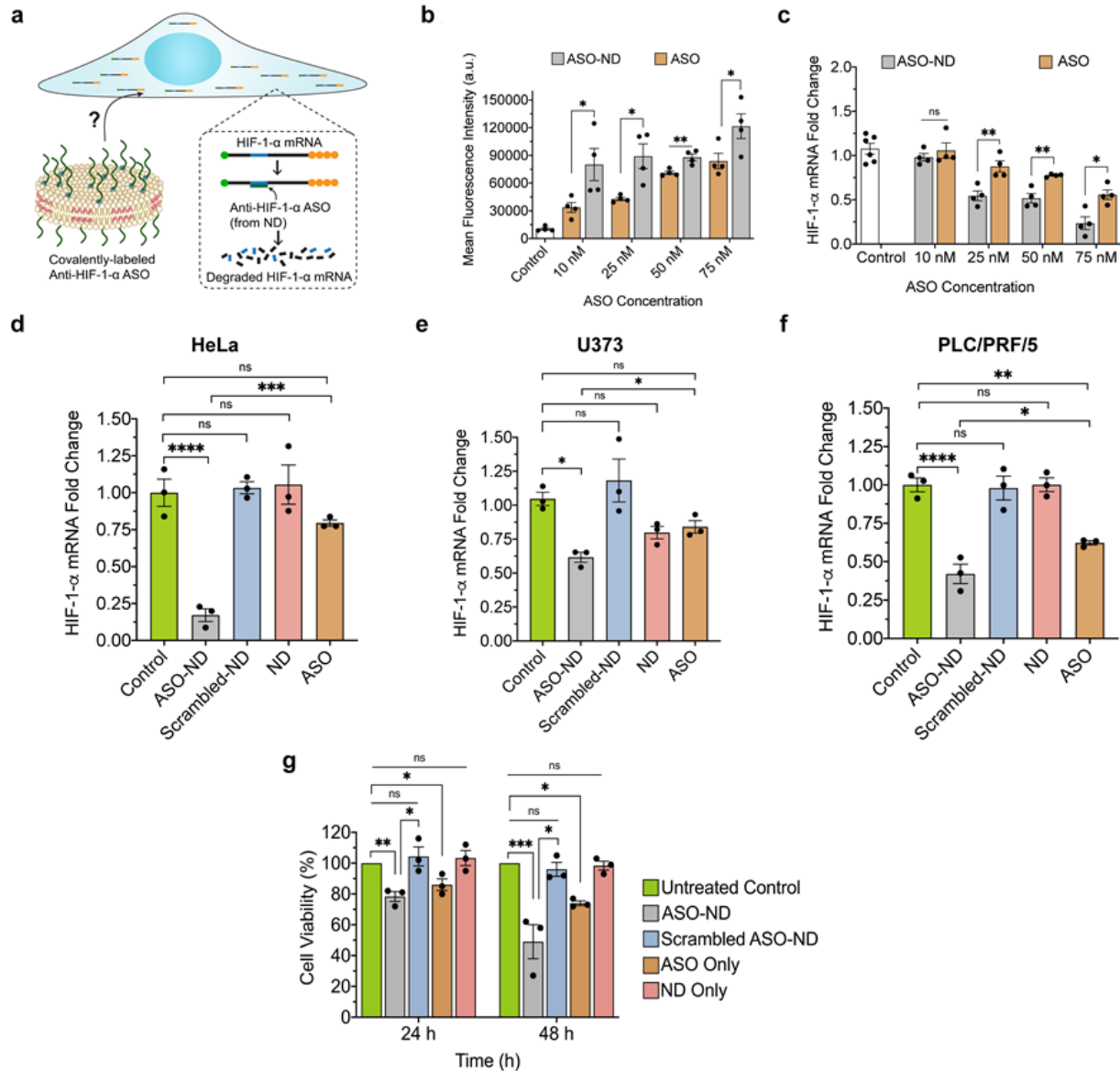


Figure 2.3.6: Quantifying the functional activity of ASO-NDs and ASOs that target HIF-1- α in three model cell lines. **(a)** Schematic showing the HIF-1- α transcript where the poly-A tail was denoted with orange circles, the blue represents that target region, and the 5' capping was shown as a green circle. **(b)** Plot quantifying the uptake of ASO-ND (gray) and ASO (gold) in HeLa cells treated for 24 h as a function of ASO concentration. The ASO was tagged with a TYE dye and the mean fluorescence intensity per cell was determined using flow cytometry. Each data point represents one independent replicate. Error bars represent SEM of $n = 3$. **(c)** Plot comparing HIF-1- α levels in HeLa cells treated for 24 h with ASO and ASO-ND. Quantification was performed using RT-qPCR. Error bars represent SEM of $n = 4$ and all values were normalized to untreated control cells. **(d)-(f)** Plots of HIF-1- α levels determined by using RT-qPCR for HeLa, U373, and PLC/PRF/5 cells that were treated with 75 nM concentrations of ASO-ND, scrambled-ND, ND, and ASO for 24 h. The ASO concentration was matched at 75 nM in all groups; however, the ND group used a 7 nM concentration of ND. The transcript levels are normalized to the untreated control group. Error bars represent the SEM of $n = 3$. **(g)** Cell viability assessment in HeLa cells after dosing the HeLa cells with ASO-ND conjugates, ASO Only, Scrambled-ND, and ND only. Cell viability was assessed using MTT assay. HeLa cells were subjected to 75 nM ASO and the ND group was subjected to 7 nM ND to best match ND concentration from the ASO-ND groups. The cells were incubated with sample for either 24 h or 48 h before adding MTT reagent and performing the assay. The values are normalized to the OD measured at 590 nm for the untreated cells as a control. Each data point represents the percent viability for one independent replicate and * $p < 0.05$, ** $p < 0.01$, *** $p < 0.001$, **** $p < 0.0001$.

First, we focused on HeLa cells and treated these cells for 24 h using different concentrations of ASO-ND and ASO. To best capture the potential activity of the ASO, no transfection agent was used in these experiments and the ASOs were spiked into the media at concentrations that ranged from 10 nM to 75 nM. We used a TYE-tagged ASO and ran flow cytometry to quantify the relative uptake levels. We generally observed dose-dependent internalization (**Figure 2.3.6b**) for both ASO and ASO-ND groups. ND-conjugation shows a significant increase in uptake compared to that of the unmodified ASO group. To test ASO function, we used identical conditions to those used for uptake measurements and then measured HIF-1- α levels using RT-qPCR (**Figure 2.3.6c**). We found a dose-dependent knockdown of HIF-1- α for both the ASO and ASO-ND group, in general agreement with the uptake data. Importantly, conjugation to the ND resulted in increased cellular internalization and increased reduction in HIF-1- α compared to the bare ASO. We normalized the knockdown levels by the uptake levels to estimate the effective activity of ASO when delivered in the unmodified and ND forms and found that the ND conjugation increased the potency of ASOs on a per molecule basis (**Figure S2.6.10**). In addition to enhanced nuclease resistance, another potential explanation for why ND conjugation leads to enhanced uptake and knockdown pertains to the internalization pathways for each type of ASO. For example, PS-modified ASOs can be routed to nonproductive pathways depending on the surface protein that internalizes the naked PS modified ASOs, resulting in dampened activity upon internalization.^{121, 129} In contrast, ND conjugation may lead to more productive pathways of uptake, such as HSPG and SRB1 mediated internalization, that allow the ASO to access the cytoplasm and the target mRNA.

To further validate this conclusion, we next treated the three cell lines: HeLa (**Figure 2.3.6d**), U373 (**Figure 2.3.6e**), and PLC/PRF/5 (**Figure 2.3.6f**) with ASO, ASO-ND, scrambled-ND, and ND for 24 h and measured HIF-1- α levels using RT-qPCR. These three cancer cell lines were selected because of their high intrinsic expression of HIF-1- α and their diverse source

tissues. We maintained the ASO concentration in all groups to 75 nM with the exception of the ND group which lacked ASO and hence we used 7.5 nM of the ND, thus best approximating the concentration of ND in the ASO-ND group. The ND group was included because of prior literature showing that certain ApoA1 mimetic peptides can downregulate HIF-1- α protein levels *in vitro* and *in vivo*,¹³⁰ but we did not detect modulation of HIF-1- α driven by the lipid nanoparticle platform. However, we found that the regulation of HIF-1- α was specific to the ASO as we observed no knockdown with the scrambled sequence. The ASO-ND group showed greater levels of HIF-1- α knockdown when compared to the ASO only group across the three cell lines tested. We were surprised to find that SRB1 expression was poorly correlated with ASO-ND activity, as SRB1 expression followed this trend PLC/PRF/5>U373>HeLa (**Figure S2.6.7**) while ASO-ND knockdown efficiency followed this trend HeLa>PLC/PRF/5>U373. Given that the uptake of NDs (**Figure S2.6.6**) and knockdown efficiency of the unconjugated ASO's was similar in all three cell lines (~25%) (**Figure 2.6.6d-f**), this suggests that other mechanisms of enhanced uptake specifically for the ASO-ND conjugates in HeLa cells. Regardless of the differential levels of enhanced knockdown across the cell lines tested, delivery of ASOs using NDs is found to be highly advantageous for modulating gene expression levels *in vitro*.

HIF-1- α is important for cancer cell survival and proliferation and its knockdown can reduce cell survival.¹³¹ Therefore, we further confirmed the functional activity of the ASO by measuring cell viability (**Figure 2.6.6g**). In this experiment, HeLa cells were treated for 24 and 48 h and then cell viability was measured using the MTT assay. We included 5 groups: ASO-ND, Scrambled ASO-ND, ND only, and ASO only. Across three independent experiments and at the 24 and 48 h time points, we observed the most significant decrease in cell viability for cells treated with the ASO-ND compared to untreated cells or to cells treated with scrambled ASO-ND. Interestingly, the soluble ASO also showed a decrease in cell viability at 24 and 48 h. These results are consistent with the HIF-1- α knockdown levels (**Figure 2.6.6d**) which showed that the

ASO-ND was more active compared to the soluble ASO. In summary, we are able to achieve efficient delivery and functional activity of the ND-tethered HIF-1- α ASO at a greater level than that of the soluble ASO. Thus, this conjugation strategy may enable improved ASO delivery and enhanced therapeutic activity.

2.4: Conclusion

We developed a facile and efficient approach to generating nucleic acid-ND conjugates. NDs self-assemble from SUVs comprised of 90% DMPC and 10% thiolated phospholipids after adding a 22 amino acid ApoA1 mimetic peptide. DNA is covalently conjugated to the surface of the ND using thiol-maleimide coupling. TEM was used to determine the maximum thiolated phospholipid content that can be tolerated and thus helping achieve NDs with up to 15 DNA copies per ND. Using this procedure, we showed that deoxyribozyme-ND conjugates were functional and are partially protected from DNase activity when compared to soluble oligonucleotides. ASO-ND conjugates are internalized by cells and show time and concentration-dependent uptake. Dual tagged ASO-ND conjugates display reduced colocalization as a function of time in cells and hence confirm separation of the ASO and phospholipid components over time. Using a small molecular inhibitor, we found that uptake is partially mediated by SRB1. ASO-ND conjugates selective for HIF-1- α showed greater activity than that of the soluble ASO drug, without the use of transfection agents, and across a panel of three cell lines. The enhanced activity is likely to be due to nuclease resistance, enhanced uptake, improved bypass of endosomal entrapment and potentially due to multivalency which may boost affinity to its target.¹³² Importantly, ND can be engineered to deliver multiple cargos including miRNAs and siRNA as well as lipophilic molecules and peptides and hence this platform may have broader applications as a therapeutic. Future work with ASO-NDs include expanded testing in other cell types, such as primary cells which may have different propensities for ND and ASO-ND uptake. More broadly, the *in vivo* activity of ASO-ND conjugates

has also yet to be explored as it remains unclear how these conjugates will distribute across different tissues and perform ASO function in animal models. That said, there is a physiological parallel for regulating HIF-1- α levels using oligonucleotide-linked HDL particles as it was recently found that hypercholesterolemia leads to elevated expression of micro-RNA 126 loaded HDL particles which directly downregulate HIF-1- α levels in pig models.¹³³ In summary, this work describes the synthesis and characterization of an ASO-ND conjugate, and we look forward to developing this platform as potential drug delivery system for cancer therapy.

2.5: Materials and Methods

All lipids were purchased (**Table S2.6.1**) from Avanti Polar Lipids (Alabaster, AL, USA). Oligonucleotides and primers for RT-qPCR were custom-synthesized (**Table S2.6.2**) by Integrated DNA Technologies (Coralville, IA, USA). The ApoA1 Mimetic Peptide (**Table S2.6.3**) was purchased from Genscript® (Piscataway, NJ, USA) with standard TFA removal. TEM samples were prepared on carbon-coated copper grids (400 mesh) obtained from Electron Microscopy Sciences (CF400-Cu; Hatfield, PA, USA) and were stained using Nano-W™ from Nanoprobes (Yaphank, NY, USA). SMCC (22360), a commercially available DNase I Kit (EN0521), 6X Loading dye (R0611), and Bond-Breaker™ TCEP Solution (77720) were obtained from ThermoFisher Scientific (Waltham, MA, USA). Hanks' Buffered Salt Solution (HBSS, H8264) and SMCC coupling performed with anhydrous *N,N*-dimethylformamide (DMF, 227056) and *N,N*-diisopropylethylamine (DIPEA, 496219) were purchased from Sigma-Aldrich (St. Louis, MO, USA). All DNA stock solutions and buffers were prepared using Barnstead™ Nanopure Water System from ThermoFisher Scientific (Waltham, MA, USA) at a resistivity of 18.2 M Ω . Unreacted SMCC was separated from DNA using ethanol precipitation with Koptec USP-grade 200-proof ethanol from Decon Labs (V1001; King of Prussia, PA, USA) and sodium acetate (3 M, pH 5.2, molecular biology grade) from Millipore-Sigma (567422; Burlington, MA, USA) and purified using

a hydrated P-2 gel from Bio-Rad (1504118; Hercules, CA, USA) or using a NAP-5 Sephadex G-25 column from Cytiva (17085301; Marlborough, MA, USA). DNA separation was performed using a MWCO: 50 kDa Amicon® Filter (UFC505024), and Blocker of Lipid Transport-1 (SML0059), and Omnipur® Agarose (2120-OP) were all purchased from EMD Millipore (Burlington, MA, USA). Quant-iT™ OliGreen™ ssDNA Reagent (O7582), DAPI stain: NucBlue™ Fixed Cell ReadyProbes™ (R37606), and SYBR™ Gold Nucleic Acid Gel Stain (S11494) were acquired from Invitrogen™ (Carlsbad, CA, USA). Cells were cultured in Dulbecco's Modification of Eagle's Medium with L-Glutamine (DMEM, 10-013-CM) using Fetal Bovine Serum (FBS, 35-010-CV) and Penicillin-Streptomycin (30-002-CI) and were detached using Trypsin EDTA (25-053-CI) from Corning (Tewksbury, MA, USA) and Non-Essential Amino Acids (NEAA, 111450; Gibco; Waltham, MA, USA) when appropriate. qPCR was performed with the following: RNeasy Mini Kit from Qiagen (74106; Hilden, NRW, Germany), High-Capacity cDNA Reverse Transcription Kit from Applied Biosystems (4368814; Foster City, CA, USA), and PerfeCTa® SYBR® Green FastMix® Reaction Mix from QuantaBio (101414-278 [VWR]; Beverly, MA, USA). MTT Cell Proliferation Kit was purchased from Abcam (ab211091; Cambridge, UK).

2.5.1: Synthesis and Characterization of Thiol ND

DMPC and the thiol lipid stocks were combined with chloroform (90:10, 80:20, and 95:5 molar ratios) and placed on a rotary evaporator to dry for 1 h. Cy5-PE was doped in at a molar ratio of 0.15% when necessary for certain experiments. After 1 h the lipid mixture was placed under a steady stream of nitrogen for 10 min. prior to hydrating the lipid film with phosphate buffered saline (PBS, pH 7.4). The mixture was sonicated for 10 min. before subjecting it to three freeze-thaw cycles. SUVs were subsequently prepared by passing the mixture 10 times through a 10 mL LIPEX® thermobarrel extruder (Evonik Industries, Essen, Germany) using a 80 nm polycarbonate filter. The ApoA1 mimetic peptide (2 mg) was dissolved in nanopure water and added to the SUVs prior to vortexing the mixture for 30 seconds. The mixture was subjected to

three warm-cool cycles alternating between 55 °C and 4 °C for 15 min. each as reported in literature.¹⁰⁷ The thiol-NDs were stored at 4 °C for up to three weeks.

2.5.2: DLS and TEM Characterization of Thiol NDs

Prepared NDs were characterized using DLS on a NanoPlus DLS Nano Particle Size and Zeta Potential Analyzer (Micromeritics Instrument Corporation, Norcross, GA, USA) instrument. Sample grids for TEM were prepared by plasmon etching a 400-mesh copper grid for 1 minute. A small drop (5 µL) of sample was placed on the grid for 30 seconds before gently wiping with filter paper so only a small amount of dispersion is left and allowed to dry. One drop of Nano-W™ was applied to the dried grid for 2 min. and was wiped and blotted using the same drying procedure. ND samples were visualized using transmission electron microscopy (TEM) on a Hitachi HT7700 instrument (Chiyoda City, Tokyo, Japan) operating at 80 kV accelerating voltage. TEM images were analyzed using the widely available ImageJ software package.

2.5.3: Addition of Maleimide Group to DNA

SMCC (2 mg) was dissolved in DMF and combined with DIPEA (0.2-fold total volume) and amine-modified DNAzyme (20 nmol) for 1 h at room temperature. Unreacted SMCC was removed through ethanol precipitation. Briefly, cold 200-proof ethanol (800 ml), water (200 ml), and sodium acetate (50 ml of 3 M solution pH 5.2) was added to the sample and frozen at -80 °C to precipitate the DNA. The precipitated solution was centrifuged at maximum speed for 30 min at 4 °C using an Eppendorf 5424R (Hamburg, Germany) refrigerated centrifuge. The supernatant was removed, and the pellet was washed twice using copious amounts of 70% ethanol (centrifuging at 4 °C for 10 min. at maximum speed in between). The pellet was dried at 37 °C for 15 min and vacuum dried using an Eppendorf Vacufuge Plus (Hamburg, Germany) for an additional 15 min. Any remaining SMCC, salts, and organic solvent was removed using a P2 gel prior to purifying the product using an AdvanceBio Oligonucleotide (Santa Clara, CA, USA) column and reverse

phase HPLC. DNA strands containing both PS and LNA modifications were purified using a NAP-5 desalting column. The column was washed multiple times with PBS (pH 7.4) prior to adding and collecting the sample (monitored through 260 nm absorbance). Samples were lyophilized overnight before use.

2.5.4: Covalent Linkage of DNA to NDs

Disulfide bonds were reduced in Cy5 containing thiol NDs using 10-fold excess TCEP. TCEP was removed using a centrifugal filtration (MWCO: 50 kDa) and the ND concentration was determined using 650 nm (A_{650}) absorbance to determine Cy5 lipid concentration (Beer's Law, $\epsilon = 250,000 \text{ M}^{-1}\text{cm}^{-1}$, pathlength = 0.1 cm), which was used to determine total lipid concentration. Dividing the concentration of lipids (2) by the number of lipids in our ND (1) can give us total concentration (3). Purified Maleimide-DNA was dissolved in PBS (pH 8.5) and combined in 6-fold excess with the reduced thiol NDs. The mixture was agitated gently at 45 °C for 2 h before removing unbound DNA using centrifugal filtration (MWCO: 50 kDa) at 8500 RPM for 10 minutes and washed four times (or until the supernatant displayed no 260 nm absorbance). Fresh PBS (pH 7.4) was added in between each wash. The number of lipids in a ND was determined as previously reported. The diameter (TEM) can give us the radius (r) and enable us to determine the area (nm^2) and divide it by the area occupied by one DMPC phospholipid (ρ), reported as 0.63 nm^2 (1).

$$\# \text{ of lipids in ND} = \frac{\pi r^2}{\rho} \times 2 \text{ leaflets} \quad (1)$$

$$\text{Total [lipid]} = \left(\frac{A_{650}}{\epsilon \times 0.1 \text{ cm}} \right) \times \left(\frac{100\%}{0.15\%} \right) \quad (2)$$

$$\text{ND concentration} = \frac{\text{Total ND lipid concentration}}{\# \text{ of lipids in single ND}} \quad (3)$$

2.5.5: FRET Analysis of ASO-ND Samples

Samples containing 100 nM of fluorescently labeled ASO conjugated to the ND, ASO simply mixed with the ND, and ASO only were prepared in PBS. The fluorometer from Horiba Scientific (Edison, NJ, USA) was blanked using a sample containing PBS or a PBS mixed with ND. The blank subtracted samples were excited at 520 nm and emission spectrum were collected with 20 accumulations, 0.1 integration, and 1-pixel increment. FRET efficiency was calculated (4) by measuring fluorescence emission at 563 nm in the presence of the acceptor and subtracting the value from ASO donor intensity:

$$\text{FRET Efficiency} = \frac{(\text{ASO Donor Intensity}_{563} - \text{Donor Intensity}_{563} \text{ in presence of acceptor})}{\text{ASO Donor Intensity}_{563}} \times 100\% \quad (4)$$

2.5.6: Quantification of DNA Density

Commercial OliGreen™ was used to quantify the DNA density on the ND. Stock concentration of DNA (11 µg/mL) composed of the same sequence strand used to functionalize NDs, was prepared at the following concentrations: 0.01, 0.1, 0.2, 0.5, 0.75, 1 µg/mL in 1X TE buffer, ND, and trypsin, to facilitate structure disassembly, were added to the calibration curve. DNA-ND samples were prepared at various concentrations of 0.2 nM, 0.4 nM, 0.6 nM, and 1.2 nM in 1X TE buffer and trypsin. Assay and calibration curve samples were heated to 85 °C for 10 min. and OliGreen reagent™ was added and mixed thoroughly before measuring the fluorescence intensity (Ex/Em = 485/528 nm) on a Synergy H1 Biotek Plate Reader (Winooski, VT, USA). DNA density values were confirmed by mathematically determining the DNA density by taking the total concentration of DNA on the DNA-ND measured by 260 nm absorbance and dividing it by the ND concentration (3).

2.5.7: Zeta (ζ) Potential Measurement of DNA-ND Samples

DNA-NDs and NDs were loaded into the zeta cells and ζ -potential was measured on the Nano Particle Size and Zeta Potential Analyzer (Micromeritics Instrument Corporation, Norcross, GA, USA) at room temperature.

2.5.8: Gel Electrophoresis

A 1.5% agarose gel was prepared using in-gel staining with SYBR Gold (10,000-fold dilution). Samples (5 μ L) containing DNA only, fluorescently labeled ND only, and fluorescently labeled DNA-ND were mixed with 6X loading dye (5 μ L) and samples were loaded onto the gel. The gel was run at 85 V for 1.5 h on a Bio-Rad PowerPac Basic Electrophoresis Supply (Hercules, CA, USA) and visualized using an Amersham Typhoon laser scanner (Cytiva, Marlborough, MA, USA).

2.5.9: DNAzyme Kinetics and Nuclease Degradation Assay

The DNAzyme-ND was diluted to 10 nM (DNA concentration) in HEPES buffer (10 mM HEPES, 150 mM NaCl, pH 7.4) and the solution was directly transferred to a 96-well plate (100 μ L). The DNAzyme substrate was prepared at 100 nM using HEPES buffer supplemented with magnesium (10 mM HEPES, 150 mM NaCl, 2 mM MgCl₂, pH 7.4) and added to the well-plate containing the DNAzyme samples (total volume = 200 μ L). The FAM fluorescence intensity was immediately monitored for 4 h with the plate reader. The DNA-ND samples and soluble (free) DNAzyme (1 μ M) were incubated with 1 U of DNase I of the supplied reaction buffer (final concentrations: 10 mM Tris-HCl, 2.5 mM MgCl₂ and 0.1 mM CaCl₂) at 37 °C for 2 h. Thereafter, the DNase I was quenched using the supplied EDTA (5 mM) and inactivated at 65 °C for 10 mins, as per the accompanied protocol. The samples were transferred to a 96 well plate and combined with the DNAzyme substrate solution (10 mM HEPES, 150 mM NaCl, 10 μ M DNAzyme substrate,

4 mM MgCl₂, pH = 7.4) and FAM fluorescence intensity was immediately monitored for 2.5 h using the plate reader.

2.5.10: Cell Culture

HeLa cells (ATCC), U373 cells (Sigma-Aldrich), and PLC/PRF/5 (ATCC) cells were cultured in DMEM with 10% FBS and Penicillin (100 U/mL) and Streptomycin (100 mg/mL). NEAA (1%, 100X) was supplemented to the media of U373 cells and PLC/PRF/5. Cells were maintained at 37 °C under a humidified CO₂ atmosphere (5%).

2.5.11: Confocal Microscopy of HeLa Cells

HeLa cells were plated at a density of 1×10^4 cells/well in a Nunc 96 well black optical plate (265300, ThermoFisher, Waltham, MA, USA) the day before experiment. Fluorescently labeled ASO-ND (100 nM) were incubated with cells for 3 h, 12 h, or 24 h prior to fixing cells with 4% paraformaldehyde. Cells were washed three times using PBS (pH 7.4) and stained using DAPI. Cells were imaged on a Nikon Ti2 Eclipse confocal microscope (Minato City, Tokyo, Japan) with a 60X oil objective, Nikon Elements, perfect focus, and a C2 laser scanning system. Z-stacks were collected with a 0.15 μ m step size. Cell images were analyzed using ImageJ and Pearson's Coefficient using the Just Another Colocalization ImageJ plugin.

2.5.12: Dose- and Time-Dependent Uptake Measurements using Flow Cytometry

HeLa, U373, and PLC/PRF/5 cells were plated at a density of 8×10^4 cells/well in tissue-culture treated 12-well plates the day before experiment. Fluorescently labeled ASO-ND (ND concentrations: 5 nM, 25 nM, 50 nM, 100 nM) for 4 h, 12 h, or 24 h before cells were washed with sterile PBS (pH 7.4) once before adding trypsin and collecting cells for flow. Trypsinized cells were washed with HBSS twice, prior to resuspending the cells in fresh HBSS for flow cytometry assessment on a Beckman Coulter Cytoflex (Pasadena, CA, USA) to measure cell associated

Cy5 fluorescence intensity. Histograms were prepared using FlowJo software (FlowJo LLC, Ashland, OR, USA).

2.5.13: SRB1 Mediated Uptake of ASO-NDs

HeLa, U373, and PLC/PRF/5 cells were plated at a density of 8×10^4 cells/well in tissue-culture treated 12-well plates the day before experiment. Cells were treated with BLT-1 (50 μ M) in serum-free DMEM for 1 h. Anti-HIF-1- α ASO-ND (15 nM) was added and incubated with cells for 2 h, prior to washing cells and collecting and analyzing cells for flow in the same procedure as described above. Fluorescence intensity was compared against untreated cells containing ND or ASO-ND.

2.5.14: RT-qPCR to Assess HIF-1- α Levels after EZN-2968 ASO-ND Treatment *in vitro*

HeLa, U373, and PLC/PRF/5 cells were plated at a density of 5×10^4 cells/well in tissue-culture treated 24-well plates the day before experiment. Anti-HIF-1- α ASO-ND, soluble anti-HIF-1- α , Scrambled-ND, and NDs were incubated with cells for 24 h. Cells were lysed using QIAzol and total RNA was collected as per the accompanied QIAGEN extraction kit procedure. RNA was reverse transcribed as per the recommended protocol for the High-Capacity cDNA Reverse Transcription Kit using a T100 Thermal Cycler (Bio-Rad, Hercules, CA, USA). HIF-1- α mRNA levels were quantified using quantitative real time PCR (RT-qPCR) using PerfeCTa SYBR Green FastMix and 50 μ M custom primers (**Table S2.6.2**) and a Roche Lightcycler® 96 (Basel, Switzerland) instrument. Relative quantification of mRNA levels was determined using the $\Delta\Delta C_t$ method with 18S mRNA levels for an internal control.

2.5.16: Comparing Dose-Dependent Uptake of Anti-HIF-1- α ASO and Anti-HIF-1- α ASO-NDs

HeLa cells were plated at a density of 8×10^4 cells/well in tissue-culture treated 12-well plates the day before experiment. Anti-HIF-1- α ASO-NDs and soluble anti-HIF-1- α ASO were

incubated with cells for 24 h prior to washing cells and collecting and analyzing cells for flow in the same procedure as described above. Fluorescence intensity was compared of the soluble anti-HIF-1- α against the soluble anti-HIF-1- α ASO-ND.

2.5.17: MTT Assay to Assess Cell Viability

HeLa cells were plated at a density of 1×10^4 cells/well in a tissue-culture treated 96-well plates the day before experiment. The following day, the media was exchanged for fresh media and anti-HIF-1- α -ND, soluble anti-HIF-1- α , scrambled-ND, and NDs were incubated with cells for 24 or 48 h. The cells were rinsed with fresh media prior to adding 50 μ L of phenol red-free and serum-free DMEM and 50 μ L of pre-warmed (37 °C) MTT solution. The cells were placed in the incubator at 37 °C for 3 hours before adding 150 μ L of pre-warmed MTT solvent. Subsequently, the plate was covered in foil and placed on a shaker for 15 minutes before reading the optical density at 590 nm on a plate reader. Cell viability was assessed from determining the cytotoxicity and normalizing to the untreated control (at 100%).

2.6: Supplementary Information

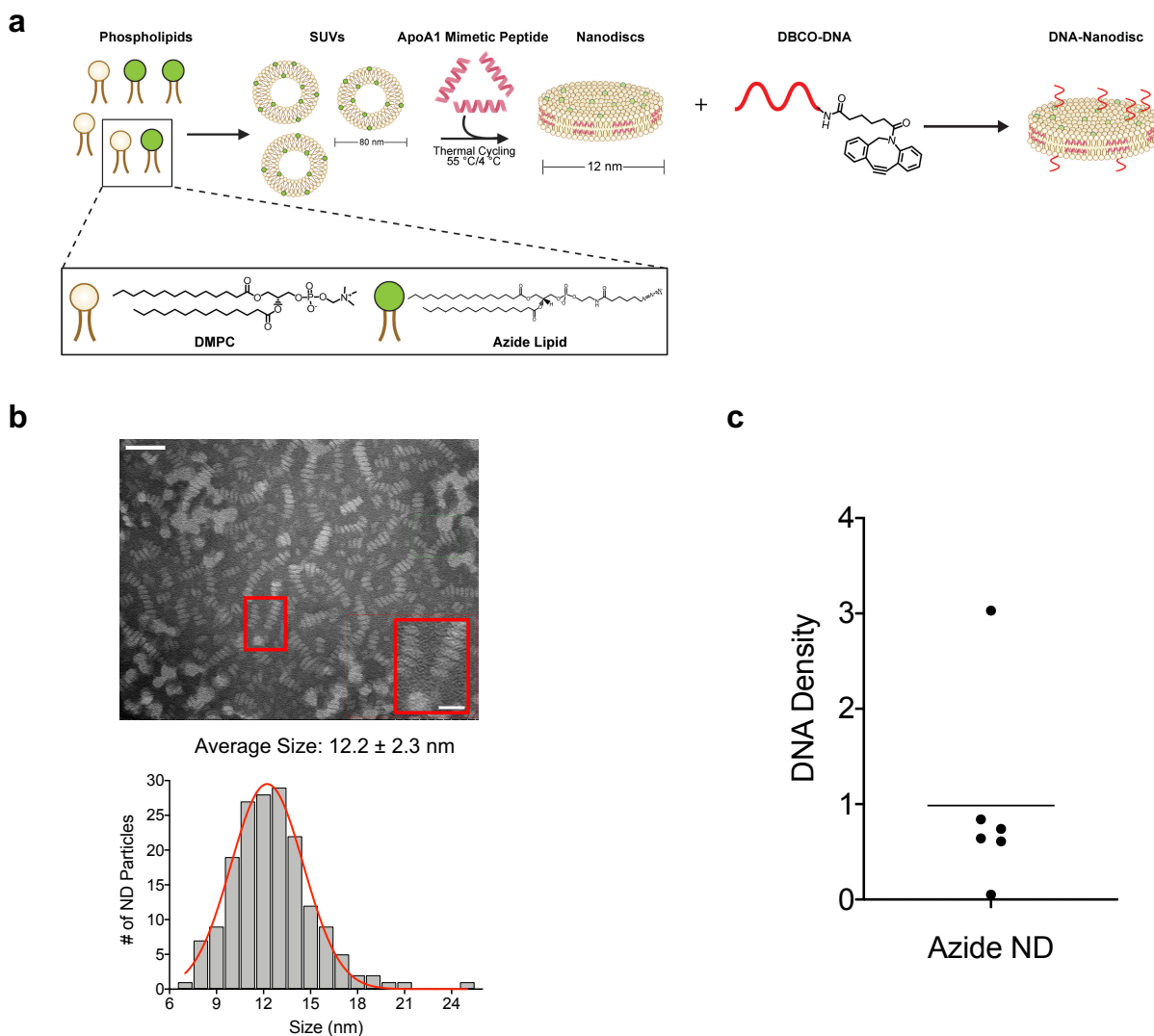


Figure S2.6.1: DNA density using the click chemistry approach to assemble NDs. **(a)** Scheme depicting that azide-NDs were prepared from SUVs comprised of 10% DPPE-Azide phospholipid (Avanti Polar Lipids) and 90% DMPC. DBCO DNA (modification obtained from Integrated DNA Technologies) was conjugated to the ND using copper-free click chemistry in KPi buffer. **(b)** TEM image (top) and binned sized analysis of nanodiscs (bottom) of $n = 170$ NDs revealing that NDs prepared with DPPE-azide yield an average size of 12.2 nm. Samples were prepared using a plasmon-etched 400-mesh copper grid and stained was performed using Nano-W™. Scale bar: 50 nm, inset: 30 nm. **(c)** Plot showing the low DNA density as measured using OliGreen™. This approach results in an average DNA density of < 1 DNA/ND suggesting this attachment chemistry was not favorable for dense DNA conjugation onto the ND surface.

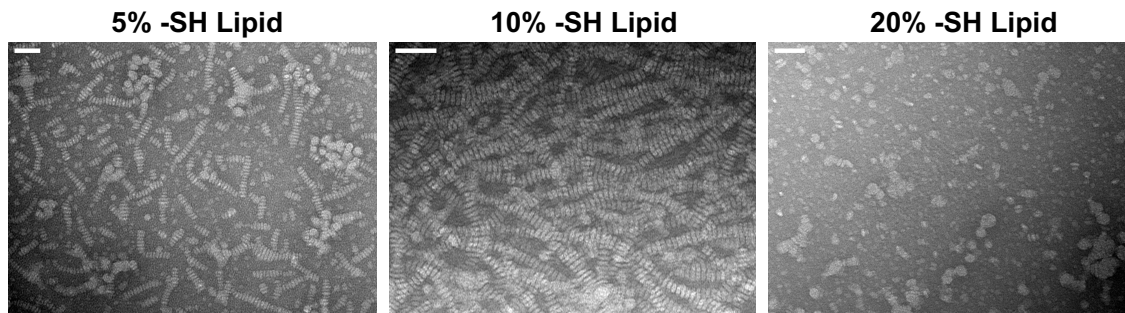


Figure S2.6.2: TEM panel of NDs incorporated with different ratios of thiol lipids. Thiol NDs incorporated with 5% and 10% thiol lipids formed monodisperse homogeneous populations, whereas the 20% thiol lipids were heterogeneous and aggregated, suggesting that a doping ratio of 10% represents the highest tolerated concentration that still assembles as a ND. Samples were prepared using a plasmon-etched 400-mesh copper grid and stained was performed using Nano-W™. Scale bar: 50 nm.

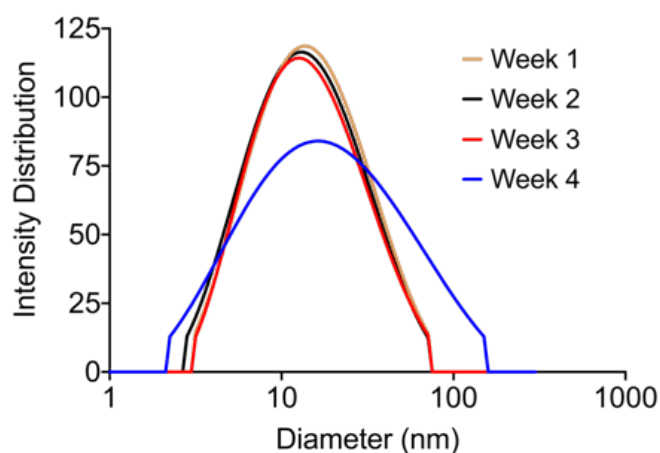


Figure S2.6.3: DLS stability data of 10% thiol DNA-NDs. DNA-NDs were stored at 4 °C and DLS measurements were taken each week. This graph suggests that DNA-NDs are stable for up to 3 weeks.

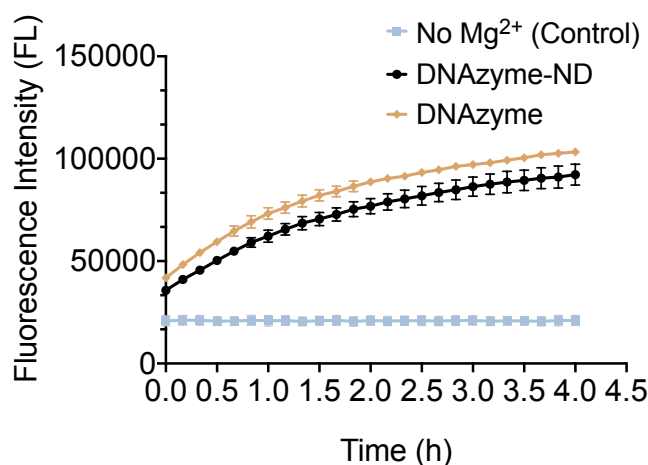


Figure S2.6.4: Catalytic activity of the DNAzyme-NDs. The mock RNA substrate used in this fluorescence kinetics assay was labeled with a FAM fluorophore on one terminus and a quencher on the opposite terminus. Graph shows a time-dependent increase in fluorescence as a result of cleavage of the mock RNA substrate by the soluble DNAzyme or the DNAzyme conjugated to the ND surface. DNAzyme incubated with the substrate in a magnesium-free buffer was added as a control. This plot shows that the DNA-ND is functional and active. Samples represent SEM of $n = 3$ independent replicates.

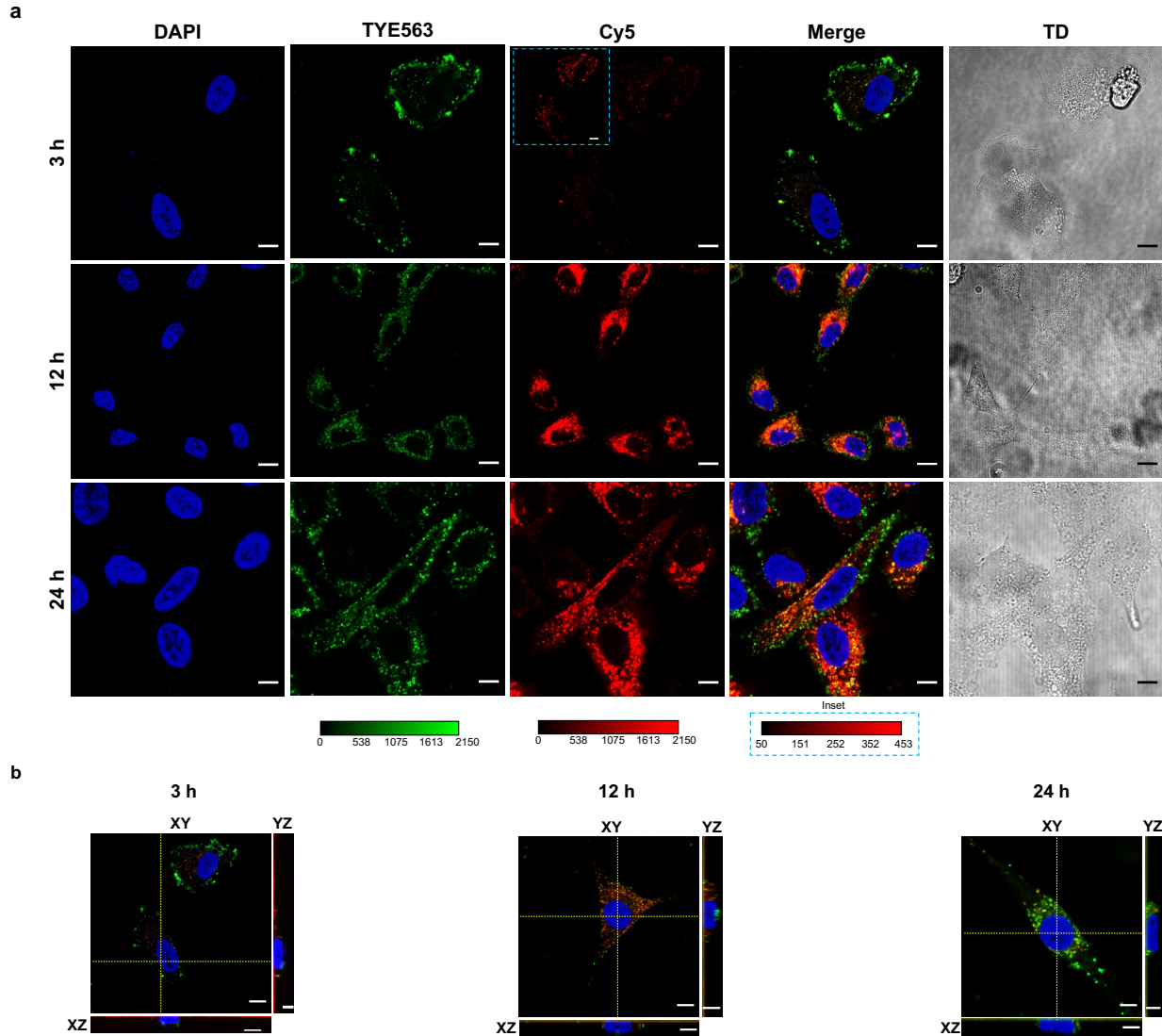


Figure S2.6.5: Confocal microscopy showing the time course for internalization of ASO-NDs into HeLa cells. **(a)** Panel shows representative images of cells treated with ASO-ND at 3 h (top), 12 h (middle), and 24 h (bottom). ASO-NDs initially localize near the cell membrane, and then at later time points there is increased localization in the cytoplasm. **(b)** Confocal Z-stack scans performed to determine the localization of ASO-ND conjugates internalized in HeLa cells at different 3 h, 12 h, and 24 h timepoints. Panel shows representative images taken at the middle layer of the cell. For each timepoint there is a planar and orthogonal projection, as derived from the indicated yellow line on XY field. We do not detect nuclear localization in these experiments. ASO was labeled with a TYE dye in the Cy3 channel and NDs were prepared using a Cy5 phospholipid. The DNA concentration was maintained at 100 nM in all groups. Cells were fixed and the nuclei were stained with DAPI (blue) prior to imaging. Scale bar: 5 μ m.

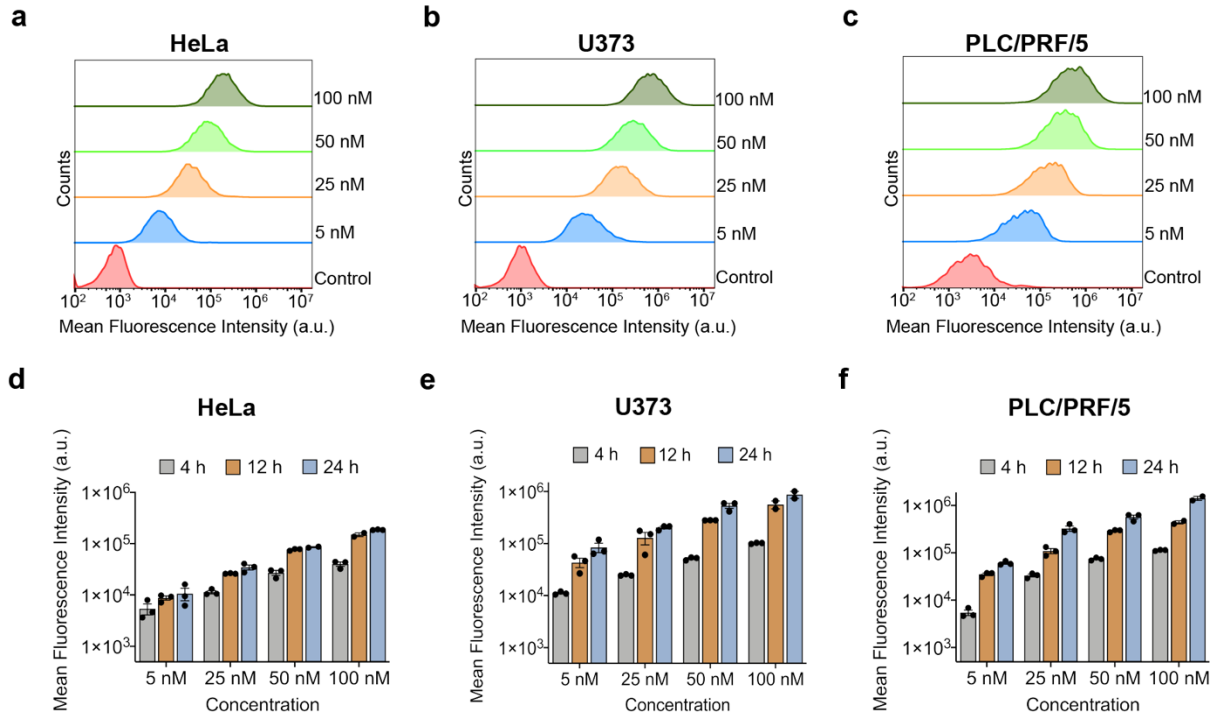


Figure S2.6.6: Quantification of ND uptake into HeLa, U373, and PLC/PRF/5 cells. Representative flow cytometry histograms of cells treated with ND tagged with 0.1% Cy5-lipids for 12 h for (a) HeLa, (b) U373, and (c) PLC/PRF/5 cells. Flow data represent Cy5 intensities for a minimum of 5000 cells. (d)-(f) show plots of the mean fluorescence intensity for cells treated with NDs as a function of time and ND concentration. There is an increase in uptake of the ND as a function of time at 4 h, 12 h, and 24 h for the three cell lines tested. HeLa cells generally showed the least ND uptake within this cohort of cells. Each data point represents one independent replicate. Error bars represent SEM of $n = 3$.

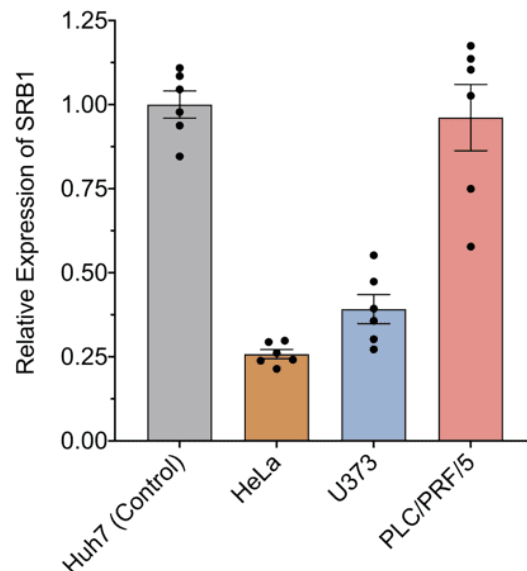


Figure S2.6.7: RT-qPCR experiment confirming the expression of SRB1 in HeLa, U373, and PLC/PRF/5 cells. We used 18S as the housekeeping gene. SRB1 expression is compared against wildtype Huh7 cells as a control because it is known to express high levels of SRB1. High SRB1 mRNA transcript levels were detected in PLC/PRF/5 cells, followed by U373 cells, followed by HeLa cells showing the lowest amount of expression. Each data point represents one independent replicate. Error bars represent SEM for $n = 6$ independent replicates.

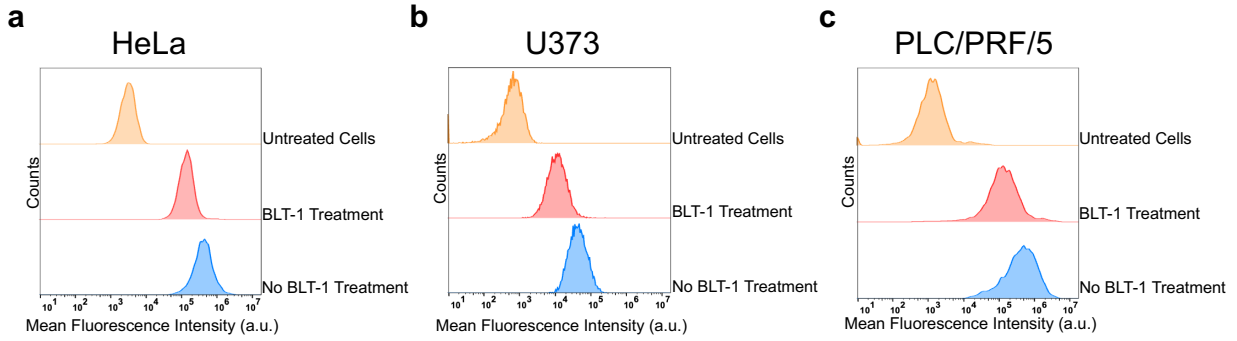


Figure S2.6.8: Testing the role of SRB1 in mediating ND uptake. Representative flow cytometry histograms measuring Cy5 intensity for cells pretreated with 50 μM BLT-1 for 1 h, and then incubated with the ND for 2 h for (a) HeLa, (b) U373, and (c) PLC/PRF/5 cells. The flow data reports mean intensities from a minimum of 5000 cells. Reduced Cy5 intensity for HeLa, U373, and PLC/PRF/5 cells after BLT-1 treatment indicates that SRB1 partially mediates the uptake of NDs into cells.

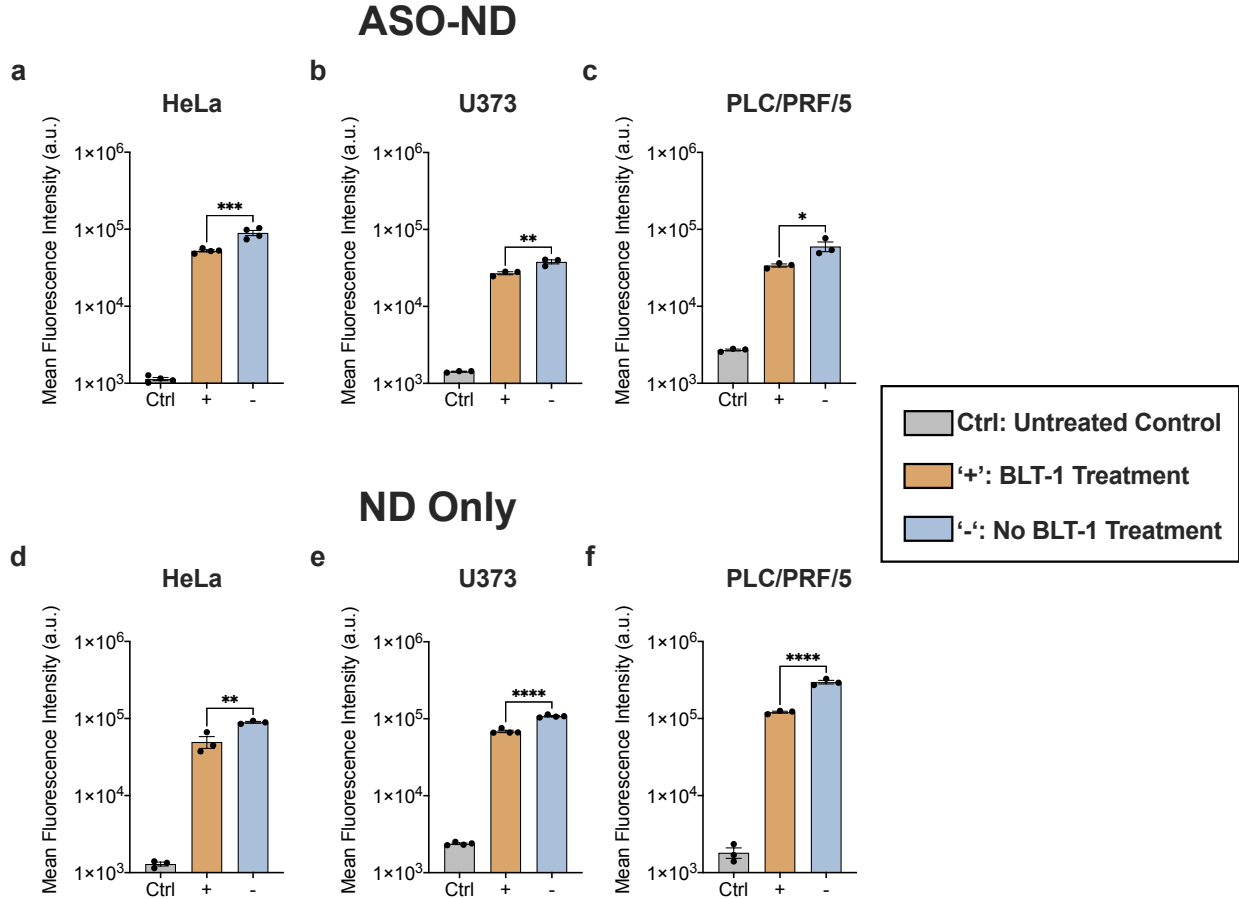


Figure S2.6.9: Quantitative Cy5 mean fluorescence intensity plots of the HeLa, U373, and PLC/PRF/5 cells treated with BLT-1. The indicated cell lines were pre-treated with 50 μM BLT-1 for 1 h prior to adding ASO-ND or ND for 2 h. The flow data reports mean intensities from 5000 cells. Bar graphs are comparing the uptake of ASO-ND (a) – (c) or ND (d) – (f) into cells after BLT-1 treatment. The raw data is a summary and representative flow cytometry histograms are shown in Figure 2.3.5 and Figure S2.6.8. Each data point represents one independent replicate. Error bars represent SEM of a minimum of $n = 3$ and * $p < 0.05$, ** $p < 0.01$, *** $p < 0.001$, **** $p < 0.0001$.

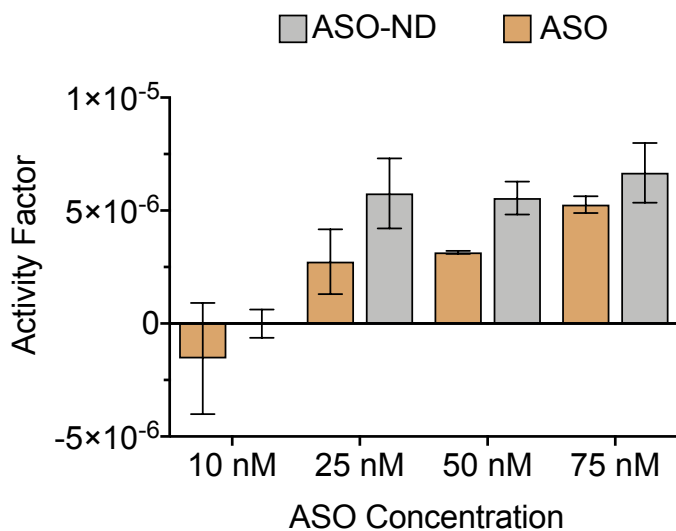


Figure S2.6.10: Plot of the activity factor comparing the activity of ASO-ND vs. naked ASOs on a per molecule basis. The ASOs and ASO-NDs were introduced to HeLa cells for 24 h without the use of a transfection reagent. Activity factor is determined by dividing the knockdown efficiency of the ASO-ND or ASO (Figure 2.3.6c) with the uptake value as determined by flow cytometry (Figure 2.3.6b). ASO-ND conjugates display enhanced activity compared to soluble HIF-1- α ASO. Error bars represent the SEM from $n = 3$ replicates.

Table S2.6.1: Lipids used for preparing thiol-modified NDs.

Lipid	Catalog Number	Structure
DMPC (1,2-dimyristoyl-sn-glycero-3-phosphocholine)	850345	
Thiol lipid (1,2-dipalmitoyl-sn-glycero-3-phosphothioethanol)	870160	
Cy5 lipid [1,2-dioleoyl-sn-glycero-3-phosphoethanolamine-N-(cyanine 5)]	810335	

Table S2.6.2: Oligonucleotide and primer sequences used for *in vitro* studies. Sequences consist of the catalytic DNAzyme, the HIF-1- α ASOs, scrambled ASO sequences, and primers used for RT-qPCR.

“+” = LNA Modification “*” = PS Modification “3AmMo” = 3' Amino Modifier. “rX” = RNA base

“5TYE563” = 5' TYE™ 563 Fluorophore

“56-FAM” = 5' 6-Fluorescein fluorophore

“3IABkFQ” = 3' Iowa Black® Hole FQ Quencher

ID	Sequence (5' → 3')
Catalytic Dz	ATT CCT TAA AGG CTA GCT ACA ACG ATT CTT GGC TTT
Catalytic Dz-Amine	ATT CCT TAA AGG CTA GCT ACA ACG ATT CTT GGC TTT /3AmMO/
Catalytic Dz Substrate	/56-FAM/ GCC AAG AArG rUTT AAG GAA T /3IABkFQ/
HIF-1- α ASO	+T*+G*+G* C*A*A* G*C*A* T*C*C* +T*+G*+T* A
HIF-1- α ASO-Amine	+T*+G*+G* C*A*A* G*C*A* T*C*C* +T*+G*+T* A /3AmMO/
TYE563-HIF-1- α ASO-Amine	/5TYE563/ T*G*G* C*A* A* G*C*A* T*C*C* T*G*T* A /3AmMO/
Scrambled HIF-1- α ASO-Amine	+C*+G*+T* C*A*G* T*A*T* G*C*G* +A*+A*+T* C /3AmMO/
SRB1 Forward Primer	TCC TCA CTT CCT CAA CGC TG
SRB1 Reverse Primer	TCC CAG TTT GTC CAA TGC C
HIF-1- α Forward Primer	TAT GAG CCA GAA GAA CTT TTA GGC
HIF-1- α Reverse Primer	CAC CTC TTT TGG CAA GCA TCC TG
18S Forward Primer	AGG AAT TGA CGG AAG GGC ACC A
18S Reverse Primer	GTG CAG CCC CGG ACA TCT AAG

Table S2.6.3: ApoA1 mimetic peptide sequence.

Peptide ID	Sequence (N → C)
ApoA1 Mimetic	PVLDLDFRELLNELLEALKQKLIK

Chapter 3

Nanodiscoidal Nucleic Acids for Gene Regulation

Contributions: Steven Narum and Kyung In Baek performed mice studies, Shuhong Liu performed sensitized-FRET experiments, and Yixiao Dong performed TEM imaging.

3.1: Overview

Therapeutic nucleic acids represent a powerful class of drug molecules to control gene expression and protein synthesis. A major challenge in this field is that soluble oligonucleotides have limited serum stability and the majority of nucleic acids that enter the cells are trapped within endosomes. Delivery efficiency can be improved by using lipid scaffolds. One such example is the nanodisc (ND), a self-assembled nanostructure comprised of phospholipids and peptides and modeled after high density lipoproteins (HDL). Herein, we describe the development of the Nanodiscoidal Nucleic Acid (NNA) which is a ND covalently modified with nucleic acids on the top and bottom lipids faces as well as the lateral peptide belt. The 13 nm ND was doped with thiolated phospholipids and thiol-containing peptides and coupled in a one-pot reaction with oligonucleotides to achieve ~30 DNA/NNA nucleic acid density. NNAs showed superior nuclease resistance and enhanced cellular uptake that was mediated through scavenger receptor B1. Time-dependent FRET analysis of internalized NNA confirmed that NNAs display increased stability. NNAs modified with clinically validated antisense oligonucleotides (ASOs) that target HIF-1- α mRNA showed enhanced activity compared to that of the soluble DNA across multiple cell lines as well as a 3D cancer spheroid model. Lastly, *in vivo* experiments show that ASO-modified NNAs are primarily localized into livers and kidneys, and NNAs were potent in downregulating HIF-1- α using five-fold lower doses than previously reported. Collectively, our results highlight the therapeutic potential for NNAs.

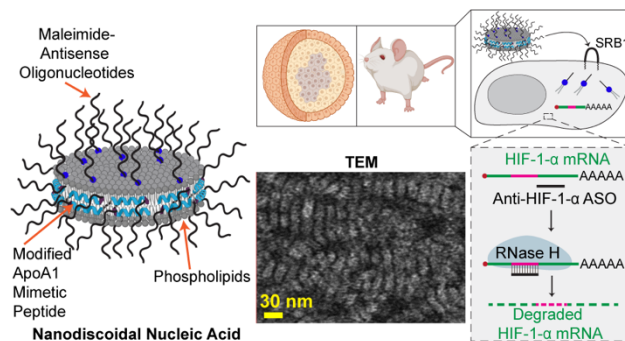


Figure 3.1.1: Overview of the structure for nanodiscoidal nucleic acids (NNAs). NNAs retained discoidal morphology and when incubated with spheroids or injected into mice, showed reduction of HIF-1- α levels.

3.2: Introduction

Nucleic acid therapeutics have made rapid advancements and strides over the past couple decades, which was only accelerated during the COVID-19 pandemic because of the role of liposome-mRNA vaccines in combatting severe disease. The numerous clinical trials using nucleic acid-based drugs include antisense oligonucleotides (ASOs), siRNA, mRNA, adenoviral vectors (AAV), and aptamers are starting to yield a steady stream of FDA-approved therapeutics. That said, there are a significant number of failures and hundreds of clinical trials thus far have only produced 15 FDA approved therapies to date. The efficacy of these drugs is often limited by several factors. First, the vast majority of nucleic acid drugs fail to reach their cytoplasmic target due to many processes that include nuclease-mediated degradation, as well as endosomal entrapment and degradation.^{1, 4} To overcome this issue, larger doses of nucleic acid drugs are used, which can lead to thrombocytopenia and off-target effects.³ Nanoparticle (NP) compositions, such as spherical nucleic acids, help mitigate the delivery and stability challenges and have been shown to improve specificity, therapeutic dosing, and overall half-life.^{102, 103} In part, NPs are an advantageous platform for delivery due to their smaller sizes (< 200 nm) which leads to enhanced cell uptake and evasion of clearance processes. Phospholipid-based NPs (e.g., liposomes) are the most widely used NP scaffold in the clinic but these tend to have limited stability and lower encapsulation efficiencies.⁷ Accordingly, lipid-based nanodiscs (NDs) have emerged as a promising class of NPs for the delivery of nucleic acids.

NDs structurally mimic nascent high-density lipoproteins (HDL) that circulate in blood and function in reverse cholesterol transport. Due to this native role, NDs are endowed with anti-inflammatory¹⁶ and anti-atherogenic properties,¹³⁴ hence offering additional benefit in using the ND scaffold. Additionally, NDs are also natively loaded with micro-RNAs (<25 nucleotide long RNAs), important in regulating HDL metabolism and other tissue-signaling processes.^{22, 72} NDs are primarily comprised of phospholipids along with apolipoprotein A1 (ApoA1), an alpha-helical

and amphipathic scaffolding protein. ApoA1 interacts with scavenger receptor B1 (SRB1) to mediate influx and efflux of cholesterol and miRNA cargo from the cytosol of the cell. This SRB1-ND transport process is described as non-endocytic²⁷ and has been shown to enhance the delivery of oligonucleotides from the ND surface to the cell because this transport mechanism bypasses endosomal entrapment and degradation.^{22, 23} SRB1 is expressed in multiple cell types, and especially in cancer cells, hence offering a broad strategy for targeted delivery of oligonucleotides.²⁸ Moreover, NDs can greatly improve circulation times and avoid immune-triggered elimination which plagues the delivery of conventional oligonucleotides. Furthermore, NDs can be rapidly self-assembled from mixtures of phospholipids and ApoA1 (<3 h), offer facile scale-up, are regarded as safe, and have demonstrated high tolerability in previous clinical trials.²⁵ Therefore, developing bioconjugation strategies for linking the maximum number of nucleic acids to each NDs is paramount may transform current approaches for nucleic acid-based drugs.

Previously, we reported a method to boost nucleic acid density on a ND scaffold by doping in thiol-containing phospholipids into the ND and conjugating these lipids to maleimide-modified oligonucleotides and forming covalent linkages.⁶² This conjugation chemistry offered significant advantages over commonly used non-covalent modifications of spherical and discoidal HDL scaffolds (including HPPS, sHDL, and NDs). Specifically, non-covalent interactions employing electrostatic binding and cholesterol-mediated binding are weak, yield low nucleic acid density (~1-10 per ND),^{69, 74, 78, 83} high polydispersity of loading, and display short half-lives (2-4 h) *in vitro* and *in vivo*,^{23, 108} thus limiting translational potential. In this work, we sought to engineer the ND scaffold to maximize loading density on the ND scaffold. The premise for this approach is the rigor of prior work with spherical nucleic acids that showed that high density DNA loading boosts the efficacy of these therapeutics through several mechanism including nuclease suppression, enhanced uptake, and increased hybridization efficiency to mRNA targets.^{135, 136}

Given that >50% of the ND is comprised of the peptide scaffold, we postulated that we could increase DNA loading by directly linking the nucleic acid to the peptide spanning the

perimeter of the ND. The challenge with this approach is that it requires introduction of a reactive group to the amphipathic peptide which may disrupt its propensity to form ND as subtle and, in some cases, single amino acid modifications have been shown to abolish its activity.⁵⁷ Therefore, we screened a small library of cysteine modified ApoA1-mimetic peptides focusing on a 22 amino acid (22A) target that had been tested in phase I clinical trials to treat atherosclerosis.⁵⁶ We decided to use reactive thiol residues because this is a native amino acid which is likely less immunogenic and given that we can introduce thiol-containing phospholipids into the ND, having thiolated peptides suggests the potential for running an efficient one-pot reaction to couple oligonucleotides to ND using facile Michael addition chemistry. In this way, we aimed to create a nanodiscoidal nucleic acid (NNA) with DNA loaded on the perimeter as well as the top and bottom lipid faces of the structure. We inserted cysteines (Cys) on the N-, C-, or both termini of the peptide and identified peptides that efficiently formed homogenous populations of NNAs. The optimal NNAs employed C-terminal GGC modified residues and presented an average of 30 copies of DNA per NNA, the highest density of nucleic acid-ND conjugates reported to date. The dense NNA structure retained its ultrasmall size (~12 nm) and discoidal morphology and demonstrated significant nuclease and serum stability. By conjugating the clinically-relevant EZN2968, an antisense oligonucleotide (ASO) that targets hypoxia inducible factor 1- α (HIF-1- α) mRNA to the ND,¹¹⁰ we demonstrated avid *in vitro* uptake along with reduction in HIF-1- α transcript levels, and a marked decrease in cell viability of cancer cells that are HIF-1- α dependent. We used this specific ASO because of the role of HIF-1- α in promoting survival of cancerous and tumorous tissue. This ASO showed activity in phase I clinical trials against refractory solid tumors, but this was not pursued further, suggesting that enhancing its efficacy may offer a route to rescuing this candidate. We further confirmed that NNA uptake is SRB1-dependent. The efficacy of anti-HIF-1- α NNAs was further validated using 3D spheroid models that showed enhanced uptake that was SRB1-mediated with a ~2-fold enhancement in transcript knockdown compared to identical

concentrations of naked ASO. Lastly, we confirmed the delivery and activity of anti-HIF-1- α NNA conjugates *in vivo* and specifically in liver and kidney tissues using a murine model. Importantly, we observed activity at low dosing (0.7 mg/kg) which afforded a 5-fold enhancement compared to conventional ASOs that dosed multiple times.¹¹⁰ Overall, this work demonstrates marked improvements in the efficacy of the HIF-1- α ASO, which has been tested in human trials and thus suggests the potential for NNAs to transform the efficacy of ASO drugs broadly.

3.3: Results and Discussion

3.3.1 Screening of Cysteine-Modified ApoA1 Mimetic Peptides

ND scaffolds were assembled by preparing small unilamellar vesicles (SUVs) through extrusion (**Figure 3.3.1a**).⁶² SUVs were comprised of phospholipids, specifically 1,2-dimyristoyl-sn-glycero-3-phosphocholine (DMPC) and/or 1,2-dimyristoyl-sn-glycero-3-phosphothioethanol (Ptd-Thioethanol) in a 90:10 (% molar) ratio (**Figure 3.3.1b**). Cy5 headgroup tagged phospholipid (**Table 3.6.2**) was added at a 0.15% - 1.0% molar ratio as needed to visualize NDs using fluorescence. We chose to work with an ApoA1 mimetic sequence, 22A, that has been clinically evaluated in a phase I safety analysis and demonstrated to be tolerable at high doses.⁵⁶ The NNA scaffolds were created by inserting one or two Cys residues at the N-and/or C- terminus of the 22A peptide (peptide A, **Figure 3.3.1c**) to generate ND with peptides B, C, and D. To conjugate nucleic acids to the top and bottom faces of the ND, we doped in 10% thiol modified phospholipids to enable nucleic acid conjugation to the phospholipids. The peptides containing one Cys insertion at the N- or C-terminus (peptides B and C) also included a double glycine spacer to minimize disruption to the native amphipathic structure of the peptide. The double-Cys insertion (peptide D) into 22A peptide did not contain a double glycine spacer as helical wheel modeling of the structure suggested that adding 6 residues would perturb the class A helix structure of the peptide.¹³⁷ The peptides were capped with an acetyl group at the N-terminus and an amide group

at the C-terminus for each of these peptides to boost lipid affinity.⁴² Following the ND formation, maleimide-modified DNA was coupled to the scaffold to create DNA-ND and NNA conjugates (**Figure 3.3.1d**) using optimized reaction conditions identified previously to bolster reaction rate and nucleophilicity.⁶² In this work, we reserve the notation NNA for NDs that present nucleic acids on all faces of the structure – both the phospholipid headgroups as well as the peptide perimeter. We refer to structure that present nucleic acids solely on phospholipids or solely on peptides as DNA-ND conjugates.

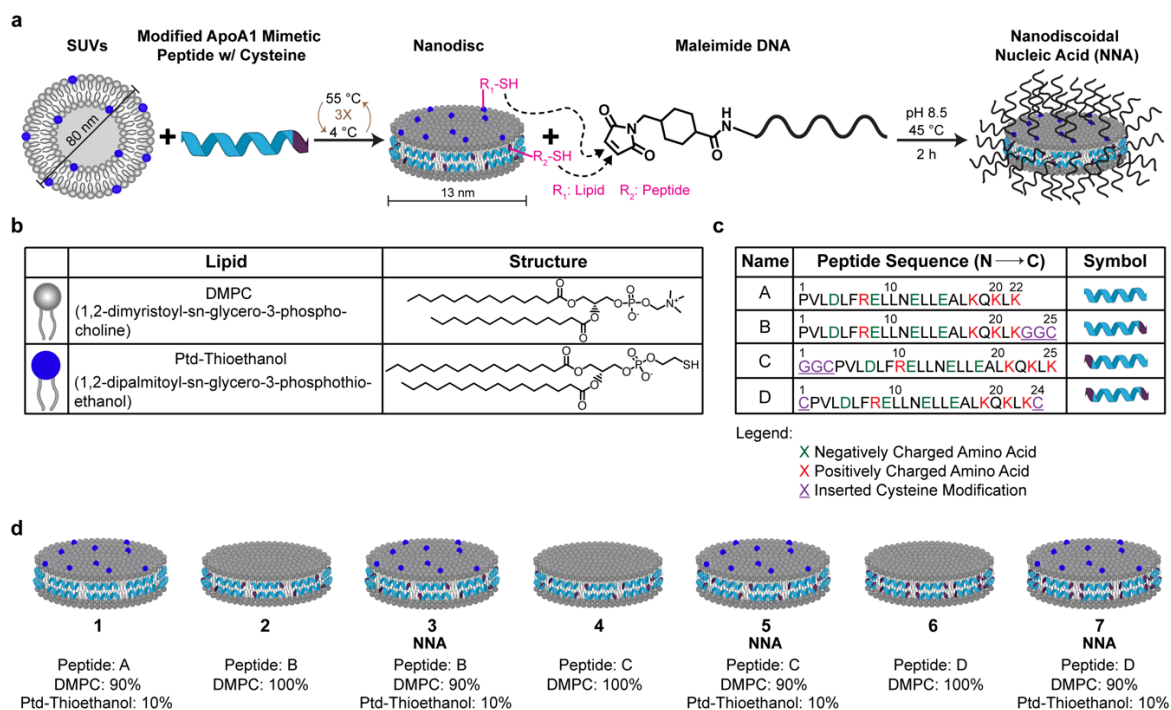


Figure 3.3.1: Assembly and synthesis of nanodiscoidal nucleic acids (NNA). **(a)** Scheme depicting the assembly of NNAs. The ND scaffold is assembled by preparing 80 nm small unilamellar vesicles (SUVs) and combining them with a modified ApoA1 mimetic peptide containing a Cys amino acid insertion. The NNA is generated by conjugating maleimide-linked DNA to the exposed thiols on the surface (lipid) and edge (peptide) of the scaffold. **(b)** Table of lipids used in the assembly of NDs and NNAs. DMPC is the majority component present in the NDs and the thiol lipid, Ptd-Thioethanol (blue), is added to certain discs to prepare NNAs. **(c)** Table of ApoA1 mimetic peptides screened for the formation of NNAs. The original mimetic peptide, denoted as A, does not contain any Cys residues and was further modified in versions B – D at the N- and/or C-terminus. **(d)** Panel of NDs/NNAs generated from the peptide screen as shown in (b). Excluding peptide A, each peptide was used to prepare two different scaffolds one with DMPC exclusively and referred to as NDs and a second type which included thiolated phospholipids and denoted as the NNA.

The DNA-ND and NNA conjugates were visualized before and after DNA coupling using transmission electron microscopy (TEM) (**Figure 3.2.2**). The imaging revealed a monodisperse, homogenous morphology with “coin-like” stack formations, attributed to the rouleaux effect from

the negative staining process,^{52, 114} for NDs 1 - 5 before and after conjugation to DNA (**Figure 3.3.2**). In contrast, NDs assembled using peptide D (**Figure 3.3.1c**) showed heterogeneous morphology prior to and after DNA conjugation. The only exception was ND 6 that showed some stack formation prior to DNA conjugation but these were more disorganized than other NDs tested (1 - 5). The weaker propensity to form intact ND for 6 and 7 is potentially due to the N- and C-Cys modified termini which increase the probability of forming disulfide bridges and aggregation. For NDs 1-5, there was a small (nonsignificant) increase in diameter as measured by TEM, which showed that ND size changing from ~11 – 12 nm before DNA conjugation to ~13 – 15 nm after coupling. DLS measurements (**Figure 3.6.2**) showed a much more substantial increase in particle size as the hydrodynamic radius shifted from ~10 – 13 nm before DNA addition to ~14 – 22 nm after DNA addition. This larger change in size observed in DLS is consistent with the literature for gold nanoparticle and lipid nanoparticles after conjugation with DNA.^{118, 138} Therefore, the TEM and DLS confirm the ultrasmall size of the native scaffold following DNA coupling.

Interestingly, the intensity-normalized DLS data shows an increase in the polydispersity of NDs and specifically the appearance of larger-diameter particles, which was most pronounced for ND 5 (**Figure 3.6.2**). This is due to the formation of a small population of liposomal aggregates that likely form due to formation of disulfide bridges between ND during the DNA coupling reaction as well as destabilization of the ND following DNA-coupling. These aggregates were more distinct for NNA (ND 5) rather than the peptide-DNA and phospholipid-DNA conjugate ND suggesting: 1) that high density DNA on the ND can lead to slight destabilization of the ND and 2) that introducing the Cys to the N-terminus of 22A was slightly more destabilizing. Helical wheel projections indicated that the peptide C places the N-terminal Cys, which is considered polar, within the hydrophobic face of the peptide, and may explain the decreased stability of ND 4 and 5 compared to that of ND 2 and 3 (**Figure 3.6.1**). It has been previously noted that the ND samples display a minor fraction of larger liposomal aggregates and those aggregates scatter light strongly compared to the smaller NDs, hence amplifying the signal in intensity-based DLS

measurements.⁵⁸ This is consistent with our observation as we were not able to see these sub-populations of liposomal aggregates in TEM, and confirming that these species are minor. Taken together, this screen of Cys-modified 22A peptides and thiol containing phospholipids confirms that we generated NNAs that are monodisperse maintaining a ~ 5 nm \times ~ 13 nm disc-like structure based on TEM.

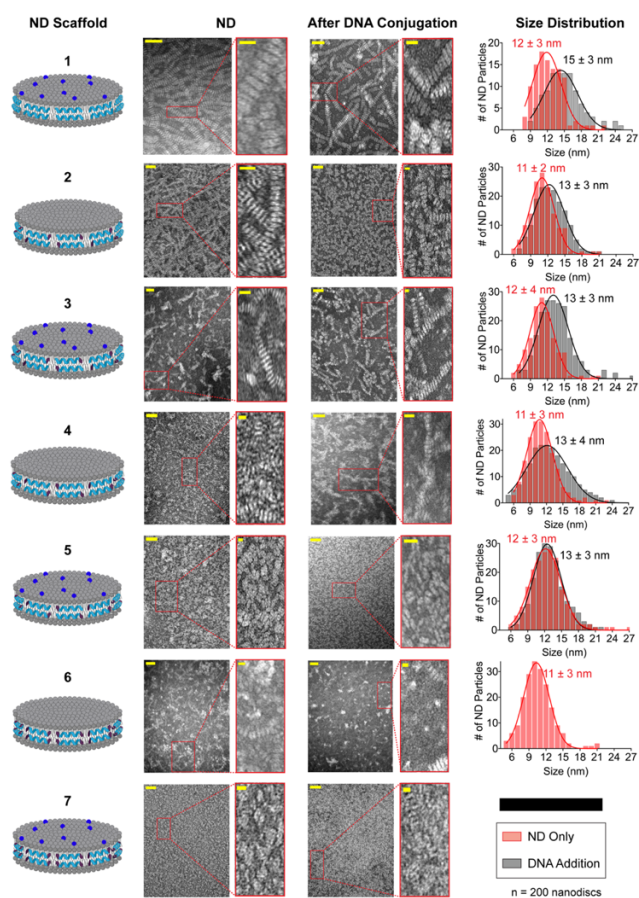


Figure 3.3.2: Transmission electron microscopy imaging of NDs and NNAs. Representative TEM images were shown for each ND prior to and after DNA conjugation. Samples were prepared using a plasmon-etched 400-mesh copper grid, and negatively stained using Nano-W™. Scale bar: 50 nm, zoom-in: 20 nm. Histograms represent binned diameter size distribution of NDs ($n = 200$) before (red) and after (black) DNA coupling for each scaffold (1 – 6). ND 6 after DNA conjugation and ND 7 before and after DNA conjugation appeared to form lipid aggregates instead of discoidal NDs, and therefore we do not show histograms for these NDs.

We next measured DNA density on NDs 1-5 using the OliGreen™ assay and found that the NNAs (NDs 3 and 5) had the greatest DNA density per disc (**Figure 3.3.3a**). ND 1 only presented thiols on the phospholipid and led to 11 ± 5 DNA strands per ND. ND 2, which displayed Cys at the peptide C-terminus afforded 16 ± 1 DNA strands per ND. These values are consistent

with our simple calculations^{40, 62} that estimate that there are 4-fold more thiol group on peptides compared to that of the phospholipids. Unsurprisingly, ND 3 displayed 25 ± 7 DNA strands per ND which suggests that DNA coupling can efficiently proceed on both the phospholipid and peptide with minimal steric clash. ND 4 displayed a lower density compared to the ND 2 and this is likely to the stability issue of peptide D (**Figure 3.6.1**). Finally, ND 5 showed the largest density of 35 ± 14 DNA strands per ND. While the average density of these NNAs was the greatest, these values were heterogenous and displayed high variability which likely relates to the broader size distributions measured by DLS. Accordingly, student's t-test analysis comparing the two NNAs did not show statistical significance in their DNA densities and hence ND 3 is more attractive as a therapeutic candidate given its enhanced monodispersity and consistent DNA density. We also compared the DNA density of NNAs to that of spherical nucleic acids comprised of a gold nanoparticle core, which have similar diameters and present the highest density of DNA and showed that NNA are approaching the DNA densities for those structures (**Table 3.6.1**).

To validate that the DNA is covalently linked to the ND, we further performed a series of characterization experiments using FRET (**Figure 3.3.3b,c**). Here we used TYE563 fluorophore tagged ASOs that target HIF-1- α (**Table 3.6.3**) as the donor whereas the ND was tagged with an acceptor dye (1% Cy5 headgroup modified phospholipid). We excited the TYE563 donor at $\lambda = 525$ nm and collected the emission spectra (**Figure 3.3.3b**) quantifying sensitized emission from Cy5. Qualitatively, Cy5 emission at $\lambda = 670$ nm compared to direct donor emission ($\lambda = 560$ nm) was greatest for ND 1, 2, and 3 compared to controls where the DNA was not covalently linked to ND or when the ND lacked the Cy5 acceptor or when the donor was absent. FRET efficiency was quantified by using the ratio of donor emission normalized to the donor emission in the absence of the acceptor (**Equation 4**) and this data was plotted in **Figure 3.3.3c**. Using this analysis, we found that the ND 1, 2, and 3 showed greater quantitative FRET (40-70%) compared to that of controls where the ND and DNA were present in the solution but not covalently linked

(2%). Interestingly, we also found that the ND with DNA linked to the peptide showed lower FRET efficiency compared to ND with DNA linkage to the phospholipid. This was consistent with the expected geometry of the ND with the peptide-linked DNA lying at the periphery of the ND and increasing the distance between the phospholipid headgroups with the acceptor and the donor dyes.

To further validate the covalent attachment of the DNA to the ND, we next ran gel electrophoresis of NDs that were labeled with 0.15% Cy5 phospholipid and coupled to DNA. The gel is shown in **Figure 3.3.3d** and for ease of visualization, SYBR Gold emission from the DNA was pseudo colored yellow while the Cy5-phospholipid emission was pseudo colored red. NDs 1-5 that were conjugated to DNA showed different mobility compared to an ND scaffold only, DNA mixed with ND (but unconjugated), and soluble DNA only. As expected, upon DNA conjugation, the ND and associated phospholipid migrated more rapidly through the gel compared to the NDs lacking DNA. Additionally, the DNA mobility was slowed upon ND conjugation. Taken together, the gel electrophoresis results along with the FRET analysis confirm covalent coupling of the DNA to the ND both through peptide as well as phospholipid coupling.

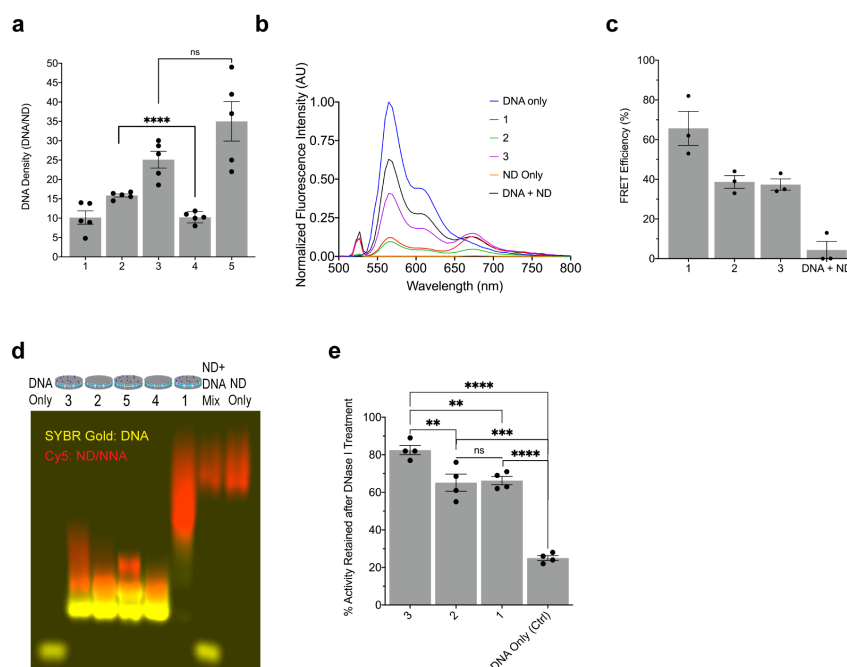


Figure 3.3.3: Characterization of DNA-ND and NNA conjugates and their nuclease resistance. **(a)** DNA density plot comparing the number of DNA strands per ND scaffold (1 – 5) after covalently conjugating the maleimide-DNA to the

thiol/cysteine bearing NDs. There is an increase in the amount of DNA added to a ND when using the NNA scaffolds (NDs 3 and 5). Data represents an average of $n = 5$ independent replicates. **(b)** Fluorescence spectra for the DNA-NDs (NDs 1 – 2) and NNA (ND 3) samples prepared with 1% Cy5 phospholipid and DNA was tagged with TYE563 fluorophore. Fluorescence spectra were collected for DNA (100 nM) concentration when excited at $\lambda = 525$ nm. **(c)** Plot of the calculated FRET efficiency for the DNA-NDs and NNAs against the DNA mixed with ND (no attachment). The higher FRET efficiencies (37% - 66%) present in the conjugated sample compared to the control (~ 2%) validate the attachment of the DNA on the surface and the peptide of the ND. Data represents an average of $n = 3$ independent replicates. **(d)** Agarose gel electrophoresis of the DNA-ND and NNA conjugates (NDs 1 – 5), DNA mixed with ND, DNA only, and ND only samples. NDs (red) were prepared with 0.15% Cy5 phospholipid, and the gel for sample analysis was prepared with 1.5% agarose in TAE buffer, with in-gel staining for DNA using SYBR gold (yellow). Retardation of the DNA bands (NDs 1 – 5) compared to the unbound free DNA control further indicate that the DNA is covalently bound to the discs. **(e)** Plot showing the percent activity retained after conjugating a catalytically active DNAzyme to the ND forming DNA-NDs (1 – 2) and NNA (3) and exposing them to 1 U of DNase I for 2 h. The NNA scaffold displayed enhanced protection against DNase I because it displayed higher activity (83%) compared to the DNA conjugated to the surface (1) and peptide (2), which retained ~65% activity, whereas the unbound soluble DNAzyme (denoted as DNA) retained only 25% of activity. Each data point represents an independent replicate ($n = 4$). ** $p < 0.01$, *** $p < 0.001$, **** $p < 0.0001$. Error bars represent SEM.

Prior work on DNA modified gold nanoparticles showed that increasing the density of DNA can lead to enhanced DNase resistance and thus, we next tested whether NNA's demonstrate this phenomenon which would be beneficial for boosting nucleic acid drug efficacy. We compared the stability of the NNA structure (ND 3) to soluble DNA and representative DNA-ND samples (NDs 1 and 2). For this work, we used deoxyribozymes (DNAzymes) because their catalytic activity is easily measurable, their catalytic function is fully recovered after heat inactivation and DNAzyme activity is highly sensitive to cleavage; even hydrolysis of a single nucleotide from a DNAzyme leads to clearly detectable changes in enzyme activity.^{118, 139} We exposed the NNA and DNA-ND samples to 1 U of DNase I (**Figure 3.3.3e**) for 2 h prior to inactivating the DNase I and assessing functional multiturnover kinetics of the DNAzyme using a dual-labeled mock RNA substrate (**Table 3.6.3**).^{103, 115} We found that the NNA structure offered greater nuclease resistance compared to the DNA-ND samples (83% activity retained vs 66% respectively), most likely due to steric crowding as well as the high local charge density of the NNA.¹⁴⁰ Notably, the nucleic acid used in this sequence was unmodified nucleobases. These data suggest that the ND scaffold provides enhanced protection against nucleases, further improving its potential for delivering therapeutic nucleic acids.

3.3.2: NNAs are Internalized into Cells via Scavenger Receptor B1

In principle, virtually any ASO can be conjugated to NDs to form NNAs, but here we tested the clinically relevant EZN2968 HIF-1- α targeting ASO.¹¹⁰ The HIF-1- α targeting ASO was tagged with a 5' TYE563 while the ND was labeled with 1% Cy5 to aid in quantifying cell uptake using confocal microscopy (**Figure 3.3.4a**). HeLa cells were incubated with 100 nM (with respect to DNA concentration) of representative ASO-ND (1 – 2) and NNA (3) samples and then imaged at 3 h and 24 h timepoints. We observed a time-dependent increase in accumulation of the NNAs and ASO-NDs as noted by the increased signal for ND 1, 2, and 3 in confocal imaging of single cells. Also, the lipid-Cy5 and DNA-TYE563 signals generally became more dispersed, less colocalized and less punctate at 24 h, as shown in the images and representative linescans. These observations suggest escape of these conjugates into the cytoplasm at later time points. In contrast, at the early 3 h timepoint, the NNAs and ASO-NDs displayed lower total signal and more punctate clusters where the TYE563 signal was colocalize to the Cy5 signal. Moreover, the TYE563 and Cy5 signals tended to localized towards the cell edge at early time points suggesting that a fraction of the ND are docked to the membrane⁸⁹ or internalized and trapped inside endosomes that are near the membrane.

Next, we sought to examine the mechanism of NNA uptake into the cell and specifically the role of SRB1 for mediating uptake. SRB1 primarily interacts with the helices of ApoA1 and ApoA1 mimetic peptides bidirectional transfer of cargo into the cell using a non-endocytic mechanism.³⁴

Next, we sought to examine the mechanism of NNA uptake into the cell and specifically the role of SRB1 for mediating uptake. SRB1 primarily interacts with the helices of ApoA1 and ApoA1 mimetic peptides bidirectional transfer of cargo into the cell using a non-endocytic

mechanism.³⁴ It is plausible that ASO conjugation to the peptide would interfere with the SRB1 recognition and disrupt ASO transfer, potentially diminishing the utility of the NNAs.

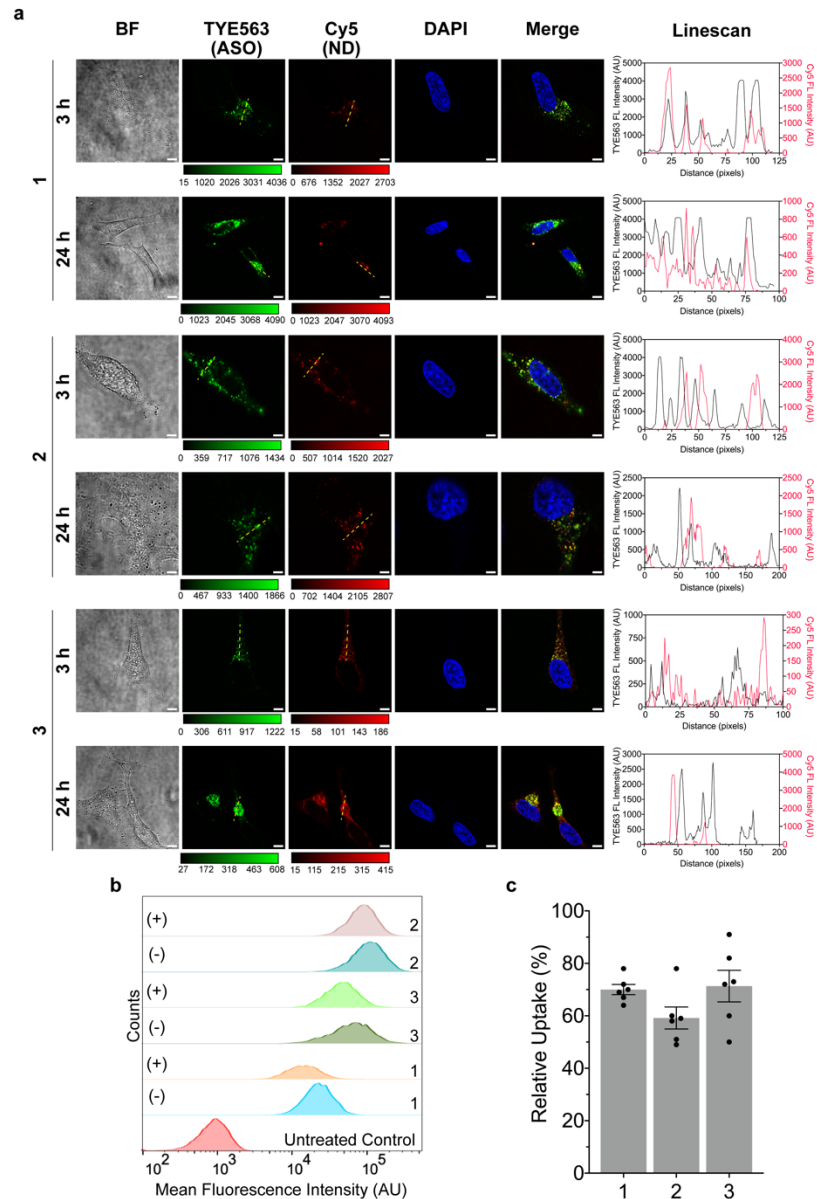


Figure 3.3.4: ASO-NDs and NNAs show cell uptake which is dependent, in part, on Scavenger Receptor B1 (SRB1). **(a)** Representative confocal images showing a time course for the increased uptake of 100 nM ASO-NDs (NDs 1 – 2) and NNA (ND 3) in a time-dependent manner into HeLa cells. Panel includes brightfield (BF) image, and fluorescence intensity of TYE563 (ASO) and Cy5 (1% Cy5 phospholipid for NNA). Images were taken at 3 h and 24 h and cells were fixed and stained with DAPI prior to imaging with a 60× oil objective. Scale bar: 5 μm. Linescans for the Cy5 and TYE channels are shown to the right and were generated from the yellow dashed lines shown in the images. **(b)** Histograms displaying the difference in uptake of ASO-NDs (NDs 1 – 2) and NNA (ND 3) after incubating cells with 50 μm BLT-1 for 1 h prior to incubation with 15 nM ND (400 nM ASO) for 2 h. NDs were prepared with 0.15% Cy5 phospholipid. SRB1 uptake was compared to NDs/NNAs treated with BLT-1 (denoted as ‘+’) against samples treated without BLT-1 (denoted as ‘-’). The flow data represents mean Cy5 intensities from a minimum of 5000 cells. Raw intensity values for all the replicates are shown in **Figure 3.6.3**. **(c)** Graph comparing the uptake of the ASO-NDs (NDs 1 – 2) and NNAs (ND 3) after BLT-1 treatment. The uptake values are normalized and compared to the uptake level of samples without BLT-1 treatment as a control. This suggests that the SRB1 is prominently involved in the uptake and internalization of

ASO-NDs and NNAs into the cell, although it is not the only mechanism. Data represents an average of $n = 6$ independent replicates. Error bars represent SEM.

SRB1 activity was diminished with a small molecule inhibitor named blocker of lipid transport (BLT-1).¹⁴¹ BLT-1 is well established and binds to the key amino acid residue C384, which has a key role in selective cellular uptake of SRB1.¹⁴² Upon treating HeLa cells with BLT-1 (50 μ M) and incubating with the panel of ASO-ND and NNA conjugates (1 – 5), cells were collected to assess the mean Cy5 fluorescence intensity of the ND scaffold (labeled with Cy5) via flow cytometry (**Figure 3.3.4b**). To our surprise, there was a significant reduction in the uptake of ASO-NDs and NNAs into cells following BLT-1 treatment for all the NDs tested (**Figure 3.6.3**). This reduction correlated into 56 – 73% reduction in uptake for all groups (**Figure 3.3.4c**) when the uptake was compared and normalized against the uptake for cells treated with ASO-NDs and NNAs without BLT-1 treatment. This partial reduction in uptake of ASO-NDs and NNAs suggest that > 50% of the uptake route involves other mechanisms, such as endocytosis or lipid fusion with the plasma membrane. It is known that the uptake of miRNA from HDL particles is dependent on SRB1, but the mechanisms of how SRB1 mediates cholesterol and miRNA transport has not been elucidated.^{22, 72, 89} The covalent attachment of the ASO to phospholipids is not likely to not limit SRB1 uptake because phospholipids are also internalized by SRB1 through the selective lipid uptake pathway during cargo transport and catabolism of the HDL scaffold.¹⁴³ In contrast, the ND-forming peptide itself is not known to be trafficked using the SRB1 pathway, but it is likely that the amphipathic peptide-oligonucleotide conjugate may undergo internalization as noted for amphipathic cell penetrating peptides.^{144, 145} While endocytosis may inevitably play a role for internalization for all nanoparticles, these experiments showing SRB1-dependent uptake enhance the therapeutic potential of NNAs as it limits endosome entrapment and eventual degradation. This data demonstrates that the C-terminal Cys modified 22A peptide design and nucleic acid conjugation does retain the selective, non-endocytic features of the ND scaffold.

3.3.3: Internalized ASO-NDs and NNAs Undergo Dissociation with 24 h

To better characterize the integrity of ASO-NDs and NNAs after internalization into the cell, we used sensitized-FRET¹⁴⁶ to determine lipid-nucleic acid proximity (**Figure 3.3.5a**). Similar to the uptake studies, HeLa cells were incubated with 100 nM of ASO-NDs (1 – 2) and NNA (3) for 4 and 24 h. After rinsing and nuclear staining of the cells, the samples were imaged on an epifluorescence microscope using a FRET cube equipped to measure FRET using the TYE563 and Cy5 wavelengths (**Figure 3.3.5b**). FRET efficiency was determined by using a pixel-by-pixel analysis method (**Figure 3.6.4**) that accounted for cross talk between the donor and acceptor channels.¹⁴⁷ For all the ND sample types that were examined, we noticed a decrease in FRET efficiency when we compare values at 4 h and 24 h (**Figure 3.3.5c–e**). This confirms that ASO-ND conjugates dissociate over this time window. As expected, there were no detectable FRET for the ND scaffold only, DNA only, and the ND mixed with the DNA at the 4 and 24 h time points (**Figure 3.6.5**). It is important to note that because the donor and acceptor are not directly linked to the same molecule, the FRET efficiency for our ND conjugates is inherently lower due to a larger Förster radii, and especially for the ASO-ND 2 where the ASO is conjugated to the scaffolded peptide. The FRET efficiencies measured for all samples at $t = 4$ h were 36% for ASO-ND 1, 24% for ASO-ND 2, and 48% for NNA 3. There was not sufficient uptake of ND at $t = 0$ to quantify DNA-ND and NNA integrity at early time points. Thus, we next measure FRET efficiency at 24 h and found values of 23% for ASO-ND 1, 7% for ASO-ND 2, and 37% for NNA 3. This data shows that the ASO-ND and NNA assemblies are gradually dissociating. The disassembly of ASO-ND constructs is due to the activity of a combination of proteases, lipases, and nucleases as well as the retro-Michael (maleimide-thiol) reaction which releases the ASO from the ND and occurs under physiological conditions in the cytoplasm (i.e., highly reducing environment from glutathione).¹⁴⁸ Note however that for activity purposes it is not required that the ASO be strictly localized to the NNA and in fact, release from the scaffold can enhance the activity of ASO in the cell to bind mRNA, recruit RNaseH, and block the ribosome.

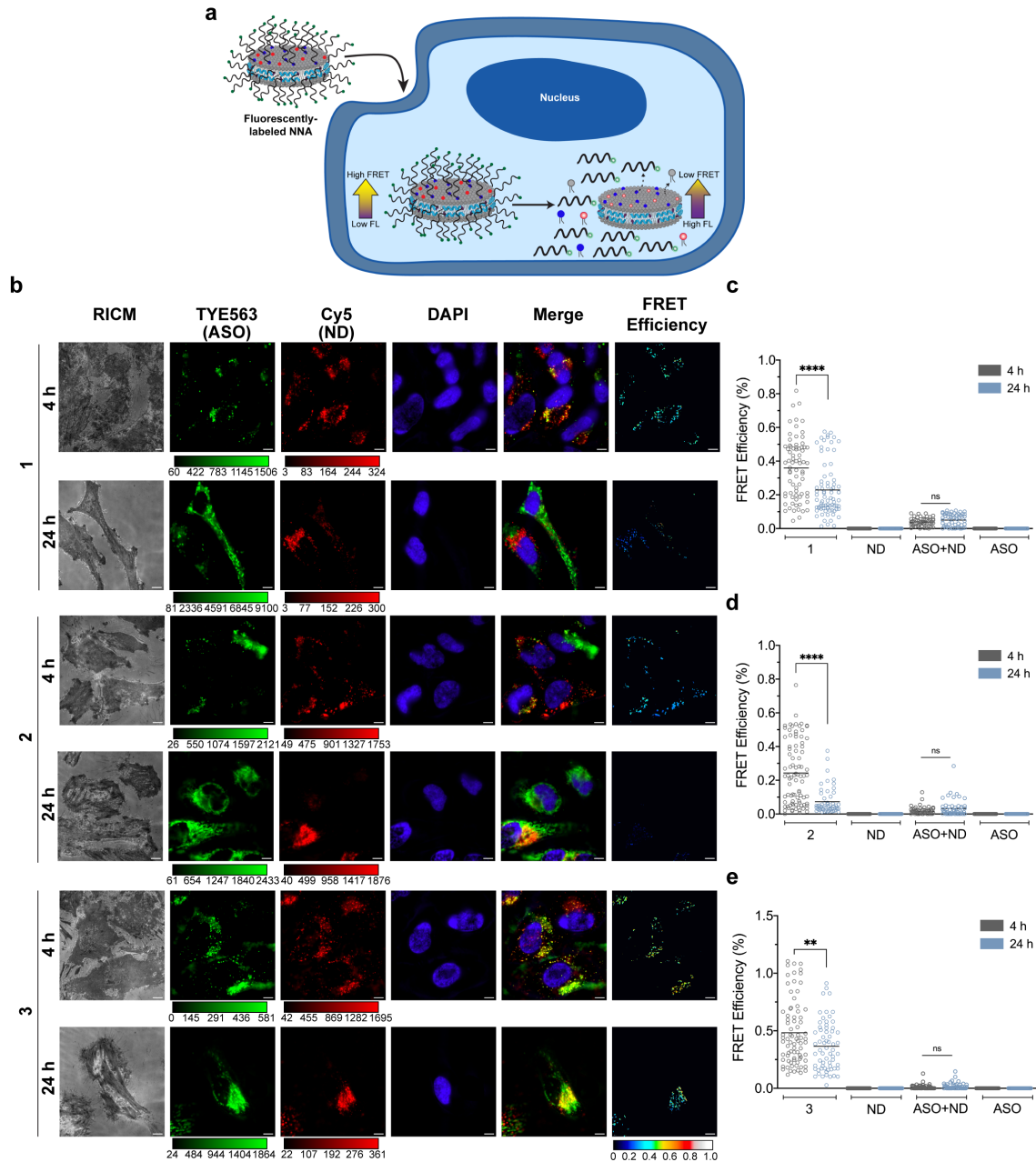


Figure 3.3.5: Sensitized-FRET assays reveal that ASO-NDs and NNAs measure disassembly of the ASO from the ND scaffold within 24 h in HeLa cells. **(a)** Scheme detailing the mechanistic application of FRET for ASO-NDs and NNA internalization inside a cell. Conjugated ASO-NDs (NDs 1 – 2) and NNA (ND 3) will display low fluorescence in the donor channel because of higher FRET, and vice versa is expected for ASO-NDs and NNAs once the nucleic acid detaches from the scaffold. **(b)** Representative epifluorescence images showing a change in FRET when cells were incubated with 100 nM ASO-NDs (NDs 1 – 2) and NNA (ND 3). Panel includes a RICM image, and fluorescence intensity of TYE563 (ASO) and Cy5 (1% Cy5 phospholipid for NNA). Images were taken at 4 h and 24 h and cells were fixed and stained with DAPI prior to imaging with a 100× oil objective using a FRET cube. FRET images were generated from thresholding the acceptor channel (ND) and parsing the pixels and correcting for bleedthrough from donor and acceptor (ASO). Calibration bar represents FRET efficiency (set between 0 – 1.0) Scale bar: 5 μm. Plot of FRET efficiencies for ND scaffold 1 **(c)**, 2 **(d)**, and 3 **(e)** depicting a decrease in FRET over time from 4 h to 24 h. The NNA sample (ND 3) demonstrated a higher FRET efficiency at 24 h compared to ASO-NDs (1 – 2), suggesting that it takes a longer time for the ASO to dissociate from the ND scaffold. ND mixed with ASO, ASO only, and ND only were used as controls and showed no FRET efficiency as they were not conjugated to a scaffold. Epifluorescence microscopy

images are shown in **Figure 3.6.5**. An average of $n = 30$ cells were analyzed for each sample and $** p < 0.01$, $**** p < 0.0001$.

3.3.4: Quantifying NNA and ASO-ND Activity *In Vitro*

In these sets of experiments, we aimed to compare the activity of the ASO conjugated NDs and NNA scaffolds by measuring HIF-1- α transcript levels using qPCR. HeLa cells were incubated with 100 nM ASO-ND or NNA for 24 h before cells were lysed and RNA was collected for qPCR. All treatment groups had an ASO concentration of 100 nM and this was validated using the extinction of DNA at $\lambda = 260$ nm. In general, we noted that the NNA scaffolds showed activity towards reducing basal HIF-1- α mRNA levels (**Figure 3.3.6a**). Of the constructs tested, ND 2 and ND 3 (NNA) showed greater levels of activity compared to ND 4 and ND 5 (NNA). In other words, conjugation of the ASO to the C-terminal cysteine of the ApoA1 mimetic peptide generated NDs that were significantly more active than ASO's conjugated to the N-terminus of the peptide. Overall, NNA (ND 3) showed the greatest level of activity (58% reduction of cellular HIF-1- α levels), suggesting that creating a high density of ASO around the ND scaffold leads to improved activity per ASO. ASO-ND 4 showed the least activity (24% knockdown), and the relatively lower activity of ND 4 and ND 5 (NNA) is attributed to the destabilizing effects (and larger aggregates) of linking the DNA to an N-terminal Cys that resides in the hydrophobic face of the peptide as suggested by the helical wheel diagram (**Figure 3.6.1**). This lower activity is further supported by TEM analysis and DLS that showed more broadly distributed NDs and a subpopulation of lipid assemblies with > 100 nm (**Figure 3.6.2**). Because cancer cells typically have an overreliance on glycolysis (Warburg effect) and HIF-1- α expression maintains upregulated glycolysis levels, knockdown of HIF-1- α can contribute to reducing cell viability.¹⁴⁹ We thus validated the qPCR quantification of HIF-1- α by also measuring cell viability of HeLa cells treated with 100 nM of ASO-NDs and NNAs for 24 h using an MTT assay (**Figure 3.3.6b**). Overall, all ASO-ND and NNA conjugates used for this study displayed significant reduction in cell viability when compared

against treatment with a scrambled ASO. Consistent with the qPCR results, NNA (ND 3) showed the greatest reduction in HeLa cell viability (42% reduction) compared to the other scaffolds (1 – 2, 4 – 5). Taken together, this data identifies NNAs using ND 3, as the most potent scaffold for gene regulation.

To validate the activity of NNAs in other cell types, we next tested HIF-1- α knockdown in three other model cell lines including KPC (**Figure 3.3.6c**), LX-2 human stellate (**Figure 3.3.6d**), and HepG2 (**Figure 3.3.6e**). These cell lines were chosen because of their intrinsic overexpression of HIF-1- α and represent different disease models (e.g., KPC: pancreatic ductal adenocarcinoma, LX-2: hepatic fibrogenesis in NAFLD, and HepG2: hepatocellular carcinoma) which are often exacerbated by abnormal levels of hypoxia. In each of these cell lines, there was a significant decrease in cellular HIF-1- α levels when treated with 100 nM of NNA (ND 3) for 24 h compared to the scrambled ASO. The NNA treatment displayed slightly more activity compared to that of soluble ASO only. These data conclude that the NNA conjugate prepared from peptide B is active *in vitro* as we can confirm from validating its activity in multiple cell lines.

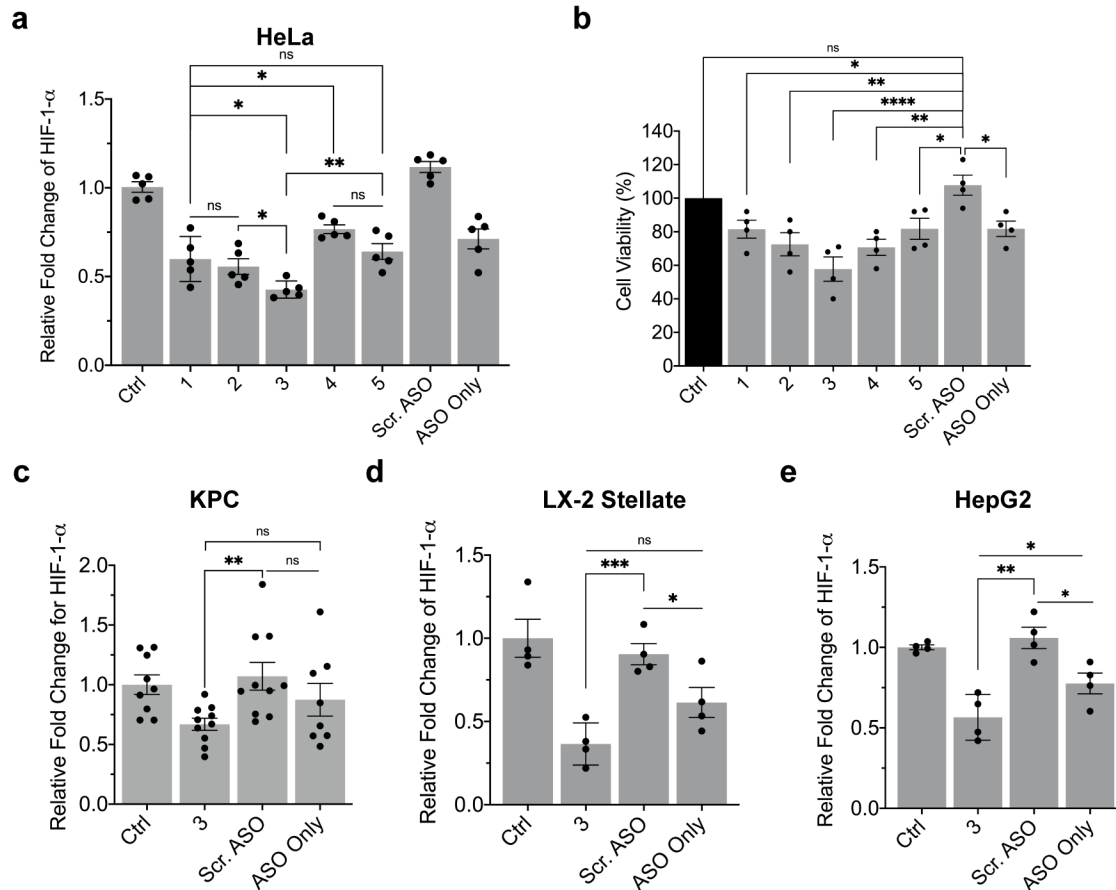


Figure 3.3.6: Quantifying the functional activity of ASO-NDs and NNAs for reducing HIF-1- α mRNA levels in different cell lines. **(a)** Plot of HIF-1- α levels after incubating HeLa cells with ASO-NDs (NDs 1 – 2, 4) and NNAs (NDs 3 and 5) for 24 h prior to extracting mRNA and quantifying the levels via RT-qPCR. The anti-HIF-1- α ASO (EZN2968) was used for this study and the ASO concentration was 100 nM for all groups, including the scrambled (scr.) ASO (conjugated on a ND) and ASO only. The ASO-ND and NNA conjugated to the peptide on the C-terminus (NDs 2 – 3) had greater activity compared to the N-terminus (NDs 4 – 5). Data represents an average of $n = 5$ independent replicates. **(b)** Assessment of cell viability using MTT assay. HeLa cells were subject to 100 nM of ASO-ND or NNA and incubated for 24 h prior to adding MTT reagent and performing the assay. The values are normalized to the OD measured at 590 nm for the untreated cells as a control (ctrl). Cells treated with ASO-ND or NNAs demonstrated a significant reduction in viability, further confirming the functional activity of the conjugates. Each data point represents the percent viability for one replicate ($n = 4$ independent replicates). **(c)** Quantification of HIF-1- α levels as determined via RT-qPCR in **(c)** KPC, **(d)** LX-2 Human Hepatic Stellate, and **(e)** HepG2 cells after incubating cells with 100 nM of NNA (ND 3), scrambled (scr.) ASO on a ND, and ASO only for 24 h. Transcript levels are normalized to the untreated control group (ctrl). The NNA scaffold significantly boosted ASO activity compared to cells administered 100 nM of ASO only without a scaffold. Data represent an average of a minimum of $n = 4$ independent replicates. and * $p < 0.05$, ** $p < 0.01$, *** $p < 0.001$, **** $p < 0.0001$. Error bars represent SEM

3.3.5: NNAs Penetrate into the Hypoxic Core of Tumor Spheroids and Express High Activity

As a stepping stone toward *in vivo* validation of NNA activity, we next employed a cancer spheroid model as a representative tumor model. Tumors typically consist of a poorly oxygenated and poorly vascularized necrotic core.¹⁵⁰ The highly hypoxic core presents with diffusional selectivity and most drugs face mass transport barriers which limits delivery to the necrotic core.¹⁵¹

One would expect that larger scaffolds and higher molecular weight drugs, such as NNAs, would experience significant barrier to reaching the core of tumor spheroids. On the other hand, tumors and other malignant cell lines highly express SRB1, thus making it possible to deliver cargo into the spheroid. To test whether NNA can penetrate the hypoxic core of spheroids, we used the most active NNA (ND 3) in subsequent experiments with the three-dimensional H1299 non-small cell lung cancer (NSCLC) spheroid model. Spheroids embedded in Matrigel were incubated with 100 nM of NNA or ASO for 24 h before visualizing using confocal microscopy (**Figure 3.3.7a**). Representative images show that there was a marked increase in NNA uptake into the core of the spheroid compared to the ASO only treatment. The soluble ASOs tended to internalize into the quiescent and proliferating areas (closer to surface and edges) of the spheroid. This was quantified by running a radial profile analysis of $n = 14$ spheroids (**Figure 3.3.7b**). The radial scans were initiated from the center of the spheroid out to the edge as determined from the brightfield image. The radial profile of soluble ASOs showed weak signal in the core of the spheroid and a gradual increase before leveling off in the proliferating zone. Conversely, the NNA treatment shows a rather uniform level of ASOs throughout the spheroid, highlighting the deeper penetrative ability of these discs. This confocal analysis strongly suggests that NNAs would provide a more effective strategy to deliver greater doses of ASOs to tumors. To quantify total uptake, we next used flow cytometry to compare ASO uptake when the ASO was linked to the NNA compared to soluble DNA. We found that NNA uptake was significantly greater than that of the ASO only treatment when directly evaluated using flow cytometry (**Figure 3.3.7c,d**). Thus, NNAs offer a

significant improvement in delivery to tumor spheroids both in terms of total uptake as well as delivery to the hypoxic core.

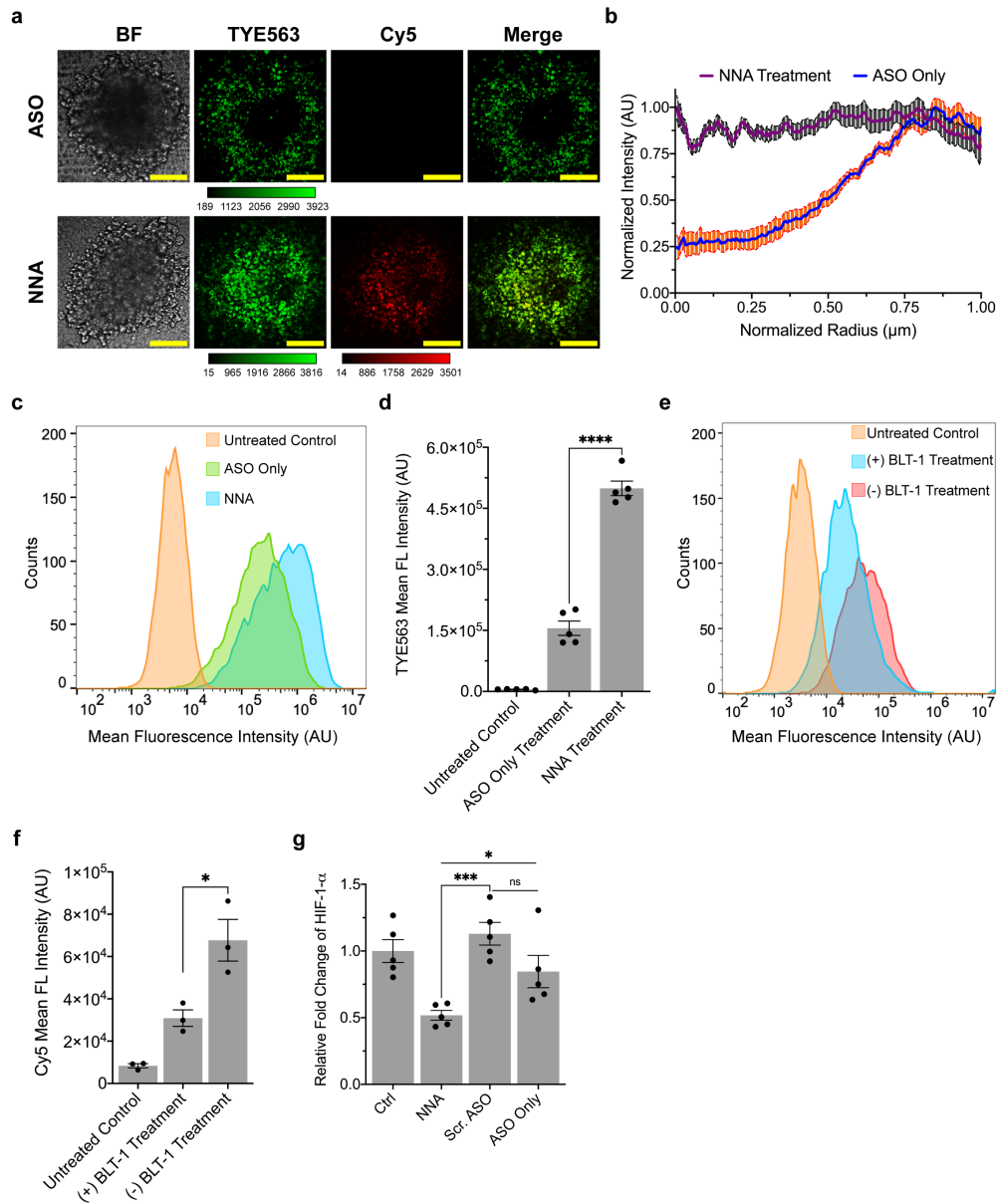


Figure 3.3.7: NNA uptake and functional activity in H1299 3D spheroids. **(a)** Confocal images of internalized NNAs and ASO (EZ2968) visualized inside the spheroid cross section at the middle slice after 24 h of incubation (ASO concentration = 100 nM). Panel includes brightfield (BF) image and fluorescence intensity of TYE563 (ASO) and Cy5 (NNA). Scale bar: 15 μm . **(b)** Radial profile scan averaging TYE563 fluorescence intensity and normalizing for 14 spheroids ($n = 3$ independent replicates). The profile scan reveals that the NNA uptake is more enhanced for spheroids, with the ability to penetrate the hypoxic core within 24 h. **(c)** Representative flow cytometry histogram depicting cell uptake when comparing between the spheroids treated with ASO only and the NNA (ND 3) treatment. The flow data represents mean TYE563 intensities from a minimum of 5500 cells. **(d)** Mean TYE563 fluorescence quantification on the uptake of ASO and NNA (ND 3) as measured via flow cytometry. Each data point represents the average of 6 spheroids ($n = 3$ independent replicates). **(e)** Representative flow cytometry histogram depicting the difference in uptake of NNAs into spheroids after blocking SRB1 with 50 μm of BLT-1 for 1 h. NNAs (150 nM ASO and 6 nM ND) were subsequently incubated with spheroids for 2 h prior to dissociating the spheroids into individual cells and measuring cell associated fluorescence using flow cytometry. The flow data represents mean Cy5 intensities from a minimum of

5000 cells. **(f)** Mean Cy5 fluorescence quantification for the uptake of NNA (3) into spheroids treated with BLT-1. There is a 54% reduction in the uptake of NNAs after BLT-1 treatment. Each data point represents an average of 8 spheroids ($n = 3$ independent replicates). **(g)** Plot comparing the HIF-1- α levels as measured by RT-qPCR after subjecting the spheroids to 550 nM of ASO, ASO on NNA, or scrambled (scr.) ASO on a ND for 24 h. Transcript levels are normalized to the untreated control group (ctrl). Each data point represents an average of 5 spheroids ($n = 3$ replicates) and * $p < 0.05$, ** $p < 0.01$, *** $p < 0.001$, **** $p < 0.0001$. Error bars represent SEM.

We next aimed to test the role of SRB1 in mediating NNA penetration to the necrotic core of spheroids. Here, we treated spheroids with 50 μ M BLT-1 for 1 h before adding 6 nM Cy5-ND (150 nM ASO) for 2 h. Spheroids were dissociated into individual cells and the Cy5 fluorescence was measured using flow cytometry (**Figure 3.3.7e**). There was a 54% ($p < 0.0001$) decrease in uptake in the spheroids treated with BLT-1 compared to untreated spheroids (**Figure 3.3.7f**). This confirms that SRB1 plays a major role in NNA mediated delivery of ASOs to spheroids. This was not unsurprising, as other work suggests an important role for SRB1 in ND uptake.²⁴ Furthermore, the small size of the ND, compared to other types of nanoparticles such as liposomes, greatly expedites transport across the extracellular matrix and interstitial openings.¹⁵²

Lastly, we tested activity of anti-HIF-1- α NNA by treating the spheroids with 550 nM of ASO or NNA for 24 h. Treatment of spheroids at this dosage resulted in an average 49% reduction in cellular HIF-1- α levels (**Figure 3.3.7g**). Additionally, spheroids treated with just ASO resulted in only a 16% reduction in cellular HIF-1- α mRNA. The NNA conjugate exhibited significant potency against the ASO only treatment, hence signifying the potential for using NNAs to deliver nucleic acids as a form of cancer therapy for mediating hypoxia and sensitizing malignant tumors for increased response from other drug treatments.

3.3.6: Anti-HIF-1- α NNAs are Active *In Vivo*

We next aimed to test whether NNAs are active *in vivo* using a mouse model. We designed the experiment, as shown in **Figure 3.3.8a**, where a single tail-vein injection of the NNA or ND scaffold, and was subsequently followed 48 h later with analysis of HIF-1- α gene expression in different tissues. EZN2968 anti-HIF-1- α ASO was conjugated to the NNA as describe above,

purified, and then quantified by UV-Vis to determine the concentration. We delivered 200 μ L of approximately 5 mM NNA and ND solutions that were doped with 1% Cy5 phospholipid. The DNA concentration was approximately 58 mM which is equivalent to a dose of 0.7 mg/kg of the ASO into C57BL/6 mice by tail-vein injection (**Figure 3.3.8a**). Live trafficking of the NNA and ND scaffold was visualized *in vivo* using a whole-body imaging at $t = 6$ h and 24 h post-injection (**Figure 3.3.8b**). Most of the localization of the NNA at $t = 6$ h was in the abdominal area (liver and kidneys), with some minor accumulation near the bronchial area. In contrast, the ND control scaffold was more uniformly distributed and was still present in the tail-vein at the 6 h time point. This more rapid localization of NNA's to the liver/kidney maybe the result of the ASO, which increases the molecular weight and hydrodynamic size of the particles, which also increases cell uptake.¹⁵³⁻¹⁵⁵ Within 24 h, the injected ND scaffold and NNA was localized primarily to the abdominal area. At 48 h post-injection, organs were harvested for *ex vivo* imaging (**Figure 3.3.8c**). The NNA conjugates accumulated in liver, kidney, spleen, lung, and fat tissues which was also noted for the ND. The amount of uptake as inferred from the total fluorescence intensity of the tissues indicated comparable levels for the ND and NNA. Fluorescence quantification detailed that the kidney and liver were the two major organs for internalizing the NNA and ND scaffold (**Figure 3.3.8d**). This is consistent with prior research reporting ND uptake.^{24, 79} RNA was extracted from harvested organs and the relative HIF-1- α levels in each organ was evaluated through qPCR. We noted knockdown of HIF-1- α following NNA treatment in the liver and kidney tissues, with the kidney knockdown showing statistical significance ($p < 0.01$). Importantly, tissues that showed weaker uptake, such as spleen, lung, and fat, showed no observable decrease of HIF-1- α as was expected (**Figure 3.3.8e, Figure 3.6.6**). These results are consistent with experiments reported by Enzon Pharmaceuticals¹¹⁰ where a 3.6 mg/kg dose was injected daily over a 2-week timeframe was the minimum that resulted in significant knockdown of HIF-1a in kidney and liver tissues. Dosing at 0.7 mg/kg with daily injections of soluble ASO did not show

significant knockdown by Enzon and this suggests that the NNA conjugation increases efficacy of the therapeutic (~5-fold lower than the minimum effective dose used in the parent study) over a shorter timeframe (2 days vs. 14 days). This data further confirms the therapeutic potential of NNAs. Aside from lowering the effective dose required (and by extension reducing patient side effects that can result from oligonucleotide drugs), the direct targeting features bestowed by the NNA may reduce the overall time required for treatment.

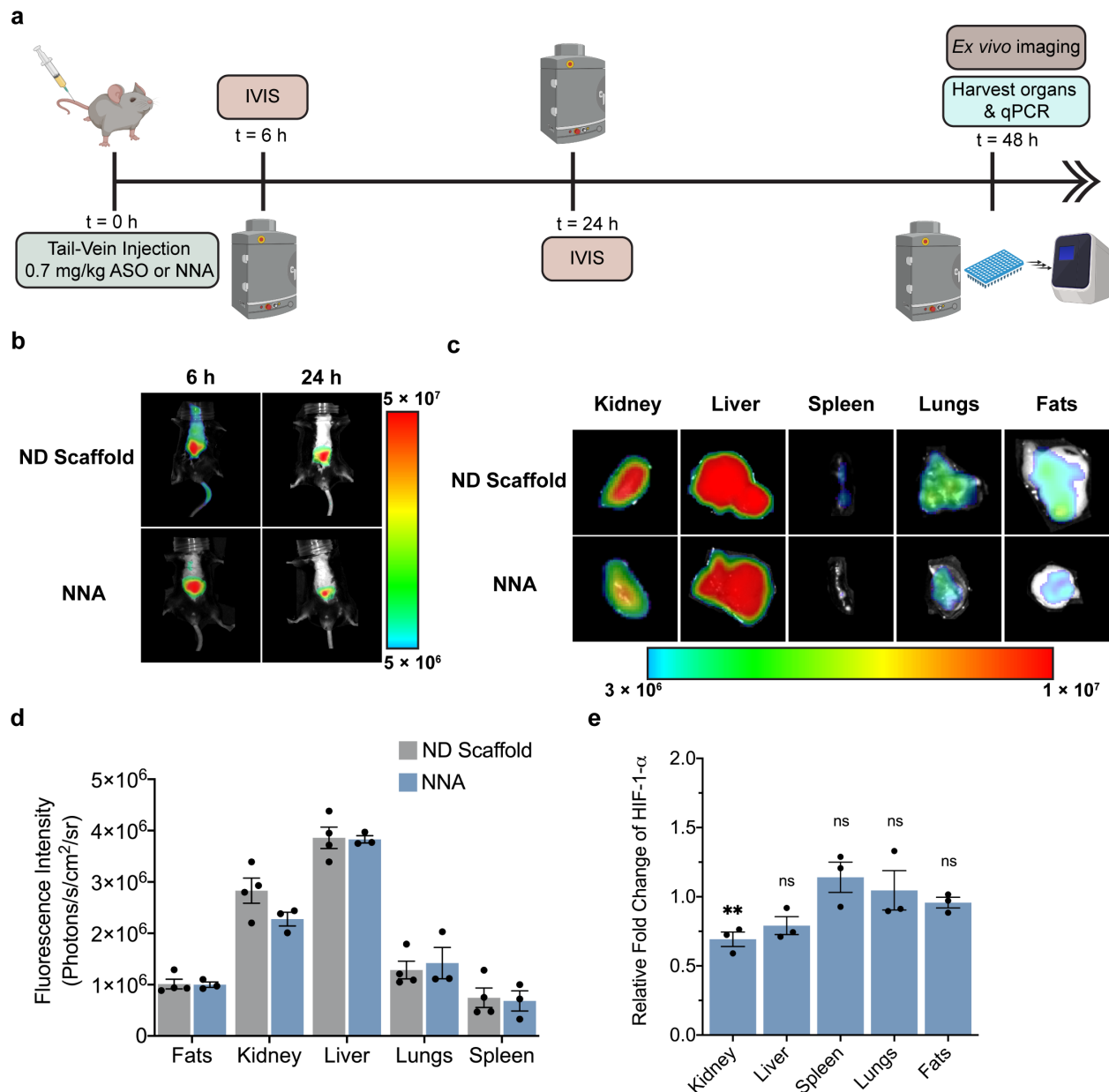


Figure 3.3.8: *In vivo* internalization and gene silencing efficacy of NNAs. **(a)** Timeline of *in vivo* imaging and qPCR experiments after injecting C57BL/6 mice with NNA, ND scaffold, and ASO only samples. Mice are injected with 0.7 mg/kg of the HIF-1- α ASO drug and sacrificed for ex vivo imaging and organ harvesting for RT-qPCR. **(b)** *In vivo*

fluorescence imaging for the uptake of the ND scaffold and NNA (ND 3) in C57BL/6 mice ($n = 4$). Representative images of mice taken at 6 h and 24 h post-injection. **(c)** *Ex vivo* fluorescence imaging of mice injected with ND scaffold (ND 3) and NNA (ND 3). Organ imaging was performed at 48 h post-injection on the kidneys, liver, spleen, lungs, and fats. **(d)** Plot quantifying the fluorescence intensity measured for the different organs of the mice from the *ex vivo* imaging. Increased uptake is correlated with increased fluorescence, and this was primarily observed in the kidneys and liver, followed by some observable uptake in the lungs. **(e)** Quantification of HIF-1- α levels in the harvested organs via qPCR after treatment with NNA (ND 3) for 48 h. The data was normalized against identical tissues treated with the ND. Error bars represent SEM. Each data point represents the result from one single animal normalized to animals treated with ND scaffold and ** $p < 0.01$.

3.4: Conclusion

In this study, we developed strategies to maximize DNA loading onto ND scaffolds. The innovation in this work pertains to two concepts. The first is the idea of conducting a one-pot reaction to covalently conjugate DNA to the peptides and phospholipids comprising the ND assembly using an efficient Michael addition. Secondly, we recognized the pitfalls associated with introduction of a thiol into the HDL mimetic peptide 22A and thus screened for Cys sites that minimally perturb the amphipathic character of the peptide and its capacity to self-assemble into ND in the presence of phospholipids. The optimal resulting NNA construct was assembled with one cysteine insertion on the C-terminus of the peptide, 90% DMPC phospholipid, and 10% Ptd-Thioethanol. DNA conjugation afforded an average of 30 copies of DNA covalently bound per NNA, and still retained sub-30 nm diameters and identical morphology to the parent ND scaffold. NNAs demonstrated a high degree of nuclease protection including DNase I. The NNA assembly did not alter the selective targeting properties of the scaffold, as uptake was discovered to be partially SRB1 dependent. Furthermore, we learned through sensitized-FRET that the ASO does separate from the scaffold within 24 h of incubation and uptake within cells. The NNA containing ASO modified to the C-terminus was identified as the most active *in vitro* as determined by qPCR and viability studies using HeLa, KPC, Lx-2 Stellate, and HepG2 cells. The NNA construct, owing in part to its smaller size and its specific targeting features, showed penetration into the necrotic core of a 3D H1299 cancer spheroid model which was correlated with greater levels of anti-sense activity compared to that of soluble ASOs. The NNAs are highly potent *in vivo* where we visualized

and quantified higher uptake in the liver and kidneys, correlating to the higher activity for reducing HIF-1- α mRNA levels using only a single low dose (0.7 mg/kg) of the ASO drug. Adopting the NNA platform may offer a compelling solution to bolstering oligonucleotide therapeutic efficacy in the clinic. Linking a single-stranded oligonucleotide can also enable us to build structured material assemblies of nucleic acid coated NDs, which can provide optimal dosing and further improve the therapeutic response associated with nucleic acid drugs. Overall, the versatile and advantageous platform presented by the NNA can enable us to precisely tune our scaffold to help significantly expand delivery efficiency and improve therapeutic outcomes for multiple drug targets across the board.

3.5: Materials and Methods

Lipids used to prepare ND scaffolds were purchased (**Table S3.6.2, Figure 3.3.1c**) from Avanti Polar Lipids (Alabaster, AL, USA), including DMPC, Ptd Thioethanol, and Cy5-PE. Oligonucleotides, including the DNAzyme and ASO, and HIF-1- α and 18S primers for RT-qPCR were custom-synthesized (**Table S3.6.3**) by Integrated DNA Technologies (Coralville, IA, USA). The modified and unmodified 22A ApoA1 mimetic peptides (**Figure 3.3.1b**) was purchased from Genscript® (Piscataway, NJ, USA) with N- and C- termini capped with acetylation and amidation respectively and TFA salts were removed. TEM samples were prepared on 400 mesh carbon-coated copper grids obtained from Electron Microscopy Sciences (CF400-Cu; Hatfield, PA, USA) and negative staining was performed with Nanoprobe's Nano-W™ (Yaphank, NY, USA). SMCC (22360), DNase I (EN0521), 6X Loading dye (R0611), and Bond-Breaker™ TCEP Solution (77720) were obtained from ThermoFisher Scientific (Waltham, MA, USA). Organic solvents used for SMCC coupling including anhydrous N,N-dimethylformamide (DMF, 227056) and N,N-diisopropylethylamine (DIPEA, 496219) were purchased from Sigma-Aldrich (St. Louis, MO, USA). DNA stock solutions, buffers, and other aqueous experiments used water from

Barnstead™ Nanopure Water System from ThermoFisher Scientific (Waltham, MA, USA) at a resistivity of 18.2 MΩ. Ethanol precipitation to separate unreacted SMCC from DNA utilized Koptec's USP-grade 200-proof ethanol from Decon Labs (V1001; King of Prussia, PA, USA) and sodium acetate (3 M, pH 5.2, molecular biology grade) from Millipore-Sigma (567422; Burlington, MA, USA) and purified using a hydrated P-2 gel from Bio-Rad (1504118; Hercules, CA, USA). Unreacted maleimide DNA from NNA, ASO-ND, and DNA-ND conjugation was removed using size exclusion with a MWCO: 50 kDa Amicon® Filter (UFC505024), Blocker of Lipid Transport-1 (SML0059), and Omnipur® Agarose (2120-OP) were purchased from EMD Millipore (Burlington, MA, USA). Quant-iT™ OliGreen™ ssDNA Reagent (O7582), nuclear DAPI stain: NucBlue™ Fixed Cell ReadyProbes™ (R37606), and SYBR™ Gold Nucleic Acid Gel Stain (S11494) were purchased from Invitrogen™ (Carlsbad, CA, USA). Cells were cultured in Dulbecco's Modification of Eagle's Medium with L-Glutamine (DMEM, 10-013-CM) and supplemented with Fetal Bovine Serum (FBS, 35-010-CV) and Penicillin-Streptomycin (30-002-CI) and were detached using Trypsin EDTA (25-053-CI) from Corning (Tewksbury, MA, USA). H1299 cells were cultured in RPMI-40 with L-Glutamine (11875093) acquired from Gibco (Waltham, MA, USA). Spheroids were initially seeded in ultra-low attachment microplates (07-201-680) and later implanted in Matrigel® Basement Membrane (356255 & 354234) and both items were purchased from Corning (Tewksbury, MA, USA). Spheroids for microscopy imaging were embedded in Matrigel on 35 mm Mattek plates with a No. 1.5 glass coverslip with a 14 mm diameter (P35G-1.5-14-C) purchased from Mattek corporation (Ashland, MA, USA). qPCR was performed with the following: RNeasy Mini Kit (74106), and QIAzol (79306) from Qiagen (Hilden, NRW, Germany), High-Capacity cDNA Reverse Transcription Kit from Applied Biosystems (4368814; Foster City, CA, USA), and PerfeCTa® SYBR® Green FastMix® Reaction Mix from QuantaBio (101414-278 [VWR]; Beverly, MA, USA). C57BL/6 mice were purchased from Jackson Laboratories (Bar Harbor, ME, USA). Prior to *in vivo* imaging, hair was removed using Nair™ (Ewing Township, NJ, USA) and mice

were anesthetized using isoflurane (DP7000) from Dechra Pharmaceuticals (Northwich, Cheshire, United Kingdom).

3.5.1: Synthesis and characterization of ND and NNA scaffolds

DMPC and thiol phospholipid stocks in chloroform were further diluted with chloroform in a 90:10 molar ratio. The mixture was evaporated using rotary evaporation and placed to dry for 30 min. For fluorescent experiments, Cy5-PE was doped in at a molar ratio of 0.15% or 1% as necessary. After 30 min. the lipid mixture was placed under a steady stream of nitrogen for 10 min. and the lipid film was hydrated with phosphate buffered saline (PBS, pH 7.4). The hydrated mixture was sonicated for 10 min. and subjected to 3 freeze-thaw cycles to ensure all the lipids were incorporated. SUVs were then prepared by passing the mixture 5 times through a 10 mL LIPEX® thermobarrel extruder (Evonik Industries, Essen, Germany) using a 80 nm polycarbonate filter. ApoA1 mimetic peptides (A, B, C, or D) was dissolved (2 mg) in nanopure water and combined with the SUVs. To assist in solubilization, the peptide-SUV mixture was vortexed for 15 seconds prior to performing three warm-cool cycles alternating between 55 °C and 4 °C for 15 min. The ND scaffolds (1 – 7) were stored for a maximum of 3 weeks at 4 °C.

3.5.2: Size and morphology characterization of NDs and NNAs

NDs and NNAs were measured as is (no further dilution) using DLS on a NanoPlus DLS Nano Particle Size and Zeta Potential Analyzer (Micromeritics Instrument Corporation, Norcross, GA, USA) instrument. Sample preparation for TEM was prepared as previously described.⁶² Briefly, 400-mesh copper grids were plasmon etched and a 5 µL drop of sample was placed on the grid for 30 seconds before gently blotting with a KimWipe and allowing the sample to dry for 2 min. One drop of Nano-W™ was applied to the dried grid for another 2 min. before blotting and drying. Samples were visualized using via TEM on a Hitachi HT7700 instrument (Chiyoda City, Tokyo, Japan) operating at 80 kV accelerating voltage. Some images were collected using the

JEOL-JEM TEM microscope (Peabody, MA, USA) operating at 120 kV accelerating voltage when available. TEM images were analyzed using Fiji.

3.5.3: Coupling maleimide-DNA onto the ND and NNA scaffolds

Maleimide-DNA was prepared as previously described.⁶² Briefly, SMCC (2 mg) was dissolved in DMF and DIPEA (0.2-fold v/v) and combined with amine-modified DNA (1 mM) for 1 h at room temperature. Unreacted SMCC was removed through ethanol precipitation and a P2 gel in a size exclusion column. The maleimide-DNA was purified via HPLC on an AdvanceBio Oligonucleotide (Santa Clara, CA, USA) column to remove any unreacted DNA. Samples were dried in a vacuum centrifuge overnight before coupling. Coupling was performed by reducing any disulfide linkages present in the peptide and/or lipid using 10-fold excess TCEP. After removing TCEP with an Amicon (MWCO: 50 kDa) column and calculating the ND concentration as described previously,⁶² purified SMCC-DNA was dissolved in PBS (pH 8.5) and combined in 12-fold excess with the ND and NNA scaffolds. The reaction was performed by gently agitating the mixture at 45 °C for 2 h before removing unbound DNA using centrifugal filtration with an Amicon size exclusion column (MWCO: 50 kDa) at 8500 RPM for 7 min. and washing 4 times (or until the supernatant displayed no 260 nm absorbance) in between with fresh PBS (pH 7.4) After the final wash, the solution was recovered (recovery volume 30 – 50 µL) and stored at 4 °C until further use.

3.5.4: Quantifying DNA density

DNA density was quantified using the commercially available OliGreen™ kit as described previously.⁶² In summary, a stock solution of DNA (12 µg/mL) that contained the same sequence strand as the sample was used to prepare a calibration curve at the following concentrations: 0.01, 0.1, 0.2, 0.5, 0.75, 1 µg/mL in 1× TE buffer. The diluted DNA calibration samples were supplemented with NDs and trypsin, to facilitate disassembly. ND and NNA samples were

prepared at the following concentrations: 0.2 nM, 0.4 nM, 0.6 nM, and 1.2 nM in 1× TE buffer with trypsin. Samples were heated to 85 °C for 10 min. before adding OliGreen™ and measuring the fluorescence intensity (Ex/Em = 485/528 nm) on a Synergy H1 Biotek Plate Reader (Winooski, VT, USA).

3.5.5: Bulk solution FRET measurements of DNA-NDs and NNAs

DNA (HIF-1- α ASO, **Table S3**) was fluorescently labeled with TYE563 and then conjugated to the ND scaffolds containing 1% Cy5 phospholipids. DNA-NDs and NNAs samples were prepared by diluting the stock solution to a final concentration containing 100 nM DNA. As controls, 100 nM DNA mixed with ND (but unconjugated), and 100 nM of DNA only were prepared in PBS. The donor fluorescence was measured on a fluorometer from Horiba Scientific (Edison, NJ, USA) by exciting the samples at $\lambda = 525$ nm and emission spectrum were collected with 20 accumulations and a 0.1 integration measured at $\lambda = 563$ nm. FRET efficiency was calculated as previously described.⁶²

3.5.6: Gel electrophoresis and serum degradation assay

A 1.5% agarose gel was prepared using in-gel staining with SYBR Gold (10,000× dilution). ND scaffolds were prepared with 0.15% Cy5 phospholipid to enable detection in the fluorescence readout. Samples (5 μ L) containing unbound DNA (control), DNA-NDs and NNAs (1 – 5), and unconjugated DNA mixed with ND were mixed with 6× loading dye (5 μ L) and samples (10 μ L) were loaded onto the gel and the gel was run at 85 V for 1.5 h on a Bio-Rad PowerPac Basic Electrophoresis Supply (Hercules, CA, USA) and visualized using an Amersham Typhoon laser scanner (Cytiva, Marlborough, MA, USA).

3.5.7: DNase I assay

NDs and NNAs containing DNAzyme along with soluble DNAzyme were diluted to 1 μ M (DNA concentration) using HEPES buffer (10 mM HEPES, 150 mM NaCl, pH 7.4) and combined

with 1 U of DNase I (or additional buffer for the control samples). The samples were incubated at 37 °C for 2 h. Thereafter, the DNase I was quenched using the supplied EDTA (5 mM) and inactivated at 65 °C for 10 mins, as per the accompanied protocol. The samples were transferred to a 96 well plate and combined with the DNAzyme substrate solution mix (10 mM HEPES, 150 mM NaCl, 10 μM DNAzyme substrate, 4 mM MgCl₂, pH = 7.4) and FAM fluorescence intensity was immediately monitored for 2.5 h using the plate reader. DNase I degradation was determined by comparing the fluorescence intensity at 2.5 h of the DNase I treated samples against the same sample that did not contain DNase I.

3.5.8: Cell and spheroid culture

HeLa cells (ATCC), HepG2 cells (ATCC), and KPC cells were cultured in DMEM containing L-glutamine with 10% FBS and 1% Penicillin (100 U/mL) - Streptomycin (100 mg/mL). LX-2 Human Hepatic Stellate cells (Sigma-Aldrich) followed similar culturing media except for using 2% FBS instead of 10% FBS. H1299 cells (ATCC) were cultured in RPMI-40 containing L-glutamine, 1% penicillin-streptomycin (1×), and 10% FBS. To form spheroids, 3000 cells were seeded in ultra-low attachment 96-well plates, centrifuged to allow cell clumping and placed in a cell culture incubator for 72 h to form cell-cell junctions. Subsequently, the spheroids were embedded in Matrigel® Basement Membrane in a Mattek plate or a 24-well tissue culture plate and placed in the incubator overnight. Treatment and incubation with NNA samples were performed the following day as the embedded spheroids began the invasion process. All cells and spheroids were maintained at 37 °C under a humidified CO₂ atmosphere (5%).

3.5.9: Confocal uptake studies on HeLa cells and spheroids

Uptake studies were performed as previously described.⁶² Briefly, HeLa cells were plated at a density of 1×10⁴ cells/well in a Nunc 96 well black optical plate (265300, ThermoFisher, Waltham, MA, USA) the day before experiment. The HIF-1-α ASO was labeled with a TYE563

fluorophore and the ND scaffolds were labeled with 1% Cy5 phospholipid. ASO-ND and NNA conjugates (100 nM) were incubated with cells for 3 h and 24 h and cells were fixed with 4% paraformaldehyde. Cells were washed three times using sterile 1× PBS (pH 7.4) and stained using DAPI. For each condition involved in spheroid imaging, a minimum of 5 spheroids were embedded in Matrigel® and treated with 100 nM of NNA (sample 3) or ASO only and incubated for 24 h. The following day, spheroids were rinsed with sterile 1× PBS three times and replaced with fresh PBS prior to imaging. Images were acquired on a Nikon Ti2 Eclipse confocal microscope (Minato City, Tokyo, Japan) using a 60× oil objective for cells (or a 20× objective for spheroids), Nikon Elements, perfect focus, and a C2 laser scanning system. Z-stacks were collected with a 0.2 µm step size for cells and a 5 µm step size for spheroids. Images were analyzed using ImageJ.

3.5.10: SRB1 mediated uptake of ASO-NDs and NNAs into cells and spheroids

HeLa cells were plated at a density of 6×10^4 cells/well in tissue-culture treated 12-well plates the day before experiment. A minimum of 5 spheroids were embedded in Matrigel® the day before experiment. Cells and spheroids were treated with 50 µM of BLT-1 in serum-free DMEM containing 0.1% BSA (v/v) for 1 h. Cells (15 nM ND scaffold, 15 nM ND) and spheroids (6 nM ND scaffold, 150 nM ASO) were treated with ASO-ND or NNA conjugates was added and incubated with cells for 2 h, prior to washing cells three times with 1× PBS before adding trypsin to dissociate cells from the surface or dissociate the spheroid into individual cells. The cells were collected and washed with 1× PBS two times before adding fresh PBS and collecting and analyzing the individual cells for flow cytometry assessment on a Beckman Coulter Cytoflex (Pasadena, CA, USA) to measure cell associated Cy5 fluorescence intensity. Fluorescence intensity was compared against cells not treated with BLT-1 containing ASO-ND or NNA conjugates. Histograms were prepared using FlowJo software (FlowJo LLC, Ashland, OR, USA).

3.5.11: Sensitized FRET measurements of ASO-NDs and NNAs in HeLa cells

HeLa cells were plated at a density of 1×10^4 cells/well in a Nunc 96 well black optical plate the day before experiment. The HIF-1- α ASO was labeled with a TYE563 fluorophore and the ND scaffolds were prepared with 1% Cy5 phospholipid. ASO-ND and NNA conjugates (100 nM) were incubated with cells for 3 h and 24 h and cells were fixed with 4% paraformaldehyde. Cells were washed three times using PBS (pH 7.4) and stained using DAPI before imaging on a Nikon Eclipse Ti microscope (Minato City, Tokyo, Japan) using a 100 \times oil objective, reflective interference contrast microscopy (RICM), Nikon Elements, perfect focus, epifluorescence illumination, and three-cubes for sensitized emission acquisition. The filter sets for the three cubes include donor channel TYE563 ex: ET545/25x, em: ET605/70m, dichroic (T565lpxr); acceptor channel Cy5, ex: ET620/60x, em: ET700/75m, dichroic (T660lpxr); and the FRET channel, TYE563 excitation ET550/40m, Cy5 emission S700/75m, dichroic (ZT647rdc) from Chroma Technology (Bellows Falls, VT, USA). The exposure was set at 200 ns for all channels. Control samples for FRET included ASO mixed with NNA (unconjugated), ASO only, and ND scaffold only. Image processing was performed using ImageJ and was modified as described in ref (¹⁴⁷). Image processing was optimized to identify the Cy5 acceptor fluorescence to calculate the FRET index (**Figure S3.6.4**). The correction factors were calculated as shown in (5) – (8) to correct for bleedthrough of donor emission into the acceptor channel and determine crosstalk. For (5), the values were determined with samples that contained donor only and no acceptor, whereas for (6) – (8), the values were determined using acceptor only, and no donor. These values were empirically calculated for our system using our specific microscope and filter setup. These factors were input into the FRET efficiency equation (9) to calculate the sensitized FRET of the fluorescence pixels associated with the ASO and ND in the cells. Note that 'A' represents the fluorescence intensity from the donor (ASO) channel, 'B' represents the fluorescence intensity from the FRET channel, and that 'C' represents the fluorescence intensity acquired from the acceptor (Cy5 ND).

$$\text{ASO Crosstalk} \quad \beta = \frac{B}{A} \quad (5)$$

$$\text{ND Cross-Excitation} \quad \gamma = \frac{B}{C} \quad (6)$$

$$\text{ASO Cross-Excitation Crosstalk} \quad \alpha = \frac{A}{C} \quad (7)$$

$$\text{FRET Crosstalk} \quad \delta = \frac{A}{B} \quad (8)$$

$$\text{FRET Efficiency} = \frac{B - (A \times \beta) - C \times (\gamma - \alpha \times \beta)}{C \times (1 - \beta \times \delta)} \quad (9)$$

3.5.12: RT-qPCR to assess HIF-1- α levels after *in vitro* treatment with ASO-ND or NNA using EZN2968

HeLa, KPC, LX-2 Human Hepatic Stellate, and HepG2 cells were plated at a density of 5×10^4 cells/well in tissue-culture treated 24-well plates the day before experiment. A minimum of 5 spheroids were embedded in Matrigel® and placed in 24 well plates, per condition, the day before experiment. ASO-NDs (1 – 2, 4) and NNAs (3, 5) conjugated specifically to the EZN2968 ASO (**Table S3.6.3**), EZN-2968 only, and scrambled EZN3088 on a ND scaffold were incubated with cells (100 nM) or spheroids (550 nM) for 24 h. Cells and spheroid were lysed using QIAzol and total RNA was collected as per the accompanied QIAGEN kit procedure. RNA was reverse transcribed to prepare cDNA in a T100 Thermal Cycler (Bio-Rad, Hercules, CA, USA). HIF-1- α mRNA levels were quantified using quantitative real time PCR (RT-qPCR) using PerfeCTa SYBR Green FastMix (using their accompanied fast 2-step cycling protocol) and 50 μ M custom primers (**Table S3**) and a Roche Lightcycler® 96 (Basel, Switzerland) instrument. Relative quantification of mRNA levels was determined using the $\Delta\Delta$ Ct method with 18S mRNA levels for an internal control.

3.5.13: MTT assay to assess cell viability

The MTT assay was performed as described previously.⁶² HeLa cells were plated at a density of 1×10^4 cells/well in a tissue-culture treated 96-well plates the day before experiment. The following day, the ASO-NDs and NNA samples (1 – 5) containing EZN2968, soluble EZN2968

ASO, and scrambled ASO-ND (EZN3088) were incubated with cells for 24 h. The cells were rinsed with fresh media prior to adding a 1:1 ratio (total volume = 100 μ L) of phenol red-free and serum-free DMEM and pre-warmed (37 $^{\circ}$ C) MTT solution. Cells were placed in the incubator at 37 $^{\circ}$ C for 3 hours before adding 150 μ L of pre-warmed MTT solvent. Subsequently, the plate was gently agitated for 15 min. before measuring the optical density at 590 nm on a plate reader. Cell viability was assessed by determining the cytotoxicity and normalizing to the untreated control set at 100%.

3.5.14: Mice acclimatization and tail-vein injection of ND scaffold, NNAs, and ASO

10-week-old male C57BL/6 mice were allowed to acclimate to their environment for 72 h before injection. Prior to injection, mice were exposed to a heat lamp for 10 min. to dilate the tail vein. Mice were restrained using an acrylic mouse restrainer and the injection site was cleaned with 70% ethanol. ASO and NNA were injected via the tail-vein into the mice at 0.7 mg/kg and the ND scaffold for the NNA conjugate was injected at 5 μ M to best account for the concentration of the discs in the NNAs.

3.5.15: Murine *in vivo* and *ex vivo* fluorescence imaging

Mouse underside hair was removed using NairTM and mice were anesthetized in a Fluovac induction chamber from Harvard Apparatus (Holliston, MA, USA) using 5% isoflurane and gradually reduced to 2% for 5 mins until they had fallen asleep. At 6 h and 24 h post sample injection the mice were imaged using the Ami HTX-Optical imager from Spectral Instruments Imaging (Tucson, AZ, USA) using exposure: 10 seconds, 1.5 cm object height, low binning (2), 2.0 FStop, 50% excitation power, ex: 640 nm, em: 710 nm. At 48 h post sample injection, the mice were sacrificed using CO₂ and the spleen, lungs, kidneys, liver, and fat were harvested and imaged using the optical imager.

3.5.16: RNA isolation and RT-qPCR quantification of HIF-1- α from mice organs

Harvested organs from sacrificed mice were collected and rapidly purified after *ex vivo* imaging to reduce RNase exposure. Each 20 mg section of an organ was supplemented with a metal bead homogenizer and 350 μ L QIAZOL and added to a BeadBug 6 Microtube Homogenizer from Benchmark Scientific (Sayreville, NJ, USA). Samples were homogenized for 3 cycles at 2500 RPM for 30 seconds to facilitate the release of RNA from tissue and samples were further purified using a benchtop mini centrifuge at 6000 RPM for 1 min to remove extracellular matrix, plasma, and blood components in the supernatant. Supernatant was diluted with 6-fold volume of QIAZOL and samples were purified by adding 1:1 (v/v) of QIAZOL and 70% ethanol to each sample. Organs were homogenized using a syringe to facilitate the release of RNA and the samples were purified to isolate RNA using the QIAGEN RNA extraction kit. RNA isolation, cDNA synthesis, and RT-qPCR were performed as described above.

3.6: Supplementary Information

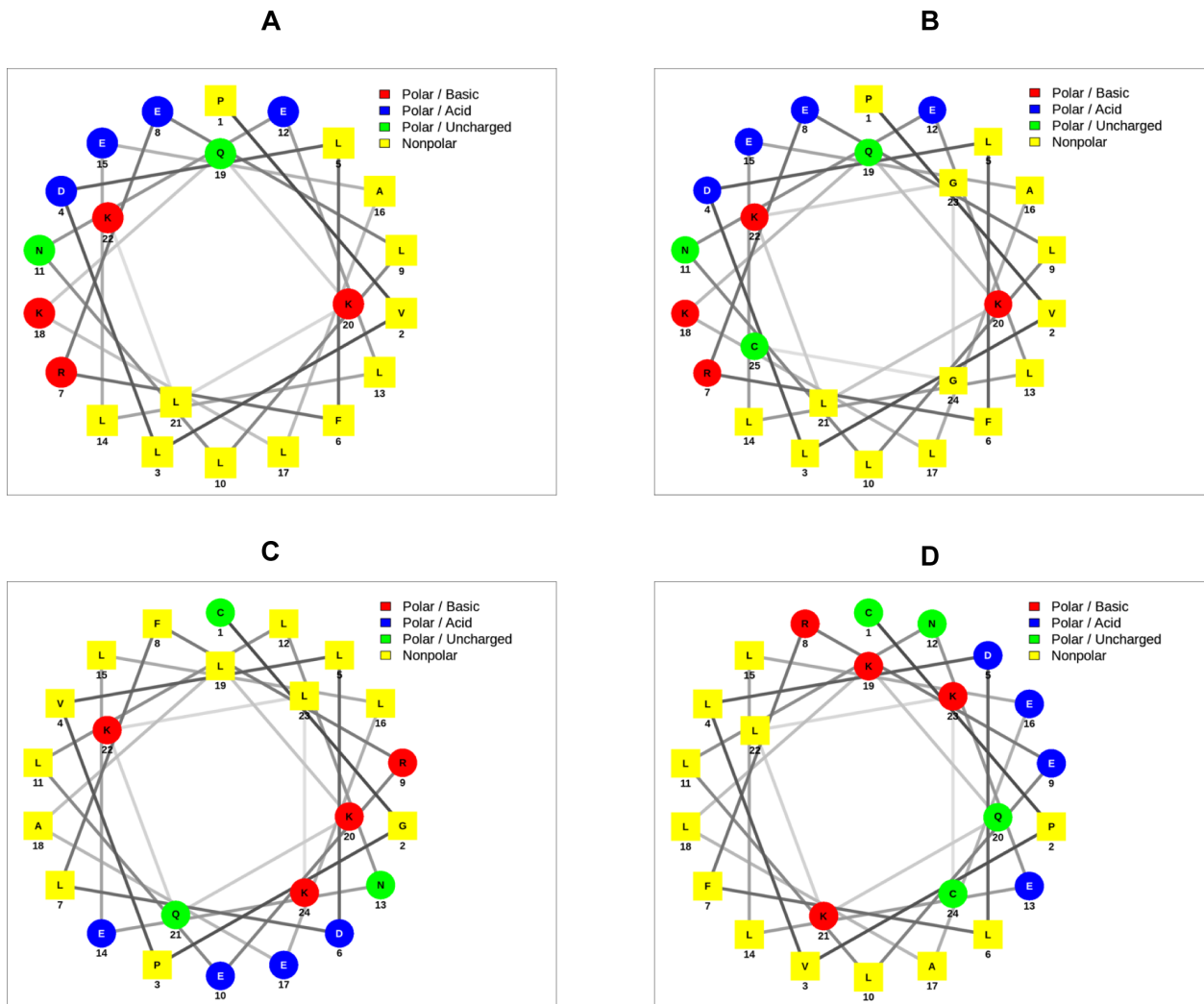


Figure 3.6.1: Helical wheel diagrams for the 22A peptide (A) and the peptides with cysteine insertion(s) for peptides B – D. Peptide sequences are listed in **Figure 3.3.1c**. Helical wheels were generated using NetWheels.

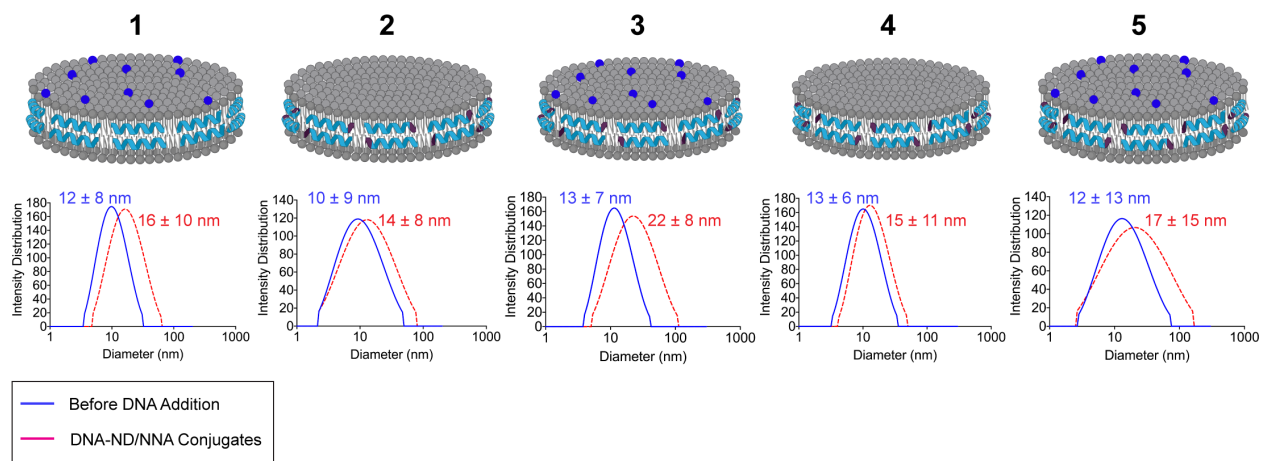


Figure 3.6.2: DLS measurements of ASO-NDs and NNAs before (blue) and after DNA addition (red). DNA coupling onto the ND scaffold shows a shift in the hydrodynamic radius. Size distribution profile is a representative graph of a typical sample ($n = 3$ independent experiments containing the ND scaffold and/or the ASO-ND or NNA conjugate).

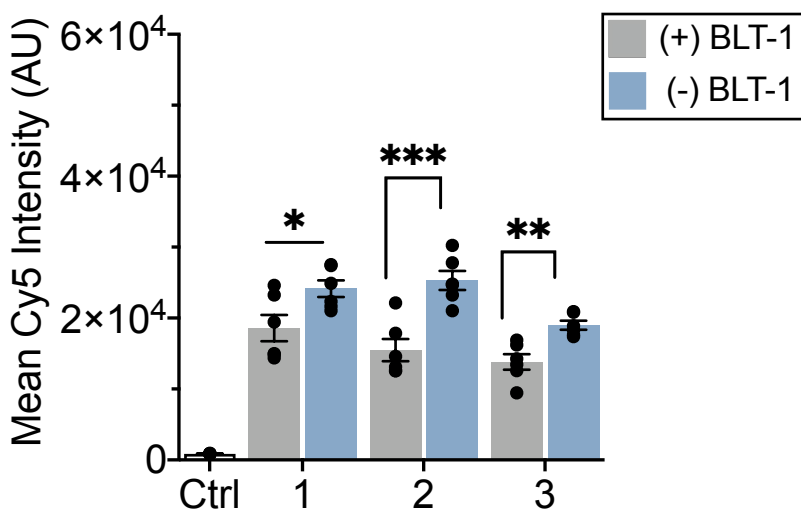


Figure 3.6.3: Raw intensity values from the uptake of DNA-NDs and NNAs with and without BLT-1 treatment. HeLa cells were incubated with 50 μ M of BLT-1 to inhibit SRB1, prior to treating cells with 15 nM of the ND scaffold (400 nM ASO) for NDs 1 – 3 for 2 h before collecting cells and measuring the cell-associated Cy5 fluorescence intensity using flow cytometry. There are significant differences in uptake for each sample group treated with BLT-1 (denoted as '+') when compared to the same group with no BLT-1 treatment (denoted as '-'). This data concludes that SRB1 plays a significant role in the internalization of ASO-NDs and NNAs into cells, but other mechanisms are also involved in the uptake. Each data point represents the average from $n = 6$ independent replicates and * $p < 0.05$, ** $p < 0.01$, *** $p < 0.001$. Error bars represent SEM.

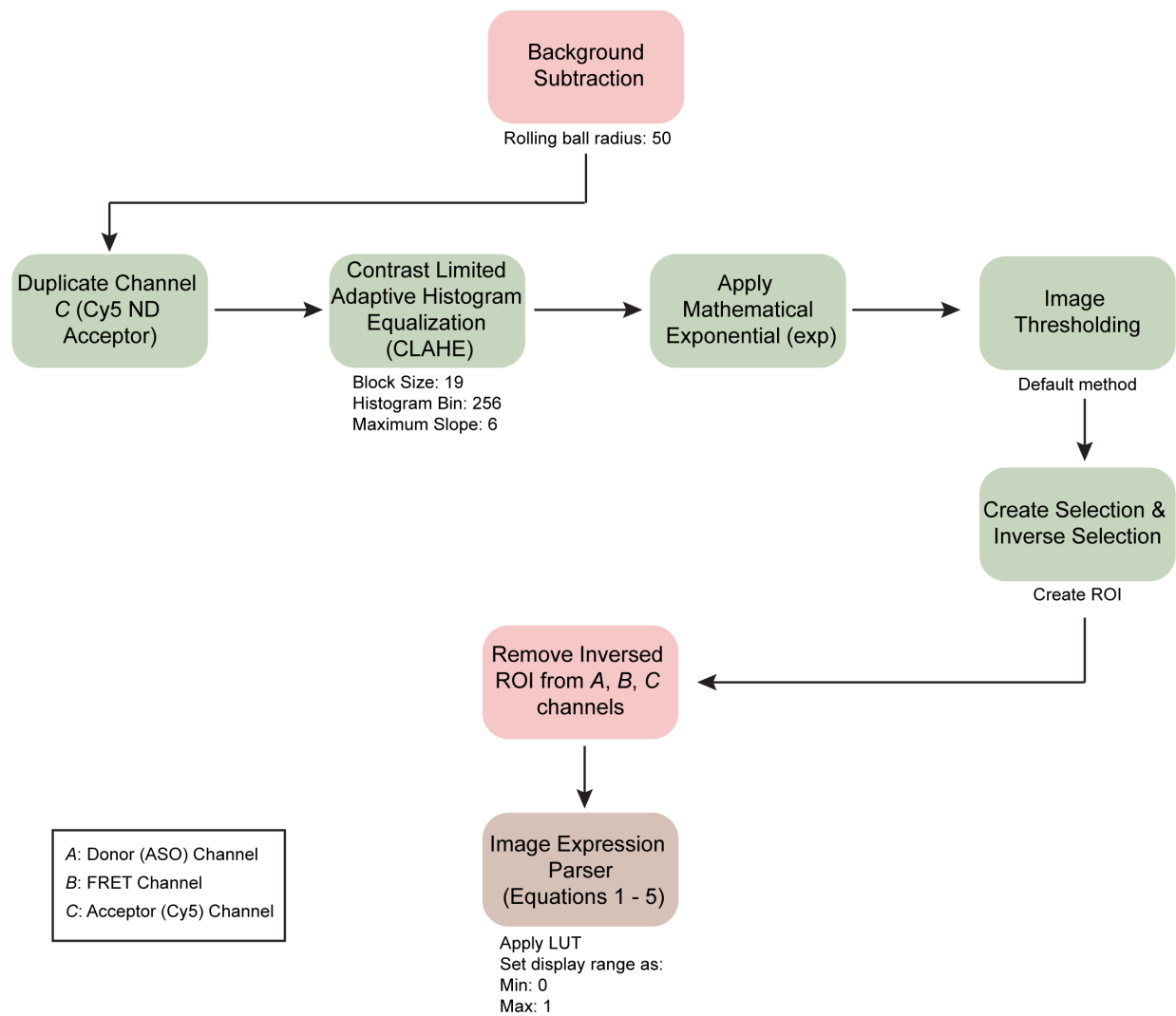


Figure 3.6.4: Flowchart detailing the image processing performed to determine FRET index (efficiency) using the Fiji/ImageJ software. Images were background subtracted using a rolling ball radius of 50 pixels for all three channels: the donor (A), FRET (B), and acceptor (C). The Cy5 acceptor (C) channel was duplicated and underwent an equalization process using the CLAHE function. CLAHE amplified “real” signal and did not amplify any signal that was contributed by noise. After CLAHE, the background on the duplicated channel was further minimized by applying a mathematical exponential before creating a threshold that enabled us to create ROI selections of regions of Cy5 intensity. Subsequently, an inverse function was applied to allow for removal of the noisy signal in the original image channels (same channel that was previously duplicated (C) and the donor (A) and FRET (B) channels included). The image was finally parsed using (5) (see **3.6.5: Materials and Methods**) to calculate the sensitized FRET. An LUT with a restricted image range: **0** minimum display value – **1** maximum display value.

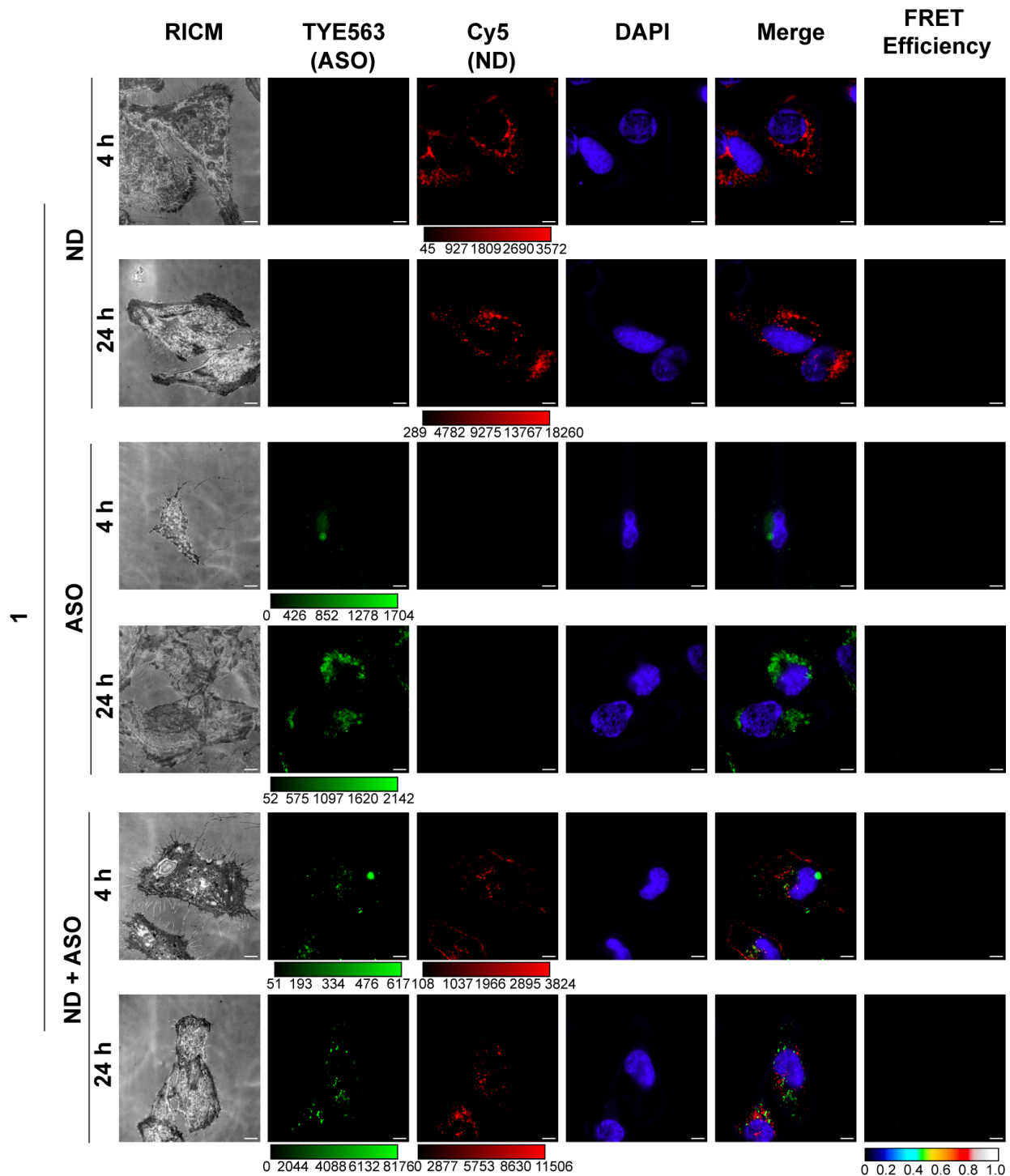


Figure 3.6.5: Representative epifluorescence images that detail the FRET efficiencies measured for the control samples for sample 1: ASO only, ND only, and ND + ASO mix but unconjugated. HeLa cells were incubated with 100 nM ASO for the ASO only and ND + ASO samples, and 6 nM of ND to best compensate for the concentration of ND in the ASO-ND for the ND only and ND + ASO sample. As described in **Figure 5**, panel includes a RICM image, and fluorescence intensity of TYE563 (ASO) and Cy5 (1% Cy5 phospholipid for NNA). Images were taken at 4 h and 24 h and cells were fixed and stained with DAPI prior to imaging with a 100× oil objective using a FRET cube. FRET images were generated from thresholding the acceptor channel (ND) and parsing the pixels and correcting for bleedthrough from donor and acceptor (ASO). Calibration bar represents FRET efficiency (set between 0 – 1.0.) As expected, the unconjugated controls do not have any FRET efficiency. Scale bar: 5 μm.

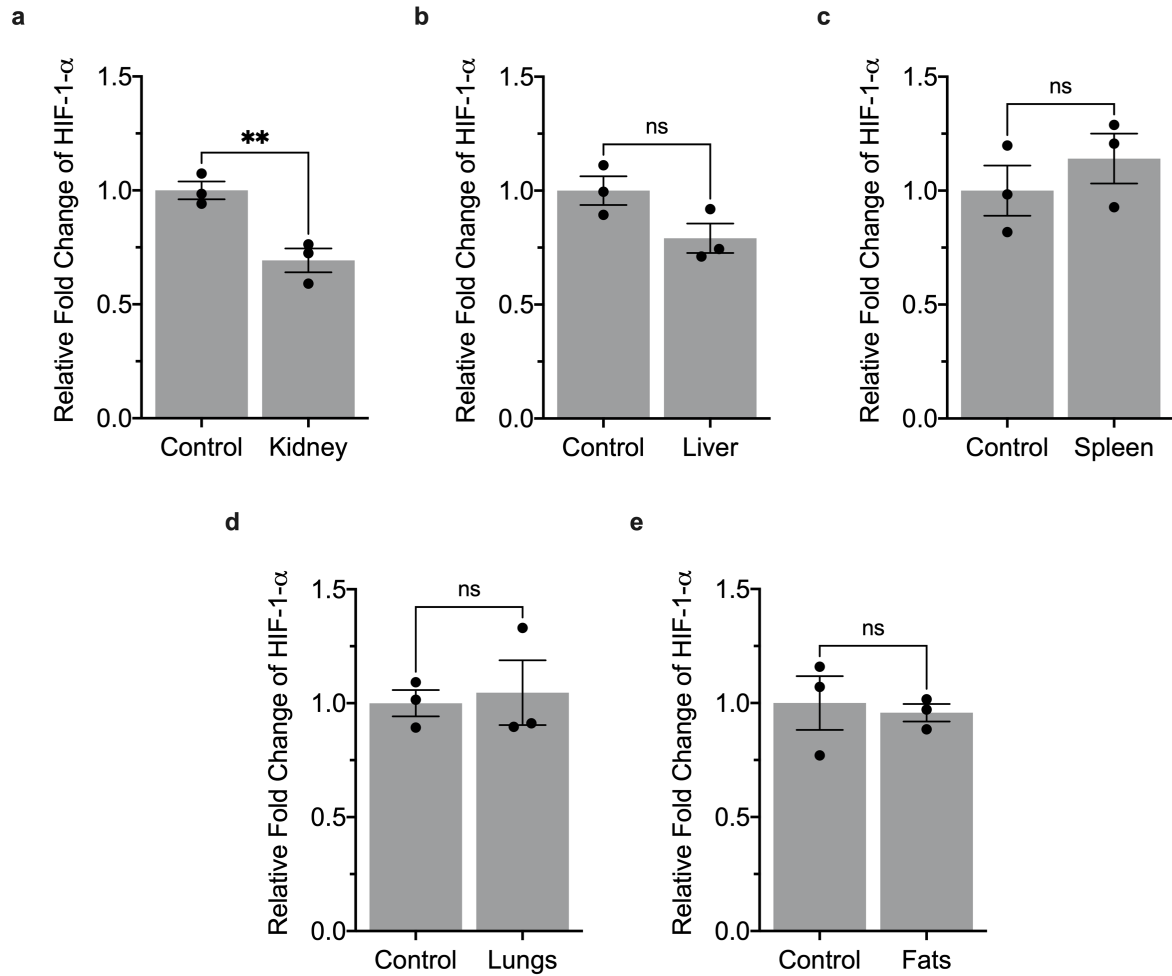


Figure 3.6.6: Quantification of HIF-1- α levels in harvested organs. ND scaffold containing no nucleic acid or NNAs (ND 3) bearing the EZN2968 anti-HIF-1- α ASO were injected into C57BL/6 mice via tail-vein injection. The ASO drug concentration was at 0.7 mg/kg whereas the ND scaffold control was injected at a concentration of 5 μ M to account for the ND concentration in the NNA sample. Mice were sacrificed at 48 h post injection and organs were harvested for RNA isolation. Plots represent the quantified HIF-1- α levels for the (a) kidney, (b) liver, (c) spleen, (d) lungs, and (e) fats; transcript levels were normalized to identical tissues that were subject to the ND scaffold treatment without ASO as a control. Each data point represents the result from one single animal. Error bars represent SEM and * $p < 0.01$.

Table S3.6.1: Comparing the amount of DNA copies occupied per micron on gold vs. the different ND scaffolds.

Scaffold	Average DNA Copies	Surface Area (nm ²)	Footprint (DNA/μm ²)
AuNP (13 nm)	100	531	188
1	10	385	26
2	16	289	55
3	26	388	67
4	10	349	29
5	35	392	89

Table S3.6.2: Lipids used for preparing the ND scaffolds (1 – 7). Catalog number is in reference to the product as available on Avanti Polar Lipids website.

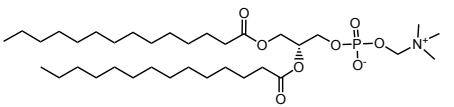
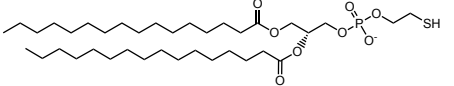
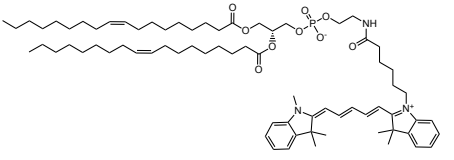
Lipid	Catalog Number	Structure
DMPC (1,2-dimyristoyl-sn-glycero-3-phosphocholine)	850345	
Thiol lipid (1,2-dipalmitoyl-sn-glycero-3-phosphothioethanol)	870160	
Cy5 lipid [1,2-dioleoyl-sn-glycero-3-phosphoethanolamine-N-(cyanine 5)]	810335	

Table S3.6.3: Nucleic acid sequences used for the NNA study. Sequences include the catalytic DNAzyme, HIF-1- α ASO sequence, scrambled ASO sequence, and primers.

“+” = LNA Modification “*” = PS Modification “3AmMo” = 3' Amino Modifier. “rX” = RNA base

“5TYE563” = 5' TYE™ 563 Fluorophore

“56-FAM” = 5' 6-Fluorescein fluorophore

“3IABkFQ” = 3' Iowa Black® Hole FQ Quencher

ID	Sequence (5' → 3')
Catalytic Dz	ATT CCT TAA AGG CTA GCT ACA ACG ATT CTT GGC TTT
Catalytic Dz-Amine	ATT CCT TAA AGG CTA GCT ACA ACG ATT CTT GGC TTT /3AmMO/
Catalytic Dz Substrate	/56-FAM/ GCC AAG AArG rUTT AAG GAA T /3IABkFQ/
HIF-1- α ASO (EZN2968)	+T*+G*+G* C*A*A* G*C*A* T*C*C* +T*+G*+T* A
HIF-1- α ASO-Amine	+T*+G*+G* C*A*A* G*C*A* T*C*C* +T*+G*+T* A /3AmMO/
TYE563-HIF-1- α ASO-Amine	/5TYE563/ T*G*G* C*A* A* G*C*A* T*C*C* T*G*T* A /3AmMO/
Scrambled HIF-1- α ASO-Amine (EZN3088-Amine)	+C*+G*+T* C*A*G* T*A*T* G*C*G* +A*+A*+T* C /3AmMO/
HIF-1- α Forward Primer	TAT GAG CCA GAA GAA CTT TTA GGC
HIF-1- α Reverse Primer	CAC CTC TTT TGG CAA GCA TCC TG
18S Forward Primer	AGG AAT TGA CGG AAG GGC ACC A
18S Reverse Primer	GTG CAG CCC CGG ACA TCT AAG

Chapter 4

Recap and Future Directions

4.1: Summary and Conclusions

Nucleic acid therapeutics have slowly gained increased momentum because of the slow increase in the amount of FDA approvals in the past half-decade. However, there are a large percentage of drugs that are in trials, and most will not be able to translate for clinical use. While protein-based therapies treat the forefront of limiting mRNA translation, DNA-based and RNA-based therapies can specifically interact with its target to remove the underlying cause for disease. Nucleic acids drugs can also be customized to develop specific RNAi and ASO therapies based on abnormalities in an individual's genome. Despite its immense potential, delivering this biomacromolecule is not without its challenges and is the primary reason for failure in clinical trials. Accordingly, any improvements for delivery technology are of paramount importance and will significantly escalate the adoption of oligonucleotide drugs in the clinic.

HDL mimics are an especially advantageous scaffold for delivery because of their structural resemblance to nascent HDL. HDL mimicking particles are also functionally similar to native HDL, more specifically regarding cargo delivery without facing endosomal barriers, and the transport of endogenous nucleic acids. Therefore, using HDL mimics such as a ND, is in fact a clever "trojan horse" strategy to efficiently deliver nucleic acids. The work presented in these studies details the engineering and design of the next generation of HDL mimicking nanoparticles devised to enhance the delivery of nucleic acid therapeutics. We focused on developing a covalent (hence more stable) coupling strategy to conjugate and simultaneously boost and maximize nucleic acid density. We discovered that this strategy did not impede the functional capacity of the oligonucleotide and linking it onto the disc boosts its nuclease protection and overall delivery efficiency. Next, we took our coupling strategy a step forward to create a densely packed discoidal structure, termed the NNA, through a DNA-peptide conjugation in conjunction with the surface conjugation. This boosted DNA density to an average of 30 DNA/ND scaffold, the highest we have observed thus far. The dense conjugation on the NNA did not alter the morphology or its gene silencing capacity in any manner and we found that the NNAs can diffuse

into the hypoxic core of cancer spheroids and reduce HIF-1- α mRNA transcript levels. Furthermore, NNAs are able to lower HIF-1- α gene expression in the kidneys in an *in vivo* mice model using a 5-fold lower dose than what was originally recommended from the pharmaceutical company that developed this ASO.

The structure and activity of NNAs presented in this body of work is pharmacologically relevant as it can significantly reduce the amount and frequency of drug that needs to be delivered with each dosage. The future using ND scaffolds and NNAs is limitless, and we look forward to watching this field rapidly expand and develop into a commonly used and everyone's preferred drug delivery system.

4.2.: Future Directions

As mentioned above, there is endless potential for HDL mimics and how they can be adopted for every therapeutic intervention. The ND scaffold, while small, offers a unique and heavily underutilized space to facilitate simultaneous delivery of multiple cargo. The underlying cause of any disease is the dysfunction of multiple biochemical and signaling pathways. Typical standard of care requires administering the therapies at separate intervals to minimize adverse reactions, which is not very effective for many people. Furthermore, most people will be on medication continuously for long periods of time, triggering malfunction of other pathways and wreaking general havoc on the immune system – the body's most important defense system. Combining NNA nucleic acid therapy with small molecule therapy can continue to lower side effects, required dosage, treatment intervals, and improve the efficacy of the overall treatment. Developing such "holistic" ND systems that appropriately partitions the drugs should be the next step towards treating disease.

The nucleic acid landscape is currently expanding because of newer chemical improvements from decades of research is finally helping to slowly boost the FDA approvals. In addition to therapeutics, DNA and RNA can have multiple utilities. DNA can be used as a material

to facilitate construction of 3D assemblies, and because of the unique space of the ND scaffold, one can carefully utilize the space to develop spatially tunable nano-sized 3D structures (e.g. a rod built from multiple NDs) constructed from DNA (as a DDS). Higher-ordered structures can be used to tune the precise delivery and directional transport of a nucleic acid drug, further amplify the drug response, and significantly reduce the amount and frequency of a drug dose to a patient. Increased hierarchy can also improve the resiliency (mechanical and chemical strength) of the DDS, but careful attention must be placed on identifying an optimal ratio that modulates the dimensional aspect against any immune response.

There are many uses for a ND scaffold from studying membrane proteins, to boosting RCT for cardiac disease, to using it as a diagnostic to detect any abnormal profile in the endogenous cargo, and to of course, using it as a drug delivery vehicle. The current clinical trial of CSL-112 and the efforts of multiple research laboratories will no doubt propel the future of ND therapeutics. We look forward to watching the advancements using HDL mimicks in the years to come.

References

1. Kulkarni, J. A.; Witzigmann, D.; Thomson, S. B.; Chen, S.; Leavitt, B. R.; Cullis, P. R.; van der Meel, R., The current landscape of nucleic acid therapeutics. *Nature Nanotechnology* **2021**, *16* (6), 630-643.
2. Crooke, S. T.; Vickers, T. A.; Liang, X.-h., Phosphorothioate modified oligonucleotide–protein interactions. *Nucleic Acids Research* **2020**, *48* (10), 5235-5253.
3. Zaslavsky, A.; Adams, M.; Cao, X.; Yamaguchi, A.; Henderson, J.; Busch-Østergren, P.; Udager, A.; Pitchiaya, S.; Tournet, B.; Kasputis, T.; Church, S. J.; Lee, S. K.; Ohl, S.; Patel, S.; Morgan, T. M.; Alva, A.; Wakefield, T. W.; Reichert, Z.; Holinstat, M.; Palapattu, G. S., Antisense oligonucleotides and nucleic acids generate hypersensitive platelets. *Thrombosis Research* **2021**, *200*, 64-71.
4. Roberts, T. C.; Langer, R.; Wood, M. J. A., Advances in oligonucleotide drug delivery. *Nature Reviews Drug Discovery* **2020**, *19* (10), 673-694.
5. Papini, E.; Tavano, R.; Mancin, F., Opsonins and Dysopsonins of Nanoparticles: Facts, Concepts, and Methodological Guidelines. *Frontiers in Immunology* **2020**, *11*.
6. Anselmo, A. C.; Mitragotri, S., A Review of Clinical Translation of Inorganic Nanoparticles. *The AAPS Journal* **2015**, *17* (5), 1041-1054.
7. Tenchov, R.; Bird, R.; Curtze, A. E.; Zhou, Q., Lipid Nanoparticles—From Liposomes to mRNA Vaccine Delivery, a Landscape of Research Diversity and Advancement. *ACS Nano* **2021**, *15* (11), 16982-17015.
8. Hou, X.; Zaks, T.; Langer, R.; Dong, Y., Lipid nanoparticles for mRNA delivery. *Nature Reviews Materials* **2021**, *6* (12), 1078-1094.
9. Mitchell, M. J.; Billingsley, M. M.; Haley, R. M.; Wechsler, M. E.; Peppas, N. A.; Langer, R., Engineering precision nanoparticles for drug delivery. *Nature Reviews Drug Discovery* **2021**, *20* (2), 101-124.
10. Dowdy, S. F., Overcoming cellular barriers for RNA therapeutics. *Nature Biotechnology* **2017**, *35* (3), 222-229.
11. Bricarello, D. A.; Smilowitz, J. T.; Zivkovic, A. M.; German, J. B.; Parikh, A. N., Reconstituted Lipoprotein: A Versatile Class of Biologically-Inspired Nanostructures. *ACS Nano* **2011**, *5* (1), 42-57.
12. Mineo, C.; Deguchi, H.; Griffin, J. H.; Shaul, P. W., Endothelial and Antithrombotic Actions of HDL. *Circulation Research* **2006**, *98* (11), 1352-1364.
13. Griffin, J. H.; Kojima, K.; Banka, C. L.; Curtiss, L. K.; Fernández, J. A., High-density lipoprotein enhancement of anticoagulant activities of plasma protein S and activated protein C. *J Clin Invest* **1999**, *103* (2), 219-27.
14. Brites, F.; Martin, M.; Guillas, I.; Kontush, A., Antioxidative activity of high-density lipoprotein (HDL): Mechanistic insights into potential clinical benefit. *BBA Clinical* **2017**, *8*, 66-77.
15. Kontush, A., HDL-mediated mechanisms of protection in cardiovascular disease. *Cardiovascular Research* **2014**, *103* (3), 341-349.
16. Barter, P. J.; Nicholls, S.; Rye, K.-A.; Anantharamaiah, G. M.; Navab, M.; Fogelman, A. M., Antiinflammatory Properties of HDL. *Circulation Research* **2004**, *95* (8), 764-772.
17. Yang, K.; Wang, J.; Xiang, H.; Ding, P.; Wu, T.; Ji, G., LCAT- targeted therapies: Progress, failures and future. *Biomedicine & Pharmacotherapy* **2022**, *147*, 112677.
18. Nazir, S.; Jankowski, V.; Bender, G.; Zewinger, S.; Rye, K.-A.; van der Vorst, E. P. C., Interaction between high-density lipoproteins and inflammation: Function matters more than concentration! *Advanced Drug Delivery Reviews* **2020**, *159*, 94-119.
19. Miller, N. E., HDL metabolism and its role in lipid transport. *European Heart Journal* **1990**, *11* (suppl_H), 1-3.

20. Heinecke, J. W., The protein cargo of HDL: Implications for vascular wall biology and therapeutics. *Journal of Clinical Lipidology* **2010**, *4* (5), 371-375.
21. Vickers, K. C.; Remaley, A. T., HDL and cholesterol: life after the divorce? *Journal of Lipid Research* **2014**, *55* (1), 4-12.
22. Vickers, K. C.; Palmisano, B. T.; Shoucri, B. M.; Shamburek, R. D.; Remaley, A. T., MicroRNAs are transported in plasma and delivered to recipient cells by high-density lipoproteins. *Nature Cell Biology* **2011**, *13* (4), 423-433.
23. Wolfrum, C.; Shi, S.; Jayaprakash, K. N.; Jayaraman, M.; Wang, G.; Pandey, R. K.; Rajeev, K. G.; Nakayama, T.; Charrise, K.; Ndungo, E. M.; Zimmermann, T.; Koteliensky, V.; Manoharan, M.; Stoffel, M., Mechanisms and optimization of in vivo delivery of lipophilic siRNAs. *Nature Biotechnology* **2007**, *25* (10), 1149-1157.
24. Tang, J.; Kuai, R.; Yuan, W.; Drake, L.; Moon, J. J.; Schwendeman, A., Effect of size and pegylation of liposomes and peptide-based synthetic lipoproteins on tumor targeting. *Nanomedicine: Nanotechnology, Biology and Medicine* **2017**, *13* (6), 1869-1878.
25. Kuai, R.; Li, D.; Chen, Y. E.; Moon, J. J.; Schwendeman, A., High-Density Lipoproteins: Nature's Multifunctional Nanoparticles. *ACS Nano* **2016**, *10* (3), 3015-3041.
26. Gao, X.; Yuan, S.; Jayaraman, S.; Gursky, O., Differential Stability of High-density Lipoprotein Subclasses: Effects of Particle Size and Protein Composition. *Journal of Molecular Biology* **2009**, *387* (3), 628-638.
27. Zannis, V. I.; Chroni, A.; Krieger, M., Role of apoA-I, ABCA1, LCAT, and SR-BI in the biogenesis of HDL. *Journal of Molecular Medicine* **2006**, *84* (4), 276-294.
28. Mooberry, L. K.; Sabnis, N. A.; Panchoo, M.; Nagarajan, B.; Lacko, A. G., Targeting the SR-B1 Receptor as a Gateway for Cancer Therapy and Imaging. *Frontiers in Pharmacology* **2016**, *7*.
29. Scheetz, L. M.; Yu, M.; Li, D.; Castro, M. G.; Moon, J. J.; Schwendeman, A., Synthetic HDL Nanoparticles Delivering Docetaxel and CpG for Chemoimmunotherapy of Colon Adenocarcinoma. *International Journal of Molecular Sciences* **2020**, *21* (5).
30. Phillips, M. C., New insights into the determination of HDL structure by apolipoproteins: Thematic Review Series: High Density Lipoprotein Structure, Function, and Metabolism. *Journal of Lipid Research* **2013**, *54* (8), 2034-2048.
31. Segrest, J. P.; Garber, D. W.; Brouillette, C. G.; Harvey, S. C.; Anantharamaiah, G. M., The Amphipathic α Helix: A Multifunctional Structural Motif in Plasma Apolipoproteins. In *Advances in Protein Chemistry*, Anfinsen, C. B.; Edsall, J. T.; Richards, F. M.; Eisenberg, D. S., Eds. Academic Press: 1994; Vol. 45, pp 303-369.
32. Palgunachari, M. N.; Mishra, V. K.; Lund-Katz, S.; Phillips, M. C.; Adeyeye, S. O.; Alluri, S.; Anantharamaiah, G. M.; Segrest, J. P., Only the Two End Helices of Eight Tandem Amphipathic Helical Domains of Human Apo A-I Have Significant Lipid Affinity. *Arteriosclerosis, Thrombosis, and Vascular Biology* **1996**, *16* (2), 328-338.
33. Saito, H.; Lund-Katz, S.; Phillips, M. C., Contributions of domain structure and lipid interaction to the functionality of exchangeable human apolipoproteins. *Progress in Lipid Research* **2004**, *43* (4), 350-380.
34. Leman, L. J.; Maryanoff, B. E.; Ghadiri, M. R., Molecules That Mimic Apolipoprotein A-I: Potential Agents for Treating Atherosclerosis. *Journal of Medicinal Chemistry* **2014**, *57* (6), 2169-2196.
35. Lund-Katz, S.; Phillips, M. C., High density lipoprotein structure-function and role in reverse cholesterol transport. *Subcell Biochem* **2010**, *51*, 183-227.
36. Sundaram, M.; Yao, Z., Intrahepatic Role of Exchangeable Apolipoproteins in Lipoprotein Assembly and Secretion. *Arteriosclerosis, Thrombosis, and Vascular Biology* **2012**, *32* (5), 1073-1078.
37. Frank, P. G.; Marcel, Y. L., Apolipoprotein A-I: structure-function relationships. *Journal of Lipid Research* **2000**, *41* (6), 853-872.

38. Anantharamaiah, G. M.; Jones, J. L.; Brouillette, C. G.; Schmidt, C. F.; Chung, B. H.; Hughes, T. A.; Bhowan, A. S.; Segrest, J. P., Studies of synthetic peptide analogs of the amphipathic helix. Structure of complexes with dimyristoyl phosphatidylcholine. *Journal of Biological Chemistry* **1985**, *260* (18), 10248-10255.
39. Leman, L. J., The potential of apolipoprotein mimetic peptides in the treatment of atherosclerosis. *Clinical Lipidology* **2015**, *10* (3), 215-217.
40. Ikeda, Y.; Taira, T.; Sakai, K.; Sakai, H.; Shigeri, Y.; Imura, T., Lipid Nanodisc Formation using Pxt-5 Peptide Isolated from Amphibian (*Xenopus tropicalis*) Skin, and its Altered Form, Modify-Pxt-5. *Journal of Oleo Science* **2018**, *67* (8), 1035-1041.
41. Marqusee, S.; Baldwin, R. L., Helix stabilization by Glu...Lys+ salt bridges in short peptides of de novo design. *Proceedings of the National Academy of Sciences* **1987**, *84* (24), 8898-8902.
42. Meriwether, D.; Imaizumi, S.; Grijalva, V.; Hough, G.; Vakili, L.; Anantharamaiah, G. M.; Farias-Eisner, R.; Navab, M.; Fogelman, A. M.; Reddy, S. T.; Shechter, I., Enhancement by LDL of transfer of L-4F and oxidized lipids to HDL in C57BL/6J mice and human plasma. *Journal of Lipid Research* **2011**, *52* (10), 1795-1809.
43. Manthei, K. A.; Patra, D.; Wilson, C. J.; Fawaz, M. V.; Piersimoni, L.; Shenkar, J. C.; Yuan, W.; Andrews, P. C.; Engen, J. R.; Schwendeman, A.; Ohi, M. D.; Tesmer, J. J. G., Structural analysis of lecithin:cholesterol acyltransferase bound to high density lipoprotein particles. *Communications Biology* **2020**, *3* (1), 28.
44. Anantharamaiah, G. M.; Mishra, V. K.; Garber, D. W.; Datta, G.; Handattu, S. P.; Palgunachari, M. N.; Chaddha, M.; Navab, M.; Reddy, S. T.; Segrest, J. P.; Fogelman, A. M., Structural requirements for antioxidative and anti-inflammatory properties of apolipoprotein A-I mimetic peptides. *J Lipid Res* **2007**, *48* (9), 1915-23.
45. Wolska, A.; Reimund, M.; Sviridov, D. O.; Amar, M. J.; Remaley, A. T., Apolipoprotein Mimetic Peptides: Potential New Therapies for Cardiovascular Diseases. *Cells* **2021**, *10* (3).
46. Getz, G. S.; Wool, G. D.; Reardon, C. A., Biological properties of apolipoprotein a-I mimetic peptides. *Curr Atheroscler Rep* **2010**, *12* (2), 96-104.
47. Navab, M.; Anantharamaiah, G. M.; Hama, S.; Garber, D. W.; Chaddha, M.; Hough, G.; Lallone, R.; Fogelman, A. M., Oral Administration of an Apo A-I Mimetic Peptide Synthesized From D-Amino Acids Dramatically Reduces Atherosclerosis in Mice Independent of Plasma Cholesterol. *Circulation* **2002**, *105* (3), 290-292.
48. Di Bartolo, B. A.; Nicholls, S. J.; Bao, S.; Rye, K.-A.; Heather, A. K.; Barter, P. J.; Bursill, C., The apolipoprotein A-I mimetic peptide ETC-642 exhibits anti-inflammatory properties that are comparable to high density lipoproteins. *Atherosclerosis* **2011**, *217* (2), 395-400.
49. Sethi, A. A.; Stonik, J. A.; Thomas, F.; Demosky, S. J.; Amar, M.; Neufeld, E.; Brewer, H. B.; Davidson, W. S.; D'Souza, W.; Sviridov, D.; Remaley, A. T., Asymmetry in the lipid affinity of bihelical amphipathic peptides. A structural determinant for the specificity of ABCA1-dependent cholesterol efflux by peptides. *J Biol Chem* **2008**, *283* (47), 32273-82.
50. Kariyazono, H.; Nadai, R.; Miyajima, R.; Takechi-Haraya, Y.; Baba, T.; Shigenaga, A.; Okuhira, K.; Otaka, A.; Saito, H., Formation of stable nanodiscs by bihelical apolipoprotein A-I mimetic peptide. *Journal of Peptide Science* **2016**, *22* (2), 116-122.
51. Zhao, Y.; Imura, T.; Leman, L. J.; Curtiss, L. K.; Maryanoff, B. E.; Ghadiri, M. R., Mimicry of High-Density Lipoprotein: Functional Peptide-Lipid Nanoparticles Based on Multivalent Peptide Constructs. *Journal of the American Chemical Society* **2013**, *135* (36), 13414-13424.
52. Imura, T.; Tsukui, Y.; Taira, T.; Aburai, K.; Sakai, K.; Sakai, H.; Abe, M.; Kitamoto, D., Surfactant-like Properties of an Amphiphilic α -Helical Peptide Leading to Lipid Nanodisc Formation. *Langmuir* **2014**, *30* (16), 4752-4759.
53. Islam, R. M.; Pourmousa, M.; Sviridov, D.; Gordon, S. M.; Neufeld, E. B.; Freeman, L. A.; Perrin, B. S.; Pastor, R. W.; Remaley, A. T., Structural properties of apolipoprotein A-I mimetic peptides that promote ABCA1-dependent cholesterol efflux. *Scientific Reports* **2018**, *8* (1), 2956.

54. Gou, S.; Wang, L.; Zhong, C.; Chen, X.; Ouyang, X.; Li, B.; Bao, G.; Liu, H.; Zhang, Y.; Ni, J., A novel apoA-I mimetic peptide suppresses atherosclerosis by promoting physiological HDL function in apoE(-/-) mice. *Br J Pharmacol* **2020**, *177* (20), 4627-4644.
55. Bloedon, L. T.; Dunbar, R.; Duffy, D.; Pinell-Salles, P.; Norris, R.; DeGroot, B. J.; Movva, R.; Navab, M.; Fogelman, A. M.; Rader, D. J., Safety, pharmacokinetics, and pharmacodynamics of oral apoA-I mimetic peptide D-4F in high-risk cardiovascular patients. *J Lipid Res* **2008**, *49* (6), 1344-52.
56. Khan, M., Lalwani, ND, Drake SL, Crockatt JG, Dasseux JL., Single-dose intravenous infusion of ETC-642, a 22-Mer ApoA-I analogue and phospholipids complex, elevates HDL-C in atherosclerosis patients. *Circulation* **2003**, *108*, 563-564.
57. Kuai, R.; Ochyl, L. J.; Bahjat, K. S.; Schwendeman, A.; Moon, J. J., Designer vaccine nanodiscs for personalized cancer immunotherapy. *Nature Materials* **2017**, *16* (4), 489-496.
58. Patel, H.; Ding, B.; Ernst, K.; Shen, L.; Yuan, W.; Tang, J.; Drake, L. R.; Kang, J.; Li, Y.; Chen, Z.; Schwendeman, A., Characterization of apolipoprotein A-I peptide phospholipid interaction and its effect on HDL nanodisc assembly. *Int J Nanomedicine* **2019**, *14*, 3069-3086.
59. Wan, C. P.; Chiu, M. H.; Wu, X.; Lee, S. K.; Prenner, E. J.; Weers, P. M., Apolipoprotein-induced conversion of phosphatidylcholine bilayer vesicles into nanodisks. *Biochim Biophys Acta* **2011**, *1808* (3), 606-13.
60. Fawaz, M. V.; Kim, S. Y.; Li, D.; Ming, R.; Xia, Z.; Olsen, K.; Pogozeva, I. D.; Tesmer, J. J. G.; Schwendeman, A., Phospholipid Component Defines Pharmacokinetic and Pharmacodynamic Properties of Synthetic High-Density Lipoproteins. *J Pharmacol Exp Ther* **2020**, *372* (2), 193-204.
61. Larsen, A. N.; Sørensen, K. K.; Johansen, N. T.; Martel, A.; Kirkensgaard, J. J. K.; Jensen, K. J.; Arleth, L.; Midtgaard, S. R., Dimeric peptides with three different linkers self-assemble with phospholipids to form peptide nanodiscs that stabilize membrane proteins. *Soft Matter* **2016**, *12* (27), 5937-5949.
62. Sharma, R.; Dong, Y.; Hu, Y.; Ma, V. P.-Y.; Salaita, K., Gene Regulation Using Nanodiscs Modified with HIF-1- α Antisense Oligonucleotides. *Bioconjugate Chemistry* **2022**, *33* (2), 279-293.
63. Bedi, S.; Morris, J.; Shah, A.; Hart, R. C.; Jerome, W. G.; Aller, S. G.; Tang, C.; Vaisar, T.; Bornfeldt, K. E.; Segrest, J. P.; Heinecke, J. W.; Davidson, W. S., Conformational flexibility of apolipoprotein A-I amino- and carboxy-termini is necessary for lipid binding but not cholesterol efflux. *Journal of Lipid Research* **2022**, *63* (3), 100168.
64. McConathy, W. J.; Nair, M. P.; Paranjape, S.; Mooberry, L.; Lacko, A. G., Evaluation of synthetic/reconstituted high-density lipoproteins as delivery vehicles for paclitaxel. *Anti-Cancer Drugs* **2008**, *19* (2).
65. Krause, B. R.; Remaley, A. T., Reconstituted HDL for the acute treatment of acute coronary syndrome. *Current Opinion in Lipidology* **2013**, *24* (6).
66. Michael Gibson, C.; Korjian, S.; Tricoci, P.; Daaboul, Y.; Yee, M.; Jain, P.; Alexander, J. H.; Steg, P. G.; Lincoff, A. M.; Kastelein, J. J. P.; Mehran, R.; D'Andrea, D. M.; Deckelbaum, L. I.; Merkely, B.; Zarebinski, M.; Ophuis, T. O.; Harrington, R. A., Safety and Tolerability of CSL112, a Reconstituted, Infusible, Plasma-Derived Apolipoprotein A-I, After Acute Myocardial Infarction. *Circulation* **2016**, *134* (24), 1918-1930.
67. Sei, Y. J.; Ahn, J.; Kim, T.; Shin, E.; Santiago-Lopez, A. J.; Jang, S. S.; Jeon, N. L.; Jang, Y. C.; Kim, Y., Detecting the functional complexities between high-density lipoprotein mimetics. *Biomaterials* **2018**, *170*, 58-69.
68. Kim, Y.; Fay, F.; Cormode, D. P.; Sanchez-Gaytan, B. L.; Tang, J.; Hennessy, E. J.; Ma, M.; Moore, K.; Farokhzad, O. C.; Fisher, E. A.; Mulder, W. J. M.; Langer, R.; Fayad, Z. A., Single Step Reconstitution of Multifunctional High-Density Lipoprotein-Derived Nanomaterials Using Microfluidics. *ACS Nano* **2013**, *7* (11), 9975-9983.

69. McMahon, K. M.; Mutharasan, R. K.; Tripathy, S.; Veliceasa, D.; Bobeica, M.; Shumaker, D. K.; Luthi, A. J.; Helfand, B. T.; Ardehali, H.; Mirkin, C. A.; Volpert, O.; Thaxton, C. S., Biomimetic High Density Lipoprotein Nanoparticles For Nucleic Acid Delivery. *Nano Letters* **2011**, *11* (3), 1208-1214.
70. Henrich, S. E.; Hong, B. J.; Rink, J. S.; Nguyen, S. T.; Thaxton, C. S., Supramolecular Assembly of High-Density Lipoprotein Mimetic Nanoparticles Using Lipid-Conjugated Core Scaffolds. *Journal of the American Chemical Society* **2019**, *141* (25), 9753-9757.
71. Agarwal, R.; Singh, V.; Journey, P.; Shi, L.; Sreenivasan, S. V.; Roy, K., Mammalian cells preferentially internalize hydrogel nanodiscs over nanorods and use shape-specific uptake mechanisms. *Proceedings of the National Academy of Sciences* **2013**, *110* (43), 17247.
72. Canfrán-Duque, A.; Lin, C.-S.; Goedeke, L.; Suárez, Y.; Fernández-Hernando, C., Micro-RNAs and High-Density Lipoprotein Metabolism. *Arteriosclerosis, Thrombosis, and Vascular Biology* **2016**, *36* (6), 1076-1084.
73. Feng, H.; Wang, M.; Wu, C.; Yu, J.; Wang, D.; Ma, J.; Han, J., High scavenger receptor class B type I expression is related to tumor aggressiveness and poor prognosis in lung adenocarcinoma: A STROBE compliant article. *Medicine (Baltimore)* **2018**, *97* (13), e0203.
74. Yang, M.; Jin, H.; Chen, J.; Ding, L.; Ng, K. K.; Lin, Q.; Lovell, J. F.; Zhang, Z.; Zheng, G., Efficient Cytosolic Delivery of siRNA Using HDL-Mimicking Nanoparticles. *Small* **2011**, *7* (5), 568-573.
75. Tahmasbi Rad, A.; Malik, S.; Yang, L.; Oberoi-Khanuja, T. K.; Nieh, M.-P.; Bahal, R., A universal discoidal nanoplatform for the intracellular delivery of PNAs. *Nanoscale* **2019**, *11* (26), 12517-12529.
76. Wang, J.; Calvert, A. E.; Kaplan, N.; McMahon, K. M.; Yang, W.; Lu, K. Q.; Peng, H.; Thaxton, C. S.; Lavker, R. M., HDL Nanoparticles Have Wound Healing and Anti-Inflammatory Properties and Can Topically Deliver miRNAs. *Advanced Therapeutics* **2020**, *3* (12), 2000138.
77. Lacko, A. G.; Sabnis, N. A.; Nagarajan, B.; McConathy, W. J., HDL as a drug and nucleic acid delivery vehicle. *Frontiers in Pharmacology* **2015**, *6*.
78. Cruz, W.; Huang, H.; Barber, B.; Pasini, E.; Ding, L.; Zheng, G.; Chen, J.; Bhat, M., Lipoprotein-Like Nanoparticle Carrying Small Interfering RNA Against Spalt-Like Transcription Factor 4 Effectively Targets Hepatocellular Carcinoma Cells and Decreases Tumor Burden. *Hepatology Communications* **2020**, *4* (5), 769-782.
79. Lin, Q.; Chen, J.; Jin, H.; Ng, K. K.; Yang, M.; Cao, W.; Ding, L.; Zhang, Z.; Zheng, G., Efficient systemic delivery of siRNA by using high-density lipoprotein-mimicking peptide lipid nanoparticles. *Nanomedicine* **2012**, *7* (12), 1813-1825.
80. Zhang, Z.; Cao, W.; Jin, H.; Lovell, J. F.; Yang, M.; Ding, L.; Chen, J.; Corbin, I.; Luo, Q.; Zheng, G., Biomimetic Nanocarrier for Direct Cytosolic Drug Delivery. *Angewandte Chemie International Edition* **2009**, *48* (48), 9171-9175.
81. Ghosh, M.; Ren, G.; Simonsen, J. B.; Ryan, R. O., Cationic lipid nanodisks as an siRNA delivery vehicle. *Biochem Cell Biol* **2014**, *92* (3), 200-205.
82. Pfeiffer, I.; Höök, F., Bivalent Cholesterol-Based Coupling of Oligonucleotides to Lipid Membrane Assemblies. *Journal of the American Chemical Society* **2004**, *126* (33), 10224-10225.
83. Nakayama, T.; Butler, J. S.; Sehgal, A.; Severgnini, M.; Racie, T.; Sharman, J.; Ding, F.; Morskaya, S. S.; Brodsky, J.; Tchangov, L.; Kosovrasti, V.; Meys, M.; Nechev, L.; Wang, G.; Peng, C. G.; Fang, Y.; Maier, M.; Rajeev, K. G.; Li, R.; Hettlinger, J.; Barros, S.; Clausen, V.; Zhang, X.; Wang, Q.; Hutabarat, R.; Dokholyan, N. V.; Wolfrum, C.; Manoharan, M.; Kotelianski, V.; Stoffel, M.; Sah, D. W. Y., Harnessing a Physiologic Mechanism for siRNA Delivery With Mimetic Lipoprotein Particles. *Molecular Therapy* **2012**, *20* (8), 1582-1589.
84. Shahzad, M. M. K.; Mangala, L. S.; Han, H. D.; Lu, C.; Bottsford-Miller, J.; Nishimura, M.; Mora, E. M.; Lee, J.-W.; Stone, R. L.; Pecot, C. V.; Thanappapasr, D.; Roh, J.-W.; Gaur, P.; Nair, M. P.; Park, Y.-Y.; Sabnis, N.; Deavers, M. T.; Lee, J.-S.; Ellis, L. M.; Lopez-Berestein, G.; McConathy, W. J.; Prokai, L.; Lacko, A. G.; Sood, A. K., Targeted Delivery of Small

Interfering RNA Using Reconstituted High-Density Lipoprotein Nanoparticles. *Neoplasia* **2011**, *13* (4), 309-IN8.

85. Chen, Q.; Guan, G.; Deng, F.; Yang, D.; Wu, P.; Kang, S.; Sun, R.; Wang, X.; Zhou, D.; Dai, W.; Wang, X.; Zhang, H.; He, B.; Chen, D.; Zhang, Q., Anisotropic active ligandations in siRNA-Loaded hybrid nanodiscs lead to distinct carcinostatic outcomes by regulating nano-bio interactions. *Biomaterials* **2020**, *251*, 120008.

86. Kuwahara, H.; Nishina, K.; Yoshida, K.; Nishina, T.; Yamamoto, M.; Saito, Y.; Piao, W.; Yoshida, M.; Mizusawa, H.; Yokota, T., Efficient *In Vivo* Delivery of siRNA Into Brain Capillary Endothelial Cells Along With Endogenous Lipoprotein. *Molecular Therapy* **2011**, *19* (12), 2213-2221.

87. Uno, Y.; Piao, W.; Miyata, K.; Nishina, K.; Mizusawa, H.; Yokota, T., High-Density Lipoprotein Facilitates *In Vivo* Delivery of α -Tocopherol-Conjugated Short-Interfering RNA to the Brain. *Human Gene Therapy* **2010**, *22* (6), 711-719.

88. Ding, Y.; Wang, W.; Feng, M.; Wang, Y.; Zhou, J.; Ding, X.; Zhou, X.; Liu, C.; Wang, R.; Zhang, Q., A biomimetic nanovector-mediated targeted cholesterol-conjugated siRNA delivery for tumor gene therapy. *Biomaterials* **2012**, *33* (34), 8893-8905.

89. Ding, Y.; Wang, Y.; Zhou, J.; Gu, X.; Wang, W.; Liu, C.; Bao, X.; Wang, C.; Li, Y.; Zhang, Q., Direct cytosolic siRNA delivery by reconstituted high density lipoprotein for target-specific therapy of tumor angiogenesis. *Biomaterials* **2014**, *35* (25), 7214-7227.

90. McMahon, K. M.; Plebanek, M. P.; Thaxton, C. S., Properties of Native High-Density Lipoproteins Inspire Synthesis of Actively Targeted *In Vivo* siRNA Delivery Vehicles. *Advanced Functional Materials* **2016**, *26* (43), 7824-7835.

91. Tripathy, S.; Vinokour, E.; McMahon, K. M.; Volpert, O. V.; Thaxton, C. S., High Density Lipoprotein Nanoparticles Deliver RNAi to Endothelial Cells to Inhibit Angiogenesis. *Part Part Syst Charact* **2014**, *31* (11), 1141-1150.

92. Somasuntharam, I.; Yehl, K.; Carroll, S. L.; Maxwell, J. T.; Martinez, M. D.; Che, P.-L.; Brown, M. E.; Salaita, K.; Davis, M. E., Knockdown of TNF- α by DNAzyme gold nanoparticles as an anti-inflammatory therapy for myocardial infarction. *Biomaterials* **2016**, *83*, 12-22.

93. Xiong, H.; Veedu, R. N.; Diermeier, S. D., Recent Advances in Oligonucleotide Therapeutics in Oncology. *International Journal of Molecular Sciences* **2021**, *22* (7).

94. Gagliardi, M.; Ashizawa, A. T., The Challenges and Strategies of Antisense Oligonucleotide Drug Delivery. *Biomedicines* **2021**, *9* (4).

95. Deleavey, Glen F.; Damha, Masad J., Designing Chemically Modified Oligonucleotides for Targeted Gene Silencing. *Chemistry & Biology* **2012**, *19* (8), 937-954.

96. Juliano, R. L., The delivery of therapeutic oligonucleotides. *Nucleic Acids Research* **2016**, *44* (14), 6518-6548.

97. Khvorova, A.; Watts, J. K., The chemical evolution of oligonucleotide therapies of clinical utility. *Nature Biotechnology* **2017**, *35* (3), 238-248.

98. Beltinger, C.; Saragovi, H. U.; Smith, R. M.; LeSauter, L.; Shah, N.; DeDionisio, L.; Christensen, L.; Raible, A.; Jarett, L.; Gewirtz, A. M., Binding, uptake, and intracellular trafficking of phosphorothioate-modified oligodeoxynucleotides. *The Journal of Clinical Investigation* **1995**, *95* (4), 1814-1823.

99. Eckstein, F., Phosphorothioates, Essential Components of Therapeutic Oligonucleotides. *Nucleic Acid Therapeutics* **2014**, *24* (6), 374-387.

100. Pei, D.; Buyanova, M., Overcoming Endosomal Entrapment in Drug Delivery. *Bioconjugate Chemistry* **2019**, *30* (2), 273-283.

101. Frazier, K. S., Antisense Oligonucleotide Therapies: The Promise and the Challenges from a Toxicologic Pathologist's Perspective. *Toxicologic Pathology* **2014**, *43* (1), 78-89.

102. Cutler, J. I.; Auyeung, E.; Mirkin, C. A., Spherical Nucleic Acids. *Journal of the American Chemical Society* **2012**, *134* (3), 1376-1391.

103. Yehl, K.; Joshi, J. P.; Greene, B. L.; Dyer, R. B.; Nahta, R.; Salaita, K., Catalytic Deoxyribozyme-Modified Nanoparticles for RNAi-Independent Gene Regulation. *ACS Nano* **2012**, *6* (10), 9150-9157.
104. Liu, B.; Wu, P.; Huang, Z.; Ma, L.; Liu, J., Bromide as a Robust Backfiller on Gold for Precise Control of DNA Conformation and High Stability of Spherical Nucleic Acids. *Journal of the American Chemical Society* **2018**, *140* (13), 4499-4502.
105. Mokhtarzadeh, A.; Vahidnezhad, H.; Youssefian, L.; Mosafer, J.; Baradaran, B.; Uitto, J., Applications of Spherical Nucleic Acid Nanoparticles as Delivery Systems. *Trends in Molecular Medicine* **2019**, *25* (12), 1066-1079.
106. McMahon, K. M.; Thaxton, C. S., High-density lipoproteins for the systemic delivery of short interfering RNA. *Expert Opinion on Drug Delivery* **2014**, *11* (2), 231-247.
107. Kadiyala, P.; Li, D.; Nuñez, F. M.; Altshuler, D.; Doherty, R.; Kuai, R.; Yu, M.; Kamran, N.; Edwards, M.; Moon, J. J.; Lowenstein, P. R.; Castro, M. G.; Schwendeman, A., High-Density Lipoprotein-Mimicking Nanodiscs for Chemo-immunotherapy against Glioblastoma Multiforme. *ACS Nano* **2019**, *13* (2), 1365-1384.
108. Meckes, B.; Banga, R. J.; Nguyen, S. T.; Mirkin, C. A., Enhancing the Stability and Immunomodulatory Activity of Liposomal Spherical Nucleic Acids through Lipid-Tail DNA Modifications. *Small* **2018**, *14* (5), 1702909.
109. Jeong, W.; Rapisarda, A.; Park, S. R.; Kinders, R. J.; Chen, A.; Melillo, G.; Turkbey, B.; Steinberg, S. M.; Choyke, P.; Doroshow, J. H.; Kummar, S., Pilot trial of EZN-2968, an antisense oligonucleotide inhibitor of hypoxia-inducible factor-1 alpha (HIF-1 α), in patients with refractory solid tumors. *Cancer Chemother Pharmacol* **2014**, *73* (2), 343-348.
110. Patnaik, A.; Chiorean, E. G.; Tolcher, A.; Papadopoulos, K.; Beeram, M.; Kee, D.; Waddell, M.; Gilles, E.; Buchbinder, A., EZN-2968, a novel hypoxia-inducible factor-1 α (HIF-1 α) messenger ribonucleic acid (mRNA) antagonist: Results of a phase I, pharmacokinetic (PK), dose-escalation study of daily administration in patients (pts) with advanced malignancies. *Journal of Clinical Oncology* **2009**, *27* (15_suppl), 2564-2564.
111. Denisov, I. G.; Sligar, S. G., Nanodiscs for structural and functional studies of membrane proteins. *Nature Structural & Molecular Biology* **2016**, *23* (6), 481-486.
112. Siuda, I.; Tieleman, D. P., Molecular Models of Nanodiscs. *Journal of Chemical Theory and Computation* **2015**, *11* (10), 4923-4932.
113. Bengtson, T.; Holm, V. L.; Kjølbye, L. R.; Midtgaard, S. R.; Johansen, N. T.; Tesei, G.; Bottaro, S.; Schiøtt, B.; Arleth, L.; Lindorff-Larsen, K., Structure and dynamics of a nanodisc by integrating NMR, SAXS and SANS experiments with molecular dynamics simulations. *Elife* **2020**, *9*, e56518.
114. Zhang, L.; Song, J.; Cavigiolio, G.; Ishida, B. Y.; Zhang, S.; Kane, J. P.; Weisgraber, K. H.; Oda, M. N.; Rye, K.-A.; Pownall, H. J.; Ren, G., Morphology and structure of lipoproteins revealed by an optimized negative-staining protocol of electron microscopy [S]. *Journal of Lipid Research* **2011**, *52* (1), 175-184.
115. Santoro, S. W.; Joyce, G. F., A general purpose RNA-cleaving DNA enzyme. *Proceedings of the National Academy of Sciences* **1997**, *94* (9), 4262.
116. Wang, Y.; Nguyen, K.; Spitale, R. C.; Chaput, J. C., A biologically stable DNAzyme that efficiently silences gene expression in cells. *Nature Chemistry* **2021**, *13* (4), 319-326.
117. Gavitt, T. D.; Hartmann, A. K.; Sawant, S. S.; Mara, A. B.; Szczepanek, S. M.; Rouge, J. L., A GATA3 Targeting Nucleic Acid Nanocapsule for In Vivo Gene Regulation in Asthma. *ACS Nano* **2021**, *15* (7), 11192-11201.
118. Petree, J. R.; Yehl, K.; Galior, K.; Glazier, R.; Deal, B.; Salaita, K., Site-Selective RNA Splicing Nanozyme: DNAzyme and RtcB Conjugates on a Gold Nanoparticle. *ACS Chemical Biology* **2018**, *13* (1), 215-224.

119. Zhang, J.; Ma, R.; Blanchard, A.; Petree, J.; Jo, H.; Salaita, K., Conditional Deoxyribozyme–Nanoparticle Conjugates for miRNA-Triggered Gene Regulation. *ACS Applied Materials & Interfaces* **2020**, *12* (34), 37851-37861.
120. Hartmann, A. K.; Cairns-Gibson, D. F.; Santiana, J. J.; Tolentino, M. Q.; Barber, H. M.; Rouge, J. L., Enzymatically Ligated DNA–Surfactants: Unmasking Hydrophobically Modified DNA for Intracellular Gene Regulation. *ChemBioChem* **2018**, *19* (16), 1734-1739.
121. Crooke, S. T.; Wang, S.; Vickers, T. A.; Shen, W.; Liang, X.-h., Cellular uptake and trafficking of antisense oligonucleotides. *Nature Biotechnology* **2017**, *35* (3), 230-237.
122. Huo, S.; Li, H.; Boersma, A. J.; Herrmann, A., DNA Nanotechnology Enters Cell Membranes. *Advanced Science* **2019**, *6* (10), 1900043.
123. Acton, S.; Rigotti, A.; Landschulz, K. T.; Xu, S.; Hobbs, H. H.; Krieger, M., Identification of Scavenger Receptor SR-BI as a High Density Lipoprotein Receptor. *Science* **1996**, *271* (5248), 518-520.
124. Lee, J.-W.; Bae, S.-H.; Jeong, J.-W.; Kim, S.-H.; Kim, K.-W., Hypoxia-inducible factor (HIF-1) α : its protein stability and biological functions. *Experimental & Molecular Medicine* **2004**, *36* (1), 1-12.
125. Ryan, H. E.; Lo, J.; Johnson, R. S., HIF-1 α is required for solid tumor formation and embryonic vascularization. *The EMBO Journal* **1998**, *17* (11), 3005-3015.
126. Hong, W. X.; Hu, M. S.; Esquivel, M.; Liang, G. Y.; Rennert, R. C.; McArdle, A.; Paik, K. J.; Duscher, D.; Gurtner, G. C.; Lorenz, H. P.; Longaker, M. T., The Role of Hypoxia-Inducible Factor in Wound Healing. *Adv Wound Care (New Rochelle)* **2014**, *3* (5), 390-399.
127. Koh, M. Y.; Spivak-Kroizman, T.; Venturini, S.; Welsh, S.; Williams, R. R.; Kirkpatrick, D. L.; Powis, G., Molecular mechanisms for the activity of PX-478, an antitumor inhibitor of the hypoxia-inducible factor-1 α . *Molecular Cancer Therapeutics* **2008**, *7* (1), 90.
128. Onnis, B.; Rapisarda, A.; Melillo, G., Development of HIF-1 inhibitors for cancer therapy. *Journal of Cellular and Molecular Medicine* **2009**, *13* (9a), 2780-2786.
129. Juliano, R. L.; Ming, X.; Carver, K.; Laing, B., Cellular Uptake and Intracellular Trafficking of Oligonucleotides: Implications for Oligonucleotide Pharmacology. *Nucleic Acid Therapeutics* **2014**, *24* (2), 101-113.
130. Gao, F.; Chattopadhyay, A.; Navab, M.; Grijalva, V.; Su, F.; Fogelman, A. M.; Reddy, S. T.; Farias-Eisner, R., Apolipoprotein A-I Mimetic Peptides Inhibit Expression and Activity of Hypoxia-Inducible Factor-1 α in Human Ovarian Cancer Cell Lines and a Mouse Ovarian Cancer Model. *Journal of Pharmacology and Experimental Therapeutics* **2012**, *342* (2), 255.
131. Weidemann, A.; Johnson, R. S., Biology of HIF-1 α . *Cell Death & Differentiation* **2008**, *15* (4), 621-627.
132. Zhang, J.; Sharma, R.; Ryu, K.; Shen, P.; Salaita, K.; Jo, H., Conditional Antisense Oligonucleotides Triggered by miRNA. *ACS Chemical Biology* **2021**, *16* (11), 2255-2267.
133. Ben-Aicha, S.; Escate, R.; Casaní, L.; Padró, T.; Peña, E.; Arderiu, G.; Mendieta, G.; Badimón, L.; Vilahur, G., High-density lipoprotein remodelled in hypercholesterolaemic blood induce epigenetically driven down-regulation of endothelial HIF-1 α expression in a preclinical animal model. *Cardiovascular Research* **2020**, *116* (7), 1288-1299.
134. Fernández-Hernando, C., Antiatherogenic Properties of High-Density Lipoprotein–Enriched MicroRNAs. *Arteriosclerosis, Thrombosis, and Vascular Biology* **2014**, *34* (6), e13-e14.
135. Rosi, N. L.; Giljohann, D. A.; Thaxton, C. S.; Lytton-Jean, A. K. R.; Han, M. S.; Mirkin, C. A., Oligonucleotide-Modified Gold Nanoparticles for Intracellular Gene Regulation. *Science* **2006**, *312* (5776), 1027-1030.
136. Li, H.; Zhang, B.; Lu, X.; Tan, X.; Jia, F.; Xiao, Y.; Cheng, Z.; Li, Y.; Silva, D. O.; Schrekker, H. S.; Zhang, K.; Mirkin, C. A., Molecular spherical nucleic acids. *Proceedings of the National Academy of Sciences* **2018**, *115* (17), 4340-4344.
137. Li, D.; Gordon, S.; Schwendeman, A.; Remaley, A. T., Apolipoprotein Mimetic Peptides for Stimulating Cholesterol Efflux. In *Apolipoprotein Mimetics in the Management of Human*

Disease, Anantharamaiah, G. M.; Goldberg, D., Eds. Springer International Publishing: Cham, 2015; pp 29-42.

138. Banga, R. J.; Chernyak, N.; Narayan, S. P.; Nguyen, S. T.; Mirkin, C. A., Liposomal Spherical Nucleic Acids. *Journal of the American Chemical Society* **2014**, *136* (28), 9866-9869.

139. Zaborowska, Z. a.; Fürste, J. P.; Erdmann, V. A.; Kurreck, J., Sequence Requirements in the Catalytic Core of the ϕ 10-23 DNA Enzyme *. *Journal of Biological Chemistry* **2002**, *277* (43), 40617-40622.

140. Seferos, D. S.; Prigodich, A. E.; Giljohann, D. A.; Patel, P. C.; Mirkin, C. A., Polyvalent DNA Nanoparticle Conjugates Stabilize Nucleic Acids. *Nano Letters* **2009**, *9* (1), 308-311.

141. Nieland, T. J. F.; Penman, M.; Dori, L.; Krieger, M.; Kirchhausen, T., Discovery of chemical inhibitors of the selective transfer of lipids mediated by the HDL receptor SR-BI. *Proceedings of the National Academy of Sciences* **2002**, *99* (24), 15422-15427.

142. Yu, M.; Romer, K. A.; Nieland, T. J.; Xu, S.; Saenz-Vash, V.; Penman, M.; Yesilaltay, A.; Carr, S. A.; Krieger, M., Exoplasmic cysteine Cys384 of the HDL receptor SR-BI is critical for its sensitivity to a small-molecule inhibitor and normal lipid transport activity. *Proc Natl Acad Sci U S A* **2011**, *108* (30), 12243-8.

143. Thuahnai, S. T.; Lund-Katz, S.; Williams, D. L.; Phillips, M. C., Scavenger Receptor Class B, Type I-mediated Uptake of Various Lipids into Cells: INFLUENCE OF THE NATURE OF THE DONOR PARTICLE INTERACTION WITH THE RECEPTOR*. *Journal of Biological Chemistry* **2001**, *276* (47), 43801-43808.

144. Margus, H.; Padari, K.; Pooga, M., Cell-penetrating Peptides as Versatile Vehicles for Oligonucleotide Delivery. *Molecular Therapy* **2012**, *20* (3), 525-533.

145. Konate, K.; Crombez, L.; Deshayes, S.; Decaffmeyer, M.; Thomas, A.; Bresseur, R.; Aldrian, G.; Heitz, F.; Divita, G., Insight into the Cellular Uptake Mechanism of a Secondary Amphipathic Cell-Penetrating Peptide for siRNA Delivery. *Biochemistry* **2010**, *49* (16), 3393-3402.

146. van Rheenen, J.; Langeslag, M.; Jalink, K., Correcting Confocal Acquisition to Optimize Imaging of Fluorescence Resonance Energy Transfer by Sensitized Emission. *Biophysical Journal* **2004**, *86* (4), 2517-2529.

147. Horzum, U.; Ozdil, B.; Pesen-Okvur, D., Step-by-step quantitative analysis of focal adhesions. *MethodsX* **2014**, *1*, 56-59.

148. Han, G.; Chari, N. S.; Verma, A.; Hong, R.; Martin, C. T.; Rotello, V. M., Controlled Recovery of the Transcription of Nanoparticle-Bound DNA by Intracellular Concentrations of Glutathione. *Bioconjugate Chemistry* **2005**, *16* (6), 1356-1359.

149. Nagao, A.; Kobayashi, M.; Koyasu, S.; Chow, C. C. T.; Harada, H., HIF-1-Dependent Reprogramming of Glucose Metabolic Pathway of Cancer Cells and Its Therapeutic Significance. *Int J Mol Sci* **2019**, *20* (2).

150. Graham, K.; Unger, E., Overcoming tumor hypoxia as a barrier to radiotherapy, chemotherapy and immunotherapy in cancer treatment. *Int J Nanomedicine* **2018**, *13*, 6049-6058.

151. Jing, X.; Yang, F.; Shao, C.; Wei, K.; Xie, M.; Shen, H.; Shu, Y., Role of hypoxia in cancer therapy by regulating the tumor microenvironment. *Molecular Cancer* **2019**, *18* (1), 157.

152. Niora, M.; Pedersbæk, D.; Münter, R.; Weywadt, M. F. d. V.; Farhangibarooji, Y.; Andresen, T. L.; Simonsen, J. B.; Jauffred, L., Head-to-Head Comparison of the Penetration Efficiency of Lipid-Based Nanoparticles into Tumor Spheroids. *ACS Omega* **2020**, *5* (33), 21162-21171.

153. Walkey, C. D.; Olsen, J. B.; Guo, H.; Emili, A.; Chan, W. C. W., Nanoparticle Size and Surface Chemistry Determine Serum Protein Adsorption and Macrophage Uptake. *Journal of the American Chemical Society* **2012**, *134* (4), 2139-2147.

154. Rizzo, L. Y.; Theek, B.; Storm, G.; Kiessling, F.; Lammers, T., Recent progress in nanomedicine: therapeutic, diagnostic and theranostic applications. *Current Opinion in Biotechnology* **2013**, *24* (6), 1159-1166.

155. Augustine, R.; Hasan, A.; Primavera, R.; Wilson, R. J.; Thakor, A. S.; Kevadiya, B. D., Cellular uptake and retention of nanoparticles: Insights on particle properties and interaction with cellular components. *Materials Today Communications* **2020**, *25*, 101692.